# Aeroelastic Optimization of Stick Models for Parametric Flutter Investigations in Blended-Wing-Body Aircraft

by

Diogo Bravo
B.Sc. in Aerospace Engineering, Instituto Superior Técnico, 2023

A Thesis Submitted in Partial Fulfillment of the
Requirements for the Degree of

MASTER OF APPLIED SCIENCE

in the Department of Mechanical Engineering

© Diogo Bravo, 2026
University of Victoria

All rights reserved. This thesis may not be reproduced in whole or in part, by photocopy or other means, without the permission of the author.

We acknowledge and respect the Lək̓ʷəŋən (Songhees and Xʷsepsəm/Esquimalt) Peoples on whose territory the university stands, and the Lək̓ʷəŋən and W̱SÁNEĆ Peoples whose historical relationships with the land continue to this day.

# Aeroelastic Optimization of Stick Models for Parametric Flutter Investigations in Blended-Wing-Body Aircraft

by

Diogo Bravo
B.Sc. in Aerospace Engineering, Instituto Superior Técnico, 2023

**Supervisory Committee**

Dr. Afzal Suleman, Co-Supervisor
(Department of Mechanical Engineering)

Dr. Mario Bras, Co-Supervisor
(Department of Mechanical Engineering)

Dr. Issa Traoré, Outside Member
(Department of Electrical and Computer Engineering)

# ABSTRACT

This work focuses on assessing the aeroelastic behaviour of a Blended-Wing-Body (BWB) aircraft configuration and proposes a model order reduction framework to enable systematic parametric analysis on aerodynamic shape and structural properties. A high-fidelity baseline aeroelastic model is first developed and assessed under ultimate loading conditions in accordance with certification requirements. Modal analysis identifies the dominant bending and torsional modes governing the dynamic response, and the Modal Assurance Criterion (MAC) is used to assess modal coupling. Aeroelastic investigations reveal two critical instabilities within the flight envelope: symmetric and antisymmetric bending-torsion flutter (BTF).

A reduced-order stick model (SM) was calibrated through an optimization workflow to replace the flexible wing in a hybrid configuration. This condensation approach reduces computational cost for aeroelastic analysis while preserving the physical significance of the model. Three case studies are conducted to match the static deformation, modal response, and aeroelastic behaviour of the full GFEM. Dedicated error metrics are introduced to quantify discrepancies in vertical displacement, twist, natural frequencies, and mode shapes.

Two novel aeroelastic metrics are proposed: an eigenvalue error metric based on the Error Vector Magnitude (EVM) concept ($E_e$) and a robust complex mode shape metric ($E_x$) tailored for complex aeroelastic eigenvectors. The optimized hybrid model predicts flutter speed within 3% error and accurately reproduces the underlying instability mechanisms, while significantly reducing computational effort.

To better understand the flutter mechanisms of the BWB configuration, the reduced-order model is used in a parametric study involving six geometric and structural parameters. The study characterizes the evolution of flutter mechanisms across the BWB design space. For the 600 configurations evaluated, the governing instability was bending-torsion flutter (BTF). The proposed methodology can suggest modifications to the configuration capable of raising the flutter speed by up to 30%.

# Table of Contents

# List of Tables

# List of Figures

# Glossary

**AFRL** Air Force Research Laboratories.

**AIC** Aerodynamic Influence Coefficient.

**BFF** Body-Freedom Flutter.

**BTF** Bending-Torsion Flutter.

**BW** Box Wing.

**BWB** Blended-Wing-Body.

**CAD** Computer Aided Design.

**CARs** Canadian Aviation Regulations.

**CFD** Computational Fluid Dynamics.

**CG** Center-of-Gravity.

**DLM** Double-Lattice Method.

**EASA** European Union Aviation Safety Agency.

**EVM** Error Vector Magnitude.

**FAA** Federal Aviation Administration.

**FE** Finite Elements.

**FEM** Finite Elements Method.

**FW** Flying Wing.

**GFEM** Generalized Finite Element Model.

**GVT** Ground Vibration Test.

**HALE** High-Altitude, Long-Endurance.

**HARW** High Aspect Ratio Wing.

**ISR** Intelligence, Surveillance and Reconnaissance.

**JW** Joined Wing.

**LCO** Limit Cycle Oscillation.

**MAC** Modal Assurance Criterion.

**MDO** Multidisciplinary Design Optimization.

**MOR** Model Order Reduction.

**RMS** Root Mean Square.

**ROM** Reduced Order Model.

**RPO** Residual Pitch Oscillation.

**SM** Stick Model.

**UAV** Unmanned Aerial Vehicle.

**USAF** United States Air Force.

**WBT** Wing-Body-Tail.

# ACKNOWLEDGEMENTS

First, I would like to thank my family for their unconditional support throughout this journey. Even when distance meant sharing many moments only over the phone, their encouragement and care were always present. I know that they would cross the world for me, and I am deeply grateful for their constant belief in me.

I would also like to thank Dr. Suleman and Dr. Shohreh Hadian for fostering such a welcoming community in Victoria, making it truly feel like a second home. Their dedication to building an environment where students can thrive academically and personally does not go unnoticed. I am equally grateful for the opportunity to be part of the amazing research group at UVic CfAR. I would also like to thank Dr. Bras for sharing his experience and guidance, and for helping me grow as an engineer, I hope our paths cross again in academia.

Finally, I would like to thank all my incredible friends from 33 Henderson Rd, Wednesday Breakfast and Thursday Volleyball. Thanks to them, these past two years were filled with unforgettable moments. Of course, this journey began long before, my friend from Tertulizinha will always be in my heart, together with the friends I grew up with in Viseu.

As this chapter comes to an end, I feel proud of everything I have accomplished so far. Above all, I carry with me a simple wish: to give back the same love, kindness, and support that I have received along the way.

*Always chasing my*
*dreams.*

# Chapter 1

# Introduction

## 1.1 Background and Motivation

In recent years, the global push toward greener and more efficient aviation intensified, driven by ambitious decarbonization goals adopted by Europe and Canada to reduce CO2 emissions by 40-55% by 2030 [1, 2]. These environmental objectives are reshaping aircraft design priorities. Modern airframes increasingly rely on lightweight composite, slender structures [3–5], which, while beneficial for performance and fuel consumption, are inevitably prone to severe nonlinear vibration problems due to their greater flexibility. In parallel, novel configurations such as the Blended-Wing-Body (BWB) offer promising gains in aerodynamic performance [6–8], although presenting significant challenges related to aeroelastic instabilities.

Aeroelastic phenomena such as divergence, control-reversal, limit cycle oscillation, and particularly flutter emerge from the coupling between aerodynamic forces, structural deformation, and inertial effects [9, 10]. Classical flutter causes divergent oscillatory vibrations of the wings, and it is typically dominated by bending-torsion interactions [11]. However, flutter mechanisms of unconventional configurations may deviate from this paradigm. BWBs and other unconventional configurations are prone to non-classical instabilities, such as body-freedom flutter, at low speeds [12, 13].

Ensuring that these advanced aircraft concepts satisfy the structural integrity and safety standards mandated by FAA, EASA, and CARs [14–16] regulations requires accurate prediction of their static, dynamic, and aeroelastic behaviour. High-fidelity finite element models (GFEMs) can capture the structural response of BWB configurations with excellent accuracy, particularly when calibrated with Ground Vibration

Test (GVT) data, thereby increasing confidence in analytical flutter predictions [17–21]. Despite their accuracy, GFEMs are computationally prohibitive for iterative workflows.

This thesis research aims to further the understanding of flutter mechanisms within the design space of a BWB. A minimum set of aerodynamic and structural design parameters is identified and systematically varied to examine how these influence the onset speed and the nature of flutter instabilities.

Although GFEMs provide the required level of fidelity for structural and aeroelastic analysis, their computational cost makes them impractical for iterative workflows, such as those involved in optimization, parametric studies, and even during numerous subcases in the certification process. Reduced order models (ROMs) offer a practical and efficient alternative to GFEMs, capturing the essential structural behaviour while drastically reducing computational effort [22].

## 1.2 Literature Review

This dissertation is a study on flutter mechanisms of a blended-wing-body (BWB) aircraft. There is much ongoing research and literature in this area, so it is appropriate to summarize some relevant studies in this section.

### 1.2.1 Brief History on Aeroelasticity

Aeroelasticity is the study of the interaction between aerodynamic, inertial, and elastic forces in a flexible structure immersed in a fluid flow. Its origins trace back to the early 20th century, when the foundational work of Frazer, Duncan, and others [23–27], demonstrated that these coupled interactions could lead to unexpected and sometimes catastrophic phenomena.

Collar [9] proposed on his note an approach to visualize this multidisciplinary concept in a diagram known as Collar's Aeroelastic Triangle. Elastic, inertial, and aerodynamic forces are placed at the vertices, and different disciplines emerge from the interaction between two, or three, of these forces. Flutter, buffeting, divergence, control reversal, gust response, and structural vibrations are some examples of issues related to aeroelasticity.

There is extensive theoretical and experimental research in this field, including the works of Livne [28], Fung [29], Weisshaar [30], and Rodden [31]. Bisplinghoff

[10] emphasized that aeroelastic behaviour manifests in two fundamental ways: static interactions, arising from the coupling of elastic and aerodynamic forces and leading to phenomena such as divergence, and dynamic interactions, in which inertial, elastic and aerodynamic forces couple to produce oscillatory instabilities such as flutter.

*Introduction to Aircraft Aeroelasticity and Loads* (Wright and Cooper [32]) served as the principal reference for this work, guiding both the theoretical background and the methodology adopted throughout.

Historically, the dynamic instability known as flutter has received the most attention due to its potentially destructive consequences and its critical role in defining the operational flight envelope. Certification regulations (CS/CFR 25.629 [33, 34]) require that the flutter boundary lie outside the aircraft's flight envelope with a safety margin of at least 15%. Above the critical flutter speed, any dynamic structural disturbance leads to self-sustained oscillations that can no longer be structurally damped, resulting in severe structural damage, loss of aerodynamic performance, ride comfort degradation, or loss of control [11, 35].

### Bending-Torsion Flutter

Hancock[11] attempted to clarify some basic ideas on wing flexure-torsion flutter, providing a physical description and explanation of the phenomenon. Flutter arises when an aircraft component, for example the wing or the tailplane, exhibits self-sustained oscillations at a certain forward speed. In the classical sense of the term, flutter occurs when two or more structural modes couple while excited by unsteady aerodynamic loads. Bending and torsion modes are the most common pair to couple.

Kassner [36] established the basis for solving the two-degree-of-freedom bending-torsion flutter problem. The author considered a two-dimensional (bending, torsion) problem of vibrating wings and described a practical method for assessing vibration characteristics and avoiding adverse coupling. Theodorsen[37] developed a rigorous aerodynamic theory for oscillating airfoils. The author identified three independent degrees of freedom (bending, torsion and aileron) to calculate the flutter velocity as a function of the interacting modal frequencies.

Experimental studies by Bollay and Brown [38] confirmed these theories, showing in wind-tunnel tests that the bending and torsion natural frequencies converge as the flutter boundary is approached - a distinguishing feature of classical bending-torsion flutter.

### Body-Freedom Flutter

Banerjee [12, 13] was the first to recognize that flutter can arise from the coupling between rigid-body motion and elastic wing modes. In his study of the tailless Ricochet sailplane, he identified an unstable low-speed flapping motion produced by the interaction between the short-period oscillation and the first wing-bending mode.

Schweiger [39] et al provided a more comprehensive explanation of the short period/wing bending coupling and demonstrated that insufficient wing stiffness was the primary cause of the instability.

Niblett [40] offered an analytical perspective on the nature of body-freedom flutter and concluded that it is highly unlikely to occur in swept-back wing configurations, which is in agreement with wind-tunnel tests reported by Gaukroger [41]. Conversely, swept-forward wings are more susceptible to body-freedom flutter because their aerostructural coupling tends to be destabilising. Mitigating this instability typically requires moving the center of lift upwind, although this is often difficult to achieve in practice.

## 1.2.2 Aeroelastic Effects on Different Aircraft Configurations

Novel configurations such as blended-wing-body (BWB) aircraft, flying wings, or high-altitude long-endurance (HALE) platforms are emerging as promising solutions for future sustainable aviation. However, each configuration poses a unique aeroelastic challenge, due to aerodynamic nonlinearities, structural nonlinearities, and the coupling between both within the flight envelope.

Livne and Weisshaar [42, 43] presented a comprehensive survey of the aeroelastic characteristics of nonconventional configurations, including BWBs, flying wings, joined wings, and HALE wings. Van Schoor and von Flotow [44] were among the first who studied the nonlinear aeroelastic characteristics of very flexible aircraft. Patil [45–47] and Palacios [48] analysed the effects of structural geometric nonlinearities on the coupling between aeroelasticity and flight dynamics of high aspect-ratio wings. Drela [49, 50] developed ASWING, a simulation toolbox with aerodynamics, structures, flight dynamics, and control laws fully and nonlinearly coupled for rapid and effective preliminary design of flexible aircraft. In parallel, Cesnik [51, 52] developed UM/NAST, a novel and practical solution to the coupled nonlinear aeroelasticity and flight dynamics of very flexible aircraft. Afonso [53, 54] reviewed the nonlinear aeroelastic behaviour of very flexible High Aspect Ratio Wings (HARW).

These works highlighted the necessity of incorporating aeroelastic tailoring within the Multidisciplinary Design Optimization (MDO) process. Jonsson [35] reviewed methods for flutter prediction that enforce flutter and post-flutter constraints in aircraft design optimization, while Najmi [55] discussed state-of-the-art aeroelastic tailoring techniques for flutter mitigation and passive aeroelastic control. Another alternative is the development of active control systems [56] to extend the flight envelope.

The next-generation of flexible aircraft must be analysed and designed with methods that capture nonlinear behaviour, such as large deformation, and non-classical flutter mechanisms. Once reliable yet efficient analysis tools for design and certification exist, the risk-averse aerospace community will be more willing to adopt these novel configurations [57].

### Blended-Wing-Body

Liebeck [6–8] proposed the blended-wing-body configuration as a solution for commercial transport planes for subsonic flight. The BWB is a tailless aircraft that combines the centerbody and propulsion system into the aerodynamic layout. Liebeck [6, 8] mentioned that this configuration has the potential to revolutionize the aerospace industry, mainly due to the large performance advantages over conventional aircraft. For example, the BWB offers a major increase in lift to drag ratio (L/D), a reduction in takeoff weight (MTOW), and a substantial decrease in fuel burn. The passenger experience is also improved thanks to the exceptionally spacious cabin layout.

Currently, JetZero [58], Airbus [59], and Bombardier [60] projects are shaping the future of commercial aviation through the development of blended-wing-body concepts. Small-scale demonstrators have been built and tested in wind tunnel. Flight-test campaigns are planned to assess handling qualities, the reliability of flight controls, and the effectiveness of multi-objective control surfaces.

In parallel, the BWB concept continues to attract interest for military purposes. The B-2 bomber [7, 61, 62] is a well-proven design that resembles a blended-wing-body. The X-48B [63] is a joint NASA/Boeing/AFRL project for a multi-role, long-range, high-capacity military transport aircraft. Lucia [57] further proposed the BWB as a high speed, flying sensor platform for wide-area surveillance and tracking (ISR - intelligence, surveillance and reconnaissance - missions).

Table 1.1 summarizes some recent research projects on the blended-wing-body configuration emphasizing the aeroelastic instabilities observed and the techniques used to identify them.

The B-2 bomber [61, 62] provides an important early example of the aeroelastic challenges associated with this novel configuration. During a low altitude high speed flight test, the aircraft experienced an unexpected shock-induced residual pitch oscillation (RPO), but outside the operational flight envelope. This event drew significant attention to the limitations of existing aeroelastic prediction tools and highlighted the need for more powerful and reliable analysis capabilities for design and certification of unconventional configurations.

Su [52] identified body-freedom flutter (BFF) in a blended-wing-body configuration through fully coupled computational aeroelastic simulations. The study revealed that BFF was excited by the interaction between the aircraft's short-period rigid-body mode and the first wing bending mode. The author highlighted that traditional wind tunnel tests fully constrain the rigid-body motion of the models and therefore may not accurately predict this flutter mechanism. Su further showed that torsional-bending stiffness, particularly relevant for anisotropic composite structures, significantly influences the flutter speed and may even alter the dominant flutter mechanism.

The LCLR (Low-Cost, Low-Risk) project developed at Northwestern Polytechnic University (NPU) is one of the most comprehensive aeroelastic characterisation efforts for a BWB to date. A coupled pitching/wing bending BFF mode was identified and limit cycle oscillatios (LCO) were observed experimentally [64]. The structural model was updated using extensive ground vibration test (GVT) data [64–67] to improve confidence in the numerical predictions. A dedicated suspension system [64, 65] was developed to allow plunge, pitch, and yaw motion during low-speed wind-tunnel tests, enabling accurate reproduction of the aircraft degrees of freedom. BFF was later confirmed during a flight-test campaign[64, 66, 68] to evaluate an active flutter-suppression controller. Finally, parametric studies involving center-of-gravity (CG) location and wing stiffness [68, 69], winglet tip mass [64], and nose weight [65] demonstrated that these factors influence not only the flutter speed and frequency, but may also change the governing flutter mechanism, for example from BFF to classical bending-torsion flutter (BTF). Gu [67] further demonstrated a conventional configuration with very short fuselage can exhibit a BFF instability in-flight, due to its low pitch inertia.

**Table 1.1:** Summary of recent BWB research projects.

| Project | Research group | Year | Type | Aeroelastic phenomena | Identification method |
|---|---|---|---|---|---|
| B-2 bomber [61, 62] | USAF | 1998 | BWB | RPO, LCO | CAP-TSDV, flight |
| Sensorcraft [70] | AFRL | 2005 | BWB | Divergence | NASTRAN, ASTROS |
| NMEDA [71] | AFRL | 2005 | BWB | Aeroelastic nonlinearities | NASTRAN, AVUS |
| Sensorcraft [52] | UMichigan, AFRL | 2009 | BWB | BFF, LCO | UM/NAST, wind tunnel |
| ACFA [72] | UMunich | 2012 | BWB | BTF | High-fidelity |
| LCLR [64–69] | NPU | 2015 - 2024 | BWB | BFF, LCO | NASTRAN, ZAERO, GVT, wind tunnel, flight |

### Flying Wing

Vehicles based on the flying-wing configuration have been explored since at least the early 1910s. Gibbs-Smith [73] provided a detailed survey on historical aircraft, including the Dunne No. 5 tailless aircraft. Early developments, however, did not mature into successful operational aircraft. As Weisshaar [74, 75] noted, limitations in handling qualities, flight control, dynamic stability and the relatively small size of the wings justified the failure of the design.

Despite these challenges, the flying-wing configuration offers significant performance advantages over conventional wing-body-tail designs. As Schweiger [39] emphasized, the absence of a rear fuselage and tail can yield substantial reductions in parasite drag, structural weight and manufacturing complexity. For these reasons, the design experienced a revival in the 70s, but Weisshaar [74, 75] brought aeroelastic concerns, in particular the wing static divergence, to the center of attention.

Table 1.2 summarizes some recent research projects on the flying wing configuration, emphasizing the aeroelastic instabilities observed and the techniques used to identify them.

The Free Flight Aeroelastic Demonstration (FFAD) aircraft developed by Lockheed Martin [76] was designed to exhibit body-freedom flutter. The objectives were to prove BFF onset can be accurately predicted and to test an active control system to suppress it. The test vehicle featured a very rigid center body with highly flexible wings. The aeroelastic model was defined using a structural stick model combined with a panel method aerodynamic model. The bending (EI) and torsion (GJ) characteristics of the wing along the elastic axis were designed to match the structural dynamic behaviour of the full scale vehicle, while the unsteady AIC coefficients were validated with data from a low turbulence wind tunnel test. Analytical predictions showed excellent agreement with flight test measurements for both the onset speed and frequency of the BFF mode. This correlation demonstrated the reliability of the modelling approach and established the model can be used to develop active suppression systems to control BFF and other aeroelastic instabilities.

The X-56A program [77, 78] was able to suppress flutter and fly beyond the open-loop flutter speed. The Zimmerman method [79] proved to be very useful in predicting the approximate body freedom flutter speed from in-flight data. This program also conducted controlled high-risk tests in which the control system was disabled momentarily to observe the unstable flutter mode and then reengaged to demonstrate successful flutter suppression. These results provided valuable validation of active control strategies for mitigating BFF in flexible, tailless configurations.

### Wing-Body-Tail, HALE, and Joined Wing Configurations

The wing-body-tail (WBT) configuration has dominated aircraft design since the Wright brothers, more than a century ago. Its geometric simplicity, combined with a long operational history free of major stability or control issues, gives it a comparatively low-risk profile. However, as highlighted in the Sensorcraft program [57], even this mature configuration can encounter significant aeroelastic challenges when pushed toward extreme endurance, altitude and efficiency requirements. High aspect-ratio wings (HARW) and lightweight structural designs introduce strong aeroelastic nonlinearities that invalidate many linear assumptions.

The need for nonlinear predictive capabilities was made explicit in the 3$^{\text{rd}}$ Aeroelastic Prediction Workshop (AePW3) [89], where different nonlinear aeroelastic tools were applied to the Pazy wing [90] - a highly flexible model developed to provide publicly available wind-tunnel data for validating numerical methods in the large-deflection regime. The analyses included static deformation coupling, linearisation about a deformed configuration to compute natural frequencies and mode shapes, and

**Table 1.2:** Summary of recent Flying Wing (FW) research projects.

| Project | Research group | Year | Type | Aeroelastic phenomena | Identification method |
|---|---|---|---|---|---|
| SB-13 [39] | Schweiger, J. | 1983 | FW | BFF | Flight |
| Ricochet [12, 13] | Banerjee, J. | 1984 | FW | BFF | Flight |
| Horten [80] | Nickel, K. | 1994 | FW | Pecking flutter | Flight |
| Sensorcraft [81, 82] | AFRL | 2005 | FW | BFF | NASTRAN, ASWING, wind tunnel |
| Sensorcraft [76, 83] | Lockheed Martin | 2010 | FW | BFF, BTF | NASTRAN, GVT, flight |
| Helios [51, 84] | UMichigan, NASA | 2011 | FW | Aeroelastic nonlinearities, divergence | UM/NAST, flight |
| MiniMUTT [85] | UMinnesota | 2020 | FW | BFF, BTF | GVT, flight |
| X-56A [77, 78] | NASA | 2023 | FW | BFF, BTF, LCO | Zimmerman [79], flight |
| [86–88] | UNanjing | 2024 | FW | BFF, BTF | High-fidelity, GVT, wind tunnel, flight |

prediction of flutter onset and offset speeds. Software such as UM/NAST, SHARPy, MSC NASTRAN, and Simecenter NASTRAN all successfully captured the decisive nonlinear aeroelastic effects, demonstrating the importance of such tools for modern flexible aircraft.

High-Altitude, Long-Endurance (HALE) aircraft are being developed for a wide range of missions, including for unmanned intelligence, surveillance, and reconnaissance (ISR), communications relay for military and civilian applications, and environmental and atmospheric sensing [46, 57, 91]. The Sensorcraft project [57] aims to demonstrate an UAV capable of loitering for 30 hours of endurance and 2000 nautical miles range. Aircraft to meet these performance requirements have characteristic features, such as slender high aspect ratio wings with thick airfoils, and very low structural weight [92]. From a structural viewpoint, this leads to very flexible airframes that undergo large static and dynamic deflections under flight loads and exhibit rigid-elastic coupling [93].

In the context of the X-HALE [94] project, a highly flexible, remote-piloted aircraft was built to collect in-flight data on the nonlinear aeroelastic coupling between structural deformation and rigid-body dynamics. The project's objective was to correlate flight measurements with predictions from the simulation toolbox UM/NAST, thereby validating the code for nonlinear aeroelastic analysis.

The joined wing (JW) configuration was first introduced by Wolkovitch [95] in 1987 as a potential solution for commercial transport applications [95], and was later considered for high altitude surveillance missions within the Sensorcraft program [57]. In this arrangement, a rear wing is attached near the top of the vertical tail and joined to the trailing edge of the forward wing, allowing this structure to act both as a horizontal tail and as a strut brace [96]. Samuels [97] compared the structural weight of a joined wing against a conventional configuration and reported potential weight savings of approximately 12-22%. From an aerodynamic perspective, Prandtl's theory [98] predicts this geometry can achieve lower induced drag than a single wing of the same span. Smith [96] examined the performance, stability, and control of a joined wing in wind tunnel tests. However, the influence of structural deformation on the aerodynamic and aeroelastic responses proved to be difficult to intuit and predict. Livne [43] provided a comprehensive survey on the aeroelastic challenges of joined-wing aircraft configurations. Box Wing (BW), strut-braced and truss-braced wings can be categorized together with JW as non-planar wing.

Weisshaar [99] presented a methodology for integrating optimization in the aeroelastic design of a joined wing aircraft. This study identified key design parameters, such as fuselage pitch inertia, wing sweep, CG position, and skin thickness, that affect the aeroelastic response. Particularly, the analysis showed these parameters can alter the dominant flutter mechanism, shifting the instability from BFF to a more classical BTF mode. The results further demonstrate that rigid-body modes must be included in the aeroelastic model, as joined-wing configurations are especially prone to instabilities arising from coupling between elastic wing modes and the aircraft pitch mode. Weisshaar argues that aerolastic tailoring, achieved by incorporating flutter constraints into the structural optimization cycle, can effectively suppress the unstable BFF mode.

Table 1.3 summarizes some recent research projects on aeroelastic instabilities observed and the techniques used to identify them.

**Table 1.3:** Miscellaneous research projects.

| **Project** | **Research group** | **Year** | **Type** | **Aeroelastic phenomena** | **Identification method** |
|---|---|---|---|---|---|
| [100] | Goland, M. | 1945, 2018 | Goland wing | BTF, LCO | Rayleigh-Ritz |
| [101] | ULiege | 2012 | Rect. | Pitch-plunge flutter, stall flutter, LCO | Wind tunnel |
| [102] | USAF | 2016 | Rect. | Stall flutter, LCO | Wind tunnel |
| [103, 104] | UVIC, IST | 2017 | HARW | BTF | NASTRAN |
| FLEXOP [105] | UBristol | 2018 | Rect. | BFF | LFT-$\mu$ [106, 107] |
| QT1 [108] | UVIC, IST | 2022 | HARW | Coupled rigid-body elastic modes | NASTRAN, ASWING, GVT, flight test |
| AePW3 [89, 90] | Extended collaboration | 2021, 2024 | Pazy wing | BTF | Different fidelity software, wind tunnel |
| [45–47, 109] | GeorgiaTech, MIT | 1999-2004 | HALE | Aeroelastic nonlinearities, BTF, LCO | Nonlinear beam Peters-Johnson |
| Sensorcraft [92] | UMichigan | 2011 | HALE | BTF | UM/NAST, AVUS |
| X-HALE [94] | UMichigan, AFRL | 2012 | HALE | Coupled dutch-roll and wing bending | UM/NAST, wind tunnel, flight test |
| [99] | Weisshaar, T. | 2002 | JW | BFF | ASTROS |
| Sensorcraft [110] | UMichigan, AFRL | 2005 | JW | Coupled rigid-body elastic modes | UM/NAST |
| Prandtl Plane [111] | UPisa | 2016 | BW | BTF, BFF, LCO | NASTRAN, in-house tool |

### 1.2.3 Aeroelastic Tailoring: Concepts and Applications

Aeroelastic tailoring refers to the deliberate manipulation of aerodynamic and structural characteristics to influence the aeroelastic response of an aircraft. According to Weisshar, *aeroelastic tailoring is the embodiment of directional stiffness into an aircraft structural design to control aeroelastic deformation, static or dynamic, in such a fashion as to affect the aerodynamic and structural performance of that aircraft in a beneficial way* [112].

Traditionally, aeroelastic tailoring has been employed as a design strategy to enhance performance, through weight reduction, or to mitigate adverse aeroelastic phenomena, such as divergence or flutter. Najmi [55] provides a comprehensive overview of state-of-the-art aeroelastic tailoring techniques for flutter mitigation and passive aeroelastic control, while highlighting the historical development and theoretical foundations of the field.

The use of parametric aeroelastic tailoring is well established in the literature as a framework to investigate the sensitivity of flutter to variations in aerodynamic geometry, structural stiffness and inertial properties. This approach has proven particularly effective in identifying the dominant coupling mechanisms and clarifying the effect of each parameter on the flutter onset speed.

#### Raising the Flutter Boundary

One of the primary applications of aeroelastic tailoring is to increase the flutter boundary through targeted modifications of aerodynamic shape and structural properties. This section reviews how individual parameters influence the flutter onset speed, highlighting both beneficial and adverse trends reported in the literature.

Weisshaar [99] identified wing sweep angle ($\Lambda$) as a key parameter affecting the aeroelastic response of joined-wing configurations, showing that increased sweep is generally associated with higher flutter speeds for BFF. In contrast, the onset speed of BTF decreases for more sweptback wings. Nevertheless, body-freedom flutter remains the governing instability, as it consistently occurs at lower airspeeds. Similar trends were observed experimentally by Ang [87, 88] in sweptback flying wings.

Afonso [53, 103] investigated the effect of geometric nonlinearities in high-aspect ratio tapered configurations. The study showed that increasing aspect ratio (AR) leads to a reduction in flutter speed, whereas taper ratio ($\lambda$) has a positive effect on the flutter boundary, with tapered wings exhibiting higher flutter speeds than their rectangular counterparts. For these conventional configurations, the governing instability was identified as classical BTF.

Banerjee [12, 13] identified low pitch inertia as the primary driver of BFF in flying wing configurations. Increasing pitch inertia ($I_z$) [99, 111], bending stiffness (EI) [39, 52, 68, 81, 105], or torsional stiffness (GJ) [39, 52] has been shown to raise the flutter boundary and passively mitigate BFF. Shi [65] and Lei [69] confirmed these trends through wind tunnel experiments by varying the pitch inertia and bending stiffness, respectively, on a blended-wing-body configuration.

The center-of-gravity location ($x_{\mathrm{CG}}$) has a significant influence on the flutter onset speed. An aft shift of the CG position [81, 99] reduces static margin, which may lead to aircraft instability, but simultaneously raises the flutter speed of BFF. In parallel, Lei [69] confirmed this trend experimentally in wind tunnel tests.

Ang [87, 88] and Liu [64] showed through wind-tunnel tests that the flutter speed associated with BFF modes decreases with increasing wingtip mass ($m_{\mathrm{wt}}$) or when the wingtip mass is moved aft ($x_{m_{\mathrm{wt}}}$). In contrast, increasing tip weights and shifting the weights towards the tip causes the flutter boundary to increase for the BTF mode.

Ang's experimental work [87, 88] is particularly relevant because it demonstrates that BFF and BTF respond differently to variations in aerodynamic and structural parameters. These differences arise from the fundamentally distinct physical nature of the two flutter mechanisms and highlights the importance of identifying the governing flutter mechanism before proceeding with aeroelastic tailoring.

### Transitioning Between Flutter Mechanisms

In addition to shifting the flutter boundary, aeroelastic tailoring can fundamentally alter the governing flutter mechanism. Several studies have shown that targeted variations of key parameters can induce transitions between body-freedom flutter (BFF) and classical bending-torsion flutter (BTF).

Increasing the sweep angle [87, 88, 99], pitch inertia [99, 111], bending stiffness [52, 105], or torsional stiffness [52] not only raises the flutter boundary but may also promote a transition from a BFF mode to BTF. Shifting the CG position aft [99] has been shown to have a similar effect. Lei [69] confirmed these trends through wind tunnel experiments, in which a BWB with increased stiffness or an aft CG position exhibited a BTF instability, in contrast to the BFF mode observed in the baseline configuration.

Afonso [53, 104] identified a transition from a second bending-torsion flutter mode to a higher third bending-torsion mode when increasing the aspect-ratio of a conventional configuration. Liu [64] showed experimentally that increasing the wingtip mass can change the flutter type of a BWB, triggering a transition from BFF to a pitch-plunge coupled flutter mode.

**Table 1.4:** Summary of parametric effects on flutter speed and governing flutter mechanisms reported in the literature, with increasing parameter.

| **Increasing parameter** | **Description** | **Governing mechanism** | **Flutter boundary** | **Mechanism transition** |
|---|---|---|---|---|
| $\Lambda$<br>[87, 88, 99] | Sweep angle | BFF<br>BTF | Increases<br>Decreases | BFF → BTF |
| AR<br>[103, 104] | Aspect ratio | BTF | Decreases | BTF → higher-order BTF |
| $\lambda$<br>[103, 104] | Taper ratio | BTF | Increases | No change reported |
| EI<br>[39, 52, 81]<br>[68, 69, 105] | Bending stiffness | BFF | Increases | BFF → BTF |
| GJ<br>[39, 52] | Torsional stiffness | BFF | Increases | BFF → BTF |
| $I_z$<br>[65, 99, 111] | Pitch inertia | BFF | Increases | BFF → BTF |
| Aft $x_{\mathrm{CG}}$<br>[69, 81, 99] | CG location | BFF | Increases | BFF → BTF |
| $m_{\mathrm{wt}}$<br>[64, 87, 88] | Wingtip mass | BFF<br>BTF | Decreases<br>Increases | BFF → pitch-plunge flutter |
| Aft $x_{m_{\mathrm{wt}}}$<br>[64, 87, 88] | Wingtip mass location | BFF<br>BTF | Decreases<br>Increases | No change reported |

### 1.2.4 Model Order Reduction of Complex Airframes

The flight-test incident involving the B-2 bomber [61, 62], in which an unexpected residual pitch oscillation (RPO) was observed, alerted the aerospace community to the limitations of the state-of-the-art aeroelastic prediction tools available at the time. This event demonstrated that aeroelastic instabilities in unconventional configurations could remain undetected during the design phase and only manifest during flight testing. In parallel, Livne and Weisshaar [42, 43] emphasized the necessity of incorporating aeroelastic analysis within the multidisciplinary design optimization

(MDO) process, particularly for unconventional aircraft configurations. However, a fundamental trade-off remains: high-fidelity aeroelastic analyses require a substantial computational cost, making iterative workflows, such as parametric studies, optimization loops, or even the certification process which includes numerous subcases, computationally prohibitive. As a result, model order reduction (MOR) techniques have become indispensable for the aeroelastic analysis of complex airframes.

Thomas [22] provided a detailed review on MOR techniques, distinguished stick-based and matrix-based reduction models, and presented their theoretical formulations. The study further identified the most efficient methods suitable for iterative aeroelastic schemes and compared their performance in a case study involving a Bombardier aircraft. The results showed that matrix-based models, such as Guyan reduction (GR) [113], Improved Reduced System (IRS) [114], or Craig-Bampton (CB) [115], can be dynamically equivalent to high-fidelity GFEM models [22, 116–118], while stick models were shown to capture static structural behaviour, particularly in bending and torsion, with good accuracy [119, 120]. Additionally, both types of MOR techniques report a substantial reduction in computational cost in aeroelastic analysis.

In the present work, particular emphasis is placed on the stick model representation, despite its known limitations in dynamic fidelity. The choice is motivated because (1) the stick model retains a clear physical interpretation, which is essential for conducting parametric studies that explicitly relate aeroelastic behaviour to variations in wing-frame geometry and structural properties, and (2) stick-based models are readily compatible with multiple aeroelastic solvers beyond NASTRAN, such as SHARPy and ASWING.

A stick model (SM) is a series of interconnected beam elements, typically aligned with the structural elastic axis, and intends to represent the static and dynamic behaviour of the airframe. Traditionally, the wing is discretized in wing bays along the span, for which the distributions of flexural and torsional rigidities (EI and GJ) are estimated and then assigned to the corresponding beam element. A large variety of methodologies for SM development have been reported in the literature.

The simplest technique to obtain a SM consists of analytically extracting the cross-sectional properties for each wing bay directly from the CAD or GFEM geometry [119–122]. Alternatively, the unitary loading method [117, 118, 120, 123] estimates the equivalent beam stiffness properties from the deflection response of each cantilevered wing bay, idealized as a cantilevered segment and subjected to prescribed unit forces and moments at its free end. In parallel, Hashemi [124, 125] proposed the constraint forces technique, in which prescribed unit displacements are applied at the free end of each cantilevered wing bay and the SM properties are derived from the resulting reaction forces.

Elsayed [120] compared four SM development strategies: (1) analytical extraction of the cross-sectional properties from CAD or FEM models, (2) the unitary loading method, (3) an empirical method in which the stiffness distribution of a new wing are inferred from a database of existing aircraft wings [121, 126], and (4) a novel methodology that does not rely on the elastic axis and extracts the equivalent stiffness properties in an arbitrarily defined coordinate system [120]. The elastic axis is a reference line along which bending deformation occurs without inducing torsion [29]. However, for complex structures, its accurate determination is often non-trivial. The latter approach, which is independent of the determination of the elastic axis, provides a more robust framework for stick model development in complex aircraft structures.

Corn [127] demonstrated that complex GFEMs of aircraft structures can be effectively simplified using Timoshenko beam formulations [128], which account for transverse shear deformation and bending-torsion coupling. This approach showed very good agreement with the reference model in modal analysis. The classical Euler-Bernouli beam formulation [129] was also evaluated, but exhibited reduced accuracy. Kratochvil [130] proposed an enhanced SM formulation for flutter analysis, in which the lifting surface and control surface are merged into a single beam element, increasing the number of structural degrees of freedom from six to nine. Results showed negligible differences in both eigenfrequencies and flutter velocity when compared to the corresponding high-fidelity GFEM.

Another approach combines the SM methodology with matrix reduction techniques. Palacios [131] proposed a procedure in which the master degrees of freedom for static condensation (Guyan reduction [113]) are selected at grid points along the axis of the aircraft structure, resembling a stick model. Haiyrli [125] extended this approach to Improved Reduced System (IRS) [114] and modal condensation [132] techniques, and demonstrated that these yield more accurate dynamic responses than the constraint forces method.

Cirillo [133] proposed a frequency-based updating strategy that applies a correction factor to the SM, derived from the error in natural frequencies when comparing with the detailed GFEM. The correction is applied to the material properties, specifically the Young's modulus E and shear modulus G. Similarly, Sarojini [134, 135] alerted to the fact that directly matching the stiffness properties of complex three-dimensional cross-sections with a uniform beam representation is often challenging or infeasible. To address this limitation, complex structures are locally smeared and the equivalent stiffness is recovered by optimizing the material parameters E and G. In both approaches, the geometric properties and mass distribution of the reduced order model are preserved.

Dunn [136] and Trivailo [137] defined an optimization problem to develop stick models. The mass and stiffness properties of the beam elements are the design variables and the objective is to match the dynamic response of the SM to GVT data and static deflection to a fatigue test. Their results demonstrated that optimized SM can reproduce the measured dynamic characteristics of the aircraft with good accuracy and layed down the basis for the optimization of reduced order models.

Thomas [138] and Kose [139] further improved the optimization of reduced order models. In both works, a SM is generated and the cross-sectional properties, including area, area momnets of inertia, torsional inertia, and shear factors, are tuned in a global optimization process to minimize the discrepancies in natural frequencies and mode-shapes. The latter was quantified using the Modal Assurance Criterion (MAC). Kose additionally varied the material properties - Young's modulus and shear modulus - of each beam, increasing the design space of the problem. In both studies, the mass distribution of the original GFEM is preserved and directly transferred to the stick model.

Across these studies, simplified stick models have consistently proved to be computationally efficient while retaining sufficient accuracy for static deformation and modal analyses. As a result, SM representations are widely adopted in industrial settings, including at Bombardier [116–121, 126] and Lockheed Martin [77, 78], to support early-stage design, loads analysis, and flight-control development workflows.

However, there remains limited evidence that SM can reliably capture coupled aeroelastic behaviour in complex aircraft configurations [22, 117, 118]. The absensence of a systematic framework to quantify the SM accuracy in aeroelastic applications is a key gap in the literature. The present work addresses this gap by developing a framework for optimized stick modelling and validation, introducing error metrics to assess the applicability or limitation of stick models in static, modal and coupled aeroelastic studies.

## 1.3 Problem Statement and Objectives

Blended-Wing-Body (BWB) aircraft are susceptible to non-classical flutter mechanisms, such as body-freedom flutter, yet it remains unclear how changes in aerodynamic and structural parameters influence these phenomena. Studying these effects requires rapid parametric analyses using reduced order models (ROMs). However, there are no readily accessible software packages to simplify complex structural models for static, modal, and aeroelastic predictions. This creates a clear need for practical guidelines on how to develop a reduced order model that balances accuracy and computational efficiency. To support the parametric studies involving geometric and structural variations, a stick model representation is adopted to preserve the physical significance of the underlying structure.

**Thesis Objectives:**

- **Develop a model order reduction methodology** capable of reproducing the static, modal, and aeroelastic behaviour of a BWB with high accuracy while significantly reducing computational cost and preserving the physical significance of the wing geometry.
- **Establish a parameterization framework** for the aerodynamic shape and structural properties of the BWB configuration, identify key design parameters to explore its design space, evaluate their influence on flutter onset, and characterize the flutter mechanisms.

## 1.4 Thesis Outline

**Chapter 1** provides a general introduction and contextualization of the research topic, presents the problem statement, and outlines the research objectives. This chapter also offers an overview on aeroelasticity, unconventional aircraft configurations, aeroelastic tailoring techniques and structural model order reduction methods relevant to this study.

**Chapter 2** describes the development of the baseline aeroelastic model of the BWB, the formulation of a reduced order model for the structure together with guidelines for the aerospace engineer, and the parameterization framework used to identify key aerodynamic and structural parameters for the exploratory parametric study.

**Chapter 3** compares the static, modal and aeroelastic response of the reduced order stick model against the baseline aeroelastic model and presents the outcomes of the parametric study conducted to investigate the evolution of flutter mechanisms across the BWB design space.

**Chapter 4** summarizes the main contributions and limitations of the thesis, and outlines recommendations and directions for future work.

# Chapter 2

# Methodology

## 2.1 Aeroelastic Model of the Very Flexible Blended-Wing-Body Aircraft

In this section, the process of creating the aeroelastic model of the very flexible BWB aircraft in finite elements is explained. This aircraft is part of the EcoJet Research Project developed in partnership with Bombardier and University of Victoria. A scaled model is shown in Figure 2.1. The project objective is to reduce aircraft carbon emissions by up to 50% through pioneering aircraft design concepts, specifically the adoption of the BWB configuration, while fostering skill transfer between academia and industry.

The GFEM of the very flexible BWB aircraft is used to determine the static response, modal characteristics, and coupled aeroelastic behaviour of the baseline aircraft model. These analyses are motivated by airworthiness and safety requirements mandated by regulatory authorities such as the FAA, EASA, and CARs [14–16]. In particular, certification requirements related to ultimate loading and aeroelastic stability (CS/CFR 25.301, CS/CFR 25.303 and CS/CFR 25.629 [33, 34]) are of primary importance for highly flexible and unconventional configurations.

This section provides an overview of the finite element method and its application to static and dynamic structural analyses, with specific focus on its implementation in NASTRAN.

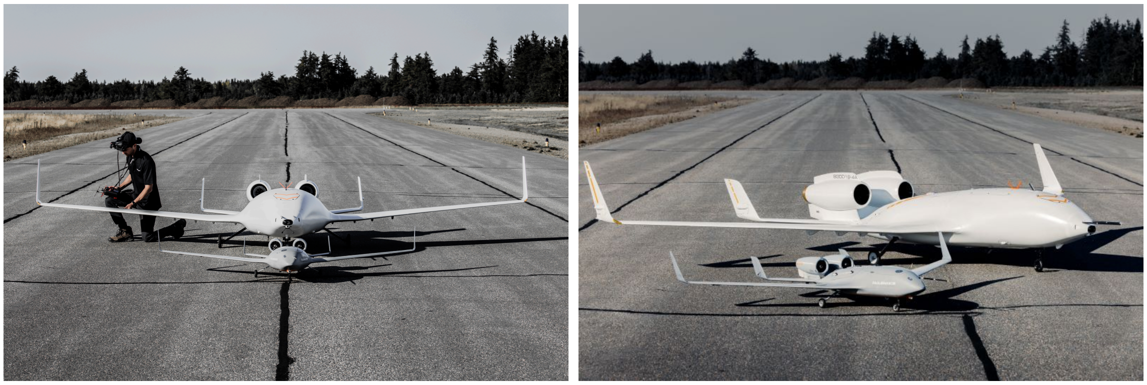

**Figure 2.1:** EcoJet flight demonstrator[60].

### 2.1.1 Baseline Aeroelastic Model

The finite element method (FEM) is used in a wide variety of disciplines and engineering applications. Many physical systems involve complex geometries, loadings, and material properties that make analytical solutions of the governing differential equations impractical, or even impossible. In such cases, numerical methods, such as the FEM provide approximate solutions.

The FEM involves discretizing a physical system into a finite number of elements interconnected at nodes. The structure is represented with element stiffness and mass matrices, which are assembled into global matrices to determine the equilibrium response of the airframe under applied loads. The aerodynamic lifting surfaces are discretized into panels or strips, and the resulting unsteady aerodynamic forces are expressed in terms of Aerodynamic Influence Coefficient (AIC) matrices that map structural motion to aerodynamic forces.

NASTRAN-compatible BDF files (Bulk Data File) were generated and organized into structural, mass, and aerodynamic models, with the objective of achieving an accurate yet computationally efficient representation of the very flexible BWB for subsequent static, modal, and aeroelastic analyses.

#### Structural Model

The structural model of the BWB aircraft is shown in Figure 2.2. It was constructed to accurately capture the stiffness distribution and load-transfer characteristics of the airframe.

The primary structural components of the aircraft, including skins, spars, ribs, and stringers, were meshed directly from CAD geometry using quadrilateral (CQUAD4) and triangular (CTRIA3) shell elements. Shell (PSHELL) and composite (PCOMP) property definitions were used to represent the fuselage, wing, winglet, and tail structures. The tail was connected to the fuselage using CBEAM elements. Isotropic materials (MAT1), such as aluminum, brass, and iron, and orthotropic materials (MAT8), such as carbon unidirectional, fiberglass, woven carbon, and foam cores, were assigned to each element in accordance with the CAD model and available design data. Mass density values were set to zero at this stage to decouple stiffness and inertia contributions.

A summary of the element typology and total number of elements used in the GFEM is provided in Table 2.1, offering an overview of the model size and level of discretization.

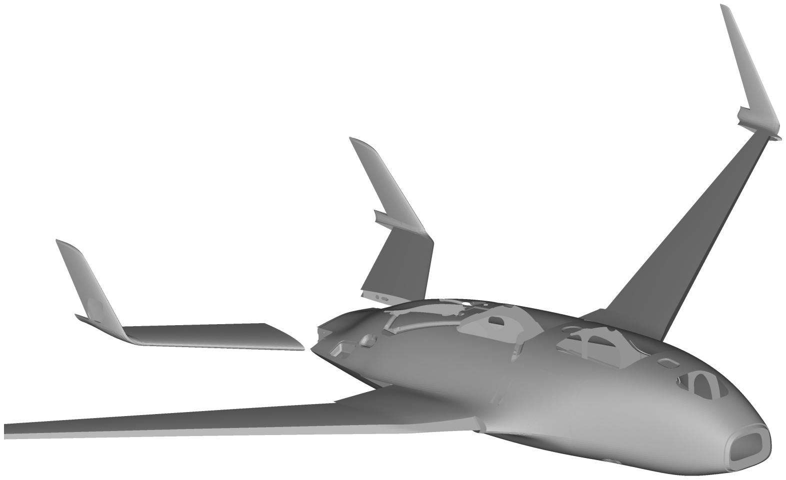

**Figure 2.2:** GFEM of the very flexible BWB aircraft scaled model.

### Mass Model

The mass representation of the BWB aircraft was used to ensure that the inertial properties of the model are consistent with the physical configuration. Instead of relying on a density-based approach, a lumped-mass formulation was adopted. This choice was motivated by three main considerations. First, lumped-mass models produce a much sparser global mass matrix, which reduces computational cost in static, modal and flutter analysis. Additionally, density-based models often introduce lo-

**Table 2.1:** Summary of elements used to define the GFEM model of the BWB aircraft

| **NASTRAN card** | Number of elements |
|---|---|
| GRID | 121248 |
| CBEAM | 51 |
| CQUAD4 | 112830 |
| CTRIA3 | 6566 |
| CBUSH | 4 |
| CONM2 | 44 |
| RBE2 | 446 |
| RBE3 | 74 |

cal unrealistic vibration modes that can contaminate aeroelastic analyses. Finally, a substantial fraction of the overall mass is linked with non-structural components, such as fuel, payload, systems, and onboard equipment thus it is not appropriate to try to link the non-structural mass to any structural stiffness model.

The lumped masses were defined using CONM2 elements, which allow the specification of concentrated masses and mass moments of inertia values at designated grid points. The mass model was constructed to reflect the actual layout of the fuselage, wing, winglet, and tail structures. Additional concentrated masses were introduced to represent different aircraft loading configurations across the operational envelope, including maximum take-off weight and zero-fuel weight conditions.

The resulting mass model is illustrated in Figure 2.3 and its global properties are summarized in Table 2.2.

An additional advantage of the lumped-mass formulation is its direct compatibility with the stick model developed in subsequent sections. Maintaining consistency in mass representation across modelling fidelities is essential for meaningful comparisons between the global finite element model and reduced order models.

### Aerodynamic Model

The aerodynamic lifting surfaces of the BWB considered in the aeroelastic analysis are shown in Figure 2.4. Unlike conventional wing-body-tail configurations, the BWB features an integrated lifting surface in which both the wing and the blended central body contribute to generate lift. As a result, the aerodynamic model represents a continuous planform comprising the wing, winglet, and fuselage. Vertical panels were additionally introduced to account for the fuselage thickness and volume effects. The

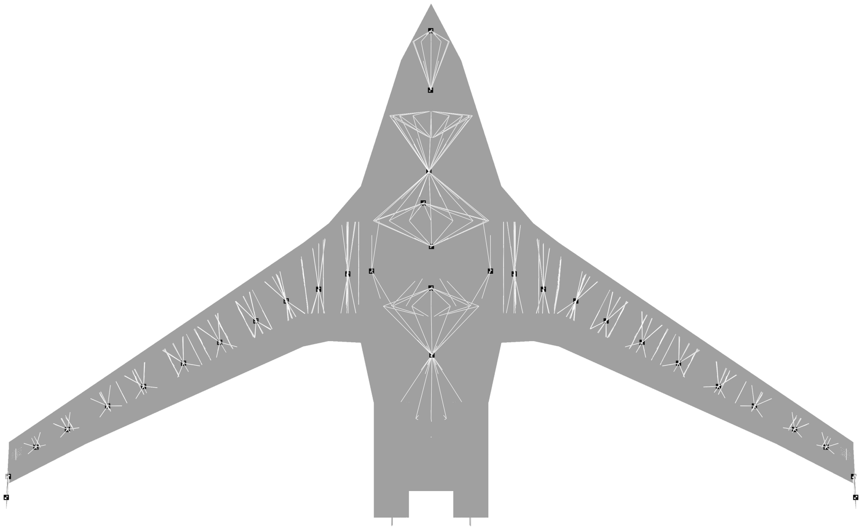

**Figure 2.3:** Mass locations of the BWB are shown in black while the rigid connections to the structure are represented by white lines.

unsteady aerodynamic forces acting on the BWB aircraft are computed using the Doublet-Lattice Method (DLM).

The lifting surfaces were discretized into a panel mesh using CAERO1 elements. The mesh near the leading and trailing edges was locally refined to accurately capture the unsteady aerodynamic response. By convention, all aerodynamic panels were oriented such that their local $x$–axes in the undeformed configuration are aligned with the free-stream direction.

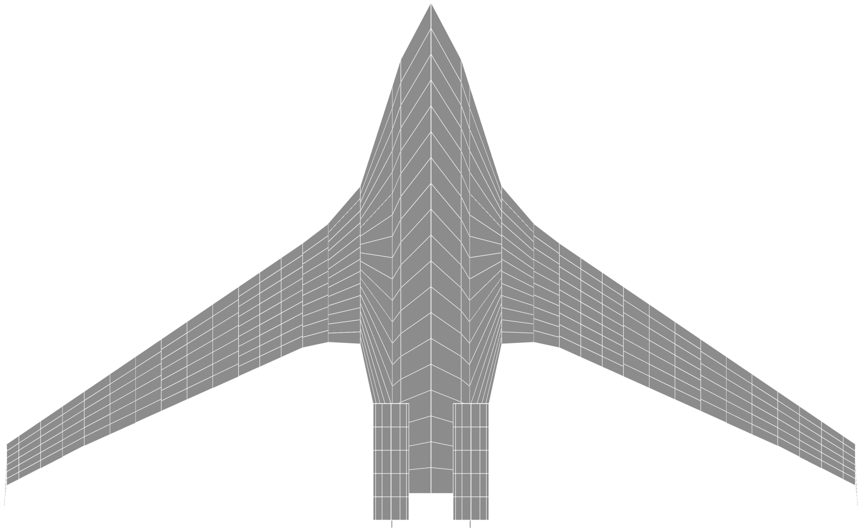

**Figure 2.4:** Aerodynamic model of the scaled BWB.

**Table 2.2:** Mass properties of the scaled BWB.

| **Mass properties** | **Component** | **Value** |
|---|---|---|
| Mass | - | 169.57 kg |
| CG location | $x$ | 1.84 m |
| | $y$ | 0.01 m |
| | $z$ | 0.00 m |
| Mass Moment of Inertia at CG | $xx$ | $93.77\,\mathrm{kg\,m^2}$ |
| | $yy$ | $168.57\,\mathrm{kg\,m^2}$ |
| | $zz$ | $80.95\,\mathrm{kg\,m^2}$ |
| | $xy$ | $0.05\,\mathrm{kg\,m^2}$ |
| | $xz$ | $-0.30\,\mathrm{kg\,m^2}$ |
| | $yz$ | $-0.06\,\mathrm{kg\,m^2}$ |

### Load Transferring, Rigid Connections and Aeroelastic Coupling

Accurate transfer of loads and displacements between different subsystems of the aeroelastic model is essential for a consistent representation of the BWB aircraft. Three main strategies were employed: rigid-body connections, motion interpolation, and aero-structure coupling.

RBE2 were introduced to represent rigid structural connections at wing-fuselage and wing-winglet junctions, ensuring that load transfer across these high-stiffness regions is accurately represented. These elements enforce kinematic constraints between dependent and independent nodes, preserving rigid-body motion and transmitting forces effectively.

RBE3 distributed the effect of concentrated masses (CONM2) onto the surrounding structural grid points. Unlike RBE2, RBE3 elements do not contribute stiffness. This strategy ensured that lumped masses were correctly coupled to the flexible structure while maintaining a realistic dynamic response.

The interaction between the aerodynamic and structural models was established through spline-based interpolation. SPLINE1 cards were used to interpolate structural deformations from the finite element structural model to the aerodynamic mesh, and to transfer distributed aerodynamic forces back to the structure.

### 2.1.2 Static, Dynamic, and Aeroelastic Analysis Framework

This section outlines the analysis framework adopted to evaluate the static, dynamic, and aeroelastic characteristics of the very flexible BWB aircraft. Static analysis is employed to calculate the structural response under ultimate load conditions; modal analysis is used to determine the natural frequencies and mode shapes; aeroelastic analysis focuses on assessing the flutter instabilities that arise from fluid-structure interaction. This section presents an overview of the analysis framework, in which each analysis is first introduced through its theoretical formulation and then applied to the baseline model.

The framework presented herein is applied to the baseline aeroelastic model developed in Section 2.1.1. Detailed results are presented in Section 3.1. These baseline results are the inputs for the optimization of the SM.

#### SOL101 - Static Analysis

Static analysis is used to determine the equilibrium structural response of the aircraft subjected to time-independent external loads and boundary conditions. Inertial and damping effects are neglected. For very flexible configurations, the static equilibrium problem is inherently nonlinear, as large deformations induce significant changes in geometry that alter the stiffness properties of the structure.

The static response is evaluated using the FE method, in which the structure is discretized into a finite number of interconnected elements joined at grid points. Each grid point is associated with six degrees of freedom. The stiffness contributions of individual elements, defined by their material properties, geometry, and formulation, are assembled into a global stiffness matrix that represents the overall resistance of the structure to deformation. Boundary conditions are imposed to prevent any rigid-body motion of the structure and obtain a well-posed equilibrium problem. The equilibrium of the constrained structure is governed by the finite element equation

$$\mathbf{K}\mathbf{u} = \mathbf{p}, \tag{2.1}$$

where $\mathbf{K}$ is the global stiffness matrix, $\mathbf{u}$ is the vector of unknown nodal displacement, and $\mathbf{p}$ is the applied load vector. The solution of this system is the displacement at each grid point, from which element strains, stresses, and internal forces are subsequently recovered on an element-by-element basis. These quantities form the basis for evaluating structural performance under static loading conditions.

A Python interface with NASTRAN was developed to automate the execution of static analyses. The workflow followed the standard structure of a NASTRAN input deck, which was divided into three main sections: executive control, case control, and bulk data. In the executive control section, the linear static solution SOL101 was specified, ensuring that the analysis treats all loads and displacements as time-independent.

In the case control section, the analysis subcases were defined. Boundary conditions were applied at the fuselage-wing interface using single-point constraints (SPC), restraining all six degrees of freedom at the attachment nodes to prevent rigid-body motion. A SET1 was created to recover displacements at selected grid points along the wing span.

In the bulk data section, the detailed finite element model was assembled. The structural stiffness and inertia properties were defined through the structural model, the mass model, and links introduced previously.

A dedicated subcase was created to evaluate the wing under ultimate loading conditions. According to certification standards (CS/CFR 25.301 and CS/CFR 25.303 [33, 34]), the ultimate load is defined as the limit load multiplied by a safety factor of 1.5, where the limit load represents the maximum loads expected during service. In this study, the limit load factors were defined as $+2.75$ and $-1.3$, after applying the safety factor, the corresponding ultimate load factors were $+4.125$ and $-1.95$, respectively. Forces were obtained from a previous CFD analysis conducted by Bombardier and provided for this work.

Table 2.3 summarizes the resulting normal forces, while Figure 2.5 illustrates the spanwise location of the applied loads. These loads are applied in the bulk data section using FORCE entries.

Detailed results are presented in Section 3.1, including the displacement at each grid point. These are later used for validation and comparison with the SM.

### SOL103 - Modal Analysis

The objective of dynamic analysis is to characterize the aeroelastic behaviour of the very flexible BWB aircraft; therefore, modal analysis is first performed to determine the fundamental dynamic properties of the system, which are required for subsequent aeroelastic coupling and flutter investigations.

Dynamic analysis differs from static analysis in two fundamental ways. First,

**Table 2.3:** Resulting normal forces of applied ultimate load

| **Station** | **Force** (N) |
|---|---|
| 1 | 621.49 |
| 2 | 93.69 |
| 3 | 184.67 |
| 4 | 148.93 |
| 5 | 132.73 |
| 6 | 152.49 |
| 7 | 107.39 |
| 8 | 46.02 |
| 9 | 125.46 |
| 10 | 166.73 |
| 11 | 61.99 |
| 12 | 152.84 |
| 13 | 59.24 |
| 14 | 145.96 |
| 15 | 88.20 |
| 16 | 82.33 |
| 17 | 83.70 |
| 18 | 78.44 |
| 19 | 126.19 |
| 20 | 59.54 |

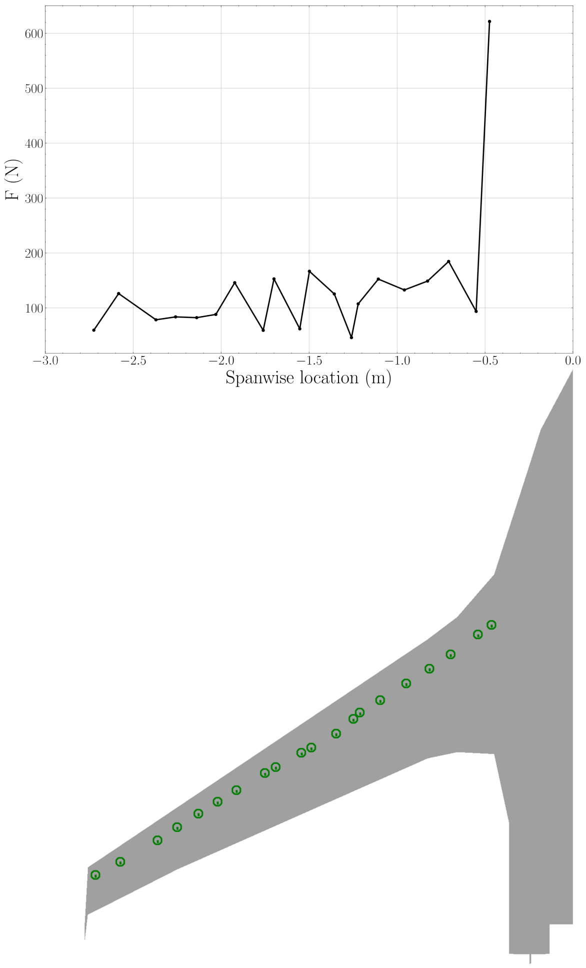

**Figure 2.5:** Spanwise locations and applied ultimate load

dynamic loads vary as a function of time or frequency. Second, the structural response is also time-dependent or frequency-dependent. These characteristics make dynamic analysis more complex, but also more realistic.

Equation 2.2 represents the equation of motion of a multi-degree-of-freedom undamped system in free vibration,

$$\mathbf{M}\ddot{\mathbf{u}} + \mathbf{K}\mathbf{u} = \mathbf{0} \tag{2.2}$$

where $\mathbf{M}$ and $\mathbf{K}$ are the global mass and stiffness matrices, respectively, and $\mathbf{u}$ and $\ddot{\mathbf{u}}$ denote the time-dependent displacement and acceleration vectors.

Modal analysis is performed to determine the fundamental dynamic characteristics of the undamped free-vibration system, that is, natural frequencies and mode shapes. These modal properties provide insight into the structural response to dynamic loading. Although damping is neglected at this stage, it may be included in other phases of the dynamic or aeroelastic analysis.

The problem reduces to the generalized eigenvalue equation

$$(\mathbf{K} - \omega^2\mathbf{M})\mathbf{u} = \mathbf{0} \tag{2.3}$$

where the eigenvalues $\omega^2$ correspond to the natural frequencies. The mass normalized eigenvectors $(U)$ represent the mode shapes of the structure and can be obtained by solving the homogeneous system.

Some important properties of eigenmodes are:

- Normal modes are orthogonal, that is, each mode shape is independent and cannot be expressed as a linear combination of other modes.
- For unconstrained (free-free) structures, rigid-body motion is possible. Each rigid-body degree of freedom is associated with a zero natural frequency, referred to as a rigid-body mode. Rigid-body modes are particularly relevant in the dynamic analysis of unconstrained aircraft structures.
- Mode shapes describe the relative deformation pattern but not the magnitude of the response. The magnitude of the structural response depends on the interaction between external excitation and the system's natural frequencies.

A Python interface with NASTRAN was developed to automate the execution of modal analyses. Similarly to a static analysis, the modal analysis workflow is divided into three main sections: executive control, case control, and bulk data. In the executive control section, the modal solution SOL103 is selected, which performs real eigenvalue extraction.

In the case control section, the analysis subcases were defined to represent two configurations with different boundary conditions. In the fixed fuselage configuration, SPCs were applied at the fuselage-wing interface to restrain all six degrees of freedom and eliminate rigid-body modes. In the free-free configuration, SPC entries were omitted, resulting in six rigid-body modes at near-zero frequency. A SET1 was created to recover displacements at selected grid points along the wing span and fuselage.

In the bulk data section, the detailed finite element model was assembled. The structural stiffness and inertia properties were defined through the structural model, the mass model, and links introduced previously. These inputs ensure consistency between the modal analysis and the static analysis presented earlier.

Eigenvalue extraction was carried out using the EIGRL entry, which specifies the Lanczos method. The Lanczos algorithm is the recommended approach in NASTRAN, as it combines efficiency with robustness and is well suited for large-scale models.

Detailed results are presented in Section 3.1, including the natural frequencies and corresponding mode shapes of the structure. These modal properties constitute the fundamental dynamic characteristics of the baseline model and are subsequently used for validation and comparison with the SM.

While modal analysis forms the foundation of the present wprk, other dynamic studies may be considered. Forced-response, tuned-discrete gust (TDG), and power spectral density (PSD) are examples of dynamic analyses beyond the scope of this thesis.

### SOL145 - Flutter Analysis

Aeroelasticity is the study of the interaction between aerodynamic, inertial, and elastic forces in a flexible structure. Collar's Aeroelastic Triangle in Figure 2.6 clearly illustrates its multidisciplinary nature.

Bisplinghoff established the classical distinction between static and dynamic aeroelastic phenomena, depending on wether inertial forces play a significant role. Static aeroelastic phenomena, such as divergence, are non-oscillatory in nature and arise from the interaction between aerodynamic and elastic forces. Dynamic aeroelastic

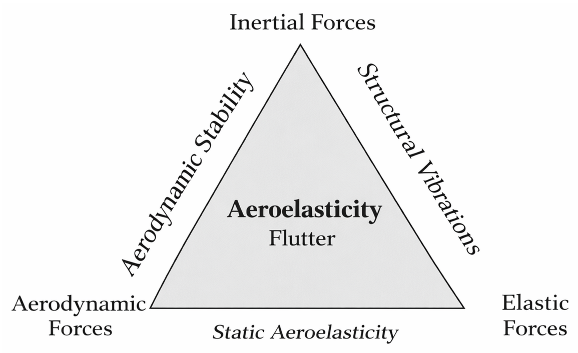

**Figure 2.6:** Collar's Aeroelastic Triangle (adapted from [9]).

phenomena, in contrast, result from the coupling of aerodynamic, elastic and inertial forces. Bisplinghoff emphasized that the dynamic instability known as flutter is the most critical aeroelastic phenomenon due to its potentially catastrophic nature.

Flutter is an unstable, self-excited oscillating phenomenon that arises from the adverse coupling of aerodynamic, inertial, and elastic forces, typically involving two or more vibration modes. Flexible modes may also interact with rigid-body dynamics (e.g., short-period motion), thereby affecting overall flight dynamics. Bending-torsion flutter (BTF) and body-freedom flutter (BFF) were reviewed in Section 1.2.1. A major challenge in flutter prediction is the unsteady nature of aerodynamic forces during oscillation and their feedback on the motion of the structure.

Certification requirements (CS/CFR 25.629 [33, 34]) mandate that flutter and divergence must not occur for any normal aircraft configuration or operating condition (including fuel state, ice, flight-control system settings, and thrust levels) within the flight envelope. Furthermore, the envelope must be enlarged by 15% ($V_D/M_D$ versus altitude envelope) to provide sufficient safety margins.

The homogeneous Equation 2.4 describes the fundamental coupled interaction between the flexible structure, aerodynamic forces, and the inertial effects associated with the system motion.

$$\mathbf{M}\ddot{\mathbf{q}} + (\rho V \mathbf{A_C}(k, M) + \mathbf{C})\dot{\mathbf{q}} + (\rho V^2 \mathbf{A_K}(k, M) + \mathbf{K})\mathbf{q} = \mathbf{0}, \tag{2.4}$$

where $\mathbf{M}$ is the global mass matrix, $\mathbf{C}$ and $\mathbf{K}$ are the structural damping and stiffness matrices, respectively; $\mathbf{A_C}$ and $\mathbf{A_K}$ are the aerodynamic damping and aerodynamic stiffness matrices; $\mathbf{q}$ is the vector of generalized modal coordinates; $\rho$ is the air density and $V$ is the air speed. The structural damping $\mathbf{C}$ is usually negligible in flutter analysis and can be omitted without loss of accuracy. The aerodynamic matrices $\mathbf{A_C}$ and

$\mathbf{A_K}$ are derived from the aerodynamic influence coefficient (AICs) matrices, which are calculated using the unsteady Doublet Lattice Method (DLM). These AIC matrices are complex-valued and depend on the aerodynamic mesh and flow parameters, namely the reduced frequency $k$ and Mach-number $M$.

The aerodynamic and structural models are generally discretized independently, that is, their grids are not necessarily coincident. Therefore, interpolation techniques (splining) are required to exchange information between them. In essence, splines serve two complementary roles:

1. Force interpolation, in which aerodynamic loads are transformed into equivalent structural forces.

2. Displacement interpolation, in which structural displacements are mapped onto the aerodynamic grid to update the lifting-surface displacements.

Equation 2.4 can be rewritten in the state-space form and the dynamic stability of the system, at a given flight condition (airspeed, mach value and altitude), can be assessed by solving the complex eigenvalue problem $(\mathbf{Q} - \lambda\mathbf{I})\mathbf{q} = \mathbf{0}$, where the system matrix $\mathbf{Q}$ is given by

$$\mathbf{Q} = \begin{bmatrix} \mathbf{0} & \mathbf{I} \\ -\mathbf{M}^{-1}(\rho V^2 \mathbf{A_K} + \mathbf{K}) & -\mathbf{M}^{-1}(\rho V \mathbf{A_C}) \end{bmatrix}, \tag{2.5}$$

$\mathbf{I}$ is the identity matrix and $\mathbf{0}$ is the zero matrix, $\lambda$ are the aeroelastic eigenvalues. The mass normalized aeroelastic eigenvectors ($U$) represent the mode shapes of the structure and can be obtained by solving the homogeneous system.

For aeroelastic systems, the eigenvalues generally occur in complex conjugate pairs, where the imaginary part defines the oscillation frequency and the real part determines the damping ratio and the overall stability of the system. If the eigenvalue is purely real, the response is non-oscillatory and corresponds to a static aeroelastic problem. A positive real part indicates instability: when associated with oscillatory modes, it manifests as flutter, whereas purely real positive eigenvalues indicate divergence.

Several classical methods are available for flutter analysis. The American flutter method (K-method) and its efficient variant (KE-method) are often used for rapid evaluations. The British flutter method (PK-method) has become the industry standard, because it provides a more realistic representation of unsteady aerodynamic loads.

The PK-method is a frequency-matching iterative scheme, applied to each aeroelastic mode and flight condition (airspeed, Mach number and altitude) of interest within the flight envelope:

1. Calculate the reduced frequency, $k = \omega b/V$, for the air speed/ frequency combination (often the previous airspeed is used, and an initial guess for the frequency of the mode is made).
2. Evaluate the aerodynamic stiffness and damping matrices $\mathbf{A_K}, \mathbf{A_C}$ using this reduced frequency.
3. Determine the frequencies for the system at this flight condition using the eigenvalue solution of the matrix shown in Equation 2.5.
4. Take the frequency solution closest to the initial guess made in 1 and repeat until convergence.

Once the frequency converges, extract the corresponding damping ratio. This procedure is repeated for each aeroelastic mode across all flight conditions of interest. The results are typically presented in $V{-}g$ and $V{-}f$ plots. The flutter speed is defined as the airspeed at which the damping is zero and it is graphically identified at the zero-crossing of the damping curve.

A Python interface with NASTRAN was developed to automate the execution of flutter analyses. Similarly to a static or a modal analysis, the flutter analysis workflow is divided into three main sections: executive control, case control, and bulk data. In the executive control section, the flutter solution SOL145 is selected, which performs a modal reduction of the structural model, computes the AIC matrices using the DLM, and evaluates the aeroelastic stability of the system.

In the case control section, the analysis subcases were defined. SPC entries were omitted to simulate free-free boundary conditions, ensuring that rigid-body modes are included in the modal basis. A SET1 was created to recover displacements at selected grid points along the wing span and fuselage.

In the bulk data section, the detailed finite element model was assembled. The structural stiffness and inertia properties were defined through the structural model, the mass model, and links introduced previously. These inputs ensure consistency between all analyses modules. Additionally, the aerodynamic model was defined, along with the spline connections that interpolate forces and displacements between the aerodynamic and structural grid points.

Eigenvalue extraction was carried out using the EIGRL entry with the Lanczos method to obtain the modal basis for the aeroelastic solution. This modal approach reduces the number of degrees of freedom while preserving the essential dynamic characteristics required for flutter analysis.

The AERO card defines the reference aerodynamic parameters and the unsteady Doublet Lattice Method (DLM) is used to compute aerodynamic influence coefficients (AIC) matrices. Splining techniques are used to transfer aerodynamic loads and structural displacements between the aerodynamic and structural grids. The aerodynamic forces are tranformed into modal coordinates to assemble the aerodynamic stiffness and damping matrices.

For computational efficiency, the AIC matrices are explicitly computed only at selected Mach numbers and reduced frequencies, specified using MKAERO1 tables. The FLUTTER card specifies the PKNL method as the iterative scheme. Aerodynamic matrices at intermediate reduced frequencies and Mach numbers are obtained through interpolation, while velocity and air-density variations are introduced through the explicit scaling terms in the aeroelastic equations using FLFACT tables.

Detailed results are presented in Section 3.1 in the form of $V$–$g$ and $V$–$f$ plots, which describe the evolution of modal damping and frequency with increasing airspeed. These plots are fundamental for assessing the aeroelastic stability of the system, including the flutter onset and the critical coupling between structural modes, unsteady aerodynamic forces and, system dynamics. Moreover, complex aeroelastic eigenvectors can be extracted to obtain the corresponding mode shapes, allowing identification of the critical modal coupling at the flutter condition. The aeroealstic behaviour of the baseline model is subsequently used for validation and comparison with the SM.

## 2.2 Optimization of Reduced Order Stick Models for Aeroelastic Analysis

The Finite Element Method (FEM) is widely used in aircraft structural design to calculate loads, stresses and deformations, predict structural dynamic response and evaluate aeroelastic stability. Depending on the level of fidelity required, aircraft structures may be represented either by detailed full finite element models (GFEM) or by simplified beam-based stick models. Section 1.2.4 reviewed the most common Model Order Reduction (MOR) techniques and justified the option for stick models over matrix based approaches.

### Full-Model Representation of Aircraft Components

Slender aircraft components, such as skins, spars, ribs, and stringers, are often meshed directly from CAD data using shell and beam elements. Section 2.1 explained in detail the creation of the high-fidelity model of the very flexible BWB aircraft, accurately capturing its geometry, material properties, and internal load transfer; this level of detail results in an extremely large numerical model, on the order of $10^6$ elements.

Simplified models are often employed and serve three main purposes:

1. **Reduced Computational Cost:** Dynamic and aeroelastic solutions are considerably time-consuming and memory-intensive. Using simplified models can drastically reduce the simulation time, making iterative studies feasible.

2. **Flexibility for Design Space Exploration:** Simplified models can be easily parameterized to study the influence of aerodynamic shape and structural stiffness in static, dynamic and aeroelastic solutions.

3. **Compatibility with Aeroelastic Solvers:** Tools like SHARPy or ASWING, widely used for nonlinear and unsteady aeroelastic simulations, require structural input in the form of beam-based models. Therefore, high-fidelity GFEM must be reduced or translated into a beam-compatible format.

Dynamic aeroelastic analyses are often preceded by some form of physical “condensation”. Reduced Order Models (ROM) aim to retain the essential static and dynamic characteristics of the system, while improving computational efficiency. Among the most common alternatives are beam-like models, also known as stick models.

### Beam-like Representation of Aircraft Components

Stick models (SM) represent the aircraft structure using a series of interconnected beam elements aligned with the structural elastic axis, typically coincident with wing spars. Each beam segment approximates the stiffness properties of the corresponding region in the original GFEM. Traditionally, the distributions of flexural and torsional rigidities (EI and GJ) along the wing span are estimated and then transferred to the stick model.

A large variety of methodologies for stick modelling have been reported in the literature, as reviewed in Section 1.2.4. Building on the foundational contributions of Dunn[136], Trivailo [137], Thomas [138] and Kose [139], this work presents a systematic optimization framework to calibrate SM such that they accurately reproduce the static deformation, dynamic response, and aeroelastic behaviour of the full model of the very flexible BWB aircraft.

The process begins with an initial representation of the stick, whose nodal layout follows the elastic axis of the airframe and is held fixed during optimization. To ensure consistency between the models, the original aerodynamic shape and mass distributions are preserved. The cross-sectional properties of each beam element are then identified as the design variables of the problem and presented in the next sections. Three optimization strategies are then introduced to refine the stiffness properties of the SM.

### 2.2.1 Initial Stick Model

To define the initial SM, the left-hand side of the BWB airframe is isolated and hereafter referred to as the wing GFEM. Three structural regions are defined: a rigid wing root, a flexible wing and a rigid winglet. The rigid regions of the wing GFEM, the central body and tail are not condensed into the stick model.

The flexible wing is discretized into 16 spanwise segments, or wing bays, each corresponding to a beam element in the stick model. For each wing bay, the geometric cross-sectional properties, namely cross-sectional area, area moments of inertia, torsional inertia, and shear factors, are computed analytically from the CAD geometry and used to populate 16 PBAR cards. These PBAR entries define the sectional stiffness properties of each beam element and are the design variables of the optimization problem. The material properties, namely Young's modulus and shear modulus, are defined globally using a MAT1 card, which is applied to all beam elements and remain constant during the optimization.

Owing to the geometric symmetry of the configuration, the left-hand side stick model is mirrored to represent the right-hand side of the wing. The two stick models

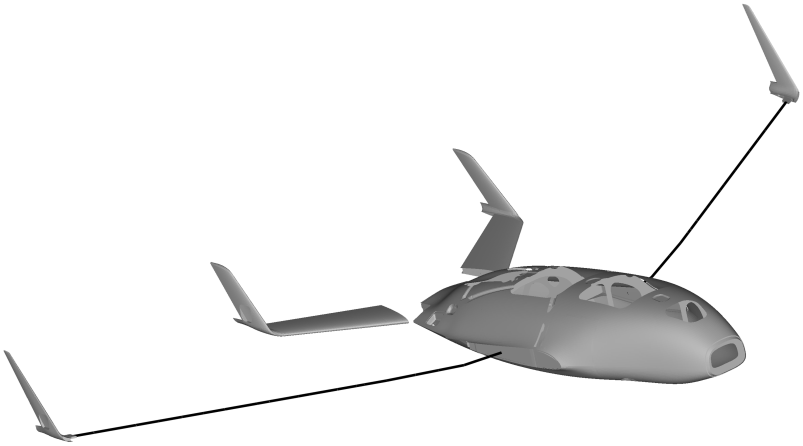

**Figure 2.7:** Hybrid model of the very flexible BWB aircraft.

replace the flexible wings of the full model, yielding a hybrid structural representation [116]. In this hybrid model, the central body, tail and other rigid regions are retained in their original GFEM form. This reduction is particularly well suited for parametric aeroelastic studies, as the wing stick model can be easily optimized and then parameterized without altering the detailed representation of the remaining airframe.

The lumped-mass representation adopted in the GFEM is transferred directly to the stick model, ensuring consistency between the two structural representations. With the mass distribution held fixed, differences in the solution of the eigenvalue problem in Equation 2.3 arise solely from discrepancies in the stiffness formulation. Therefore, if the stiffness matrix of the stick model is matched to that of the GFEM, the resulting elastic modal response (natural frequencies and mode shapes) of the two models will be equivalent, this is the objective of the modal optimization presented in Section 2.2.4.

Similarly, the aerodynamic model defined for the GFEM is coupled directly to the stick model for aeroelastic analysis. The aeroelastic eigenvalue problem of the SM, governed by the system matrix $\mathbf{Q}$ (Equation 2.5), can be tuned to match that of the full GFEM by optimizing the stiffness matrix of the SM, which is the objective of the aeroelastic optimization presented in Section 2.2.5. This formulation ensures consistency across structural and aerodynamic representations and allows a direct comparison between the aeroelastic responses of the reduced order and full models.

### 2.2.2 Design variables

The design variables of the optimization problem are the stiffness properties of each beam element:

$$\boldsymbol{p} = (A_{\mathrm{m}}, I_{1,\mathrm{m}}, I_{2,\mathrm{m}}, J_{\mathrm{m}}, k_{1,\mathrm{m}}, k_{2,\mathrm{m}}), \ \text{m=1, ..., 16} \tag{2.6}$$

where $\boldsymbol{p}$ is the vector of design variables, $A$ is the cross-sectional area, $I_1$ and $I_2$ are area moments of inertia, $J$ is the torsional constant, $k_1$ and $k_2$ are area factors for shear, and m identifies the beam element being evaluated.

All design variables are strictly positive and a tolerance parameter was included to avoid singularities.

$$A, I_1, I_2, J, k_1, k_2 > \mathrm{tol} = 1 \times 10^{-5} \tag{2.7}$$

Owing to the geometric symmetry of the configuration, the same 16 cards are mirrored to define the right-hand side stick model of the wing.

Three optimization methodologies are introduced to calibrate the stiffness properties of the stick model:

- **Case Study A**: The stick model is optimized to match the static deformation of the wing GFEM.

- **Case Study B**: The stick model is optimized to reproduce the elastic modal response of the wing GFEM.

- **Case Study C**: The stick model is optimized to replicate the aeroelastic behaviour of the full GFEM.

The optimization framework repeatedly executes NASTRAN to perform static, modal, and aeroelastic analyses. To reduce the associated computational cost, the optimization is parallelized using the optimParallel package developed by Gerber [140]. Given sufficient system memory is available, this approach can speed up the process up to a factor of $1 + p$, where $p$ is the number of available processing cores. The *L-BFGS-B* algorithm is adopted due to its efficient handling of bound-constrained problems and its compatibility with the parallel optimization framework.

### 2.2.3 Case Study A: Static Optimization Methodology

A stick model is developed to represent a complex GFEM of a wing. The stiffness properties of the stick model, namely cross-sectional areas, area moments of inertia, torsional inertia, and shear factors, are optimized to reproduce the static response of the wing GFEM. The objective of the optimization is to minimize the error in displacement at selected GRID points between the reduced order and full models, under equivalent loading and boundary conditions.

The wing GFEM and the initial stick model are cantilevered at the wing root to avoid rigid body motion. Throughout the optimization, a realistic load case - corresponding to a limit loading condition - is applied consistently to both models. The resulting vertical displacement ($\Delta y$) and twist ($\Delta\theta$) are then compared to evaluate the accuracy of the stick model. Deformations are evaluated at coincident GRID points, defined at the beam junctions of the stick model. To ensure compatibility, corresponding GRID points were created in the GFEM and connected to the surrounding structure using RBE3 elements.

The static analysis framework described in Section 2.1.2 is first applied to the wing GFEM to establish the reference deformation response. These results are presented in Section 3.1. The same framework is then applied to the stick model within the optimization loop, with the objective of matching the static deformation of the wing GFEM.

The objectives of Static Optimization are to minimize the Vertical Displacement RMS Error ($E_y$) and minimize the Twist RMS Error ($E_\theta$) between the reduced order and full models. A normalized error function (RMS) is introduced to quantify the difference in static response, such that the error contribution from each GRID point is weighted equally. The objective function is therefore formulated as:

$$\begin{gathered}
\min \mathrm{f}(\boldsymbol{p}) = w_y E_y(\boldsymbol{p}) + w_\theta E_\theta(\boldsymbol{p}), \\
E_y = \sqrt{\frac{1}{n}\sum_{i=1}^{n}\left(\frac{\Delta y_{\mathrm{S}}(\boldsymbol{p})_{,i} - \Delta y_{\mathrm{G},i}}{\Delta y_{\mathrm{G},i} + \delta}\right)^2}, \\
E_\theta = \sqrt{\frac{1}{n}\sum_{i=1}^{n}\left(\frac{\Delta \theta_{\mathrm{S}}(\boldsymbol{p})_{,i} - \Delta \theta_{\mathrm{G},i}}{\Delta \theta_{\mathrm{G},i} + \delta}\right)^2},
\end{gathered} \tag{2.8}$$

where f is the objective function, $\boldsymbol{p}$ is the vector of design variables, $w_y$ and $w_\theta$ are the weight coefficients, $i$ refers to the GRID point being evaluated, while $n$ is the total number of GRID points being evaluated, $\Delta y$ is the vertical displacement and $\Delta\theta$ is the twist, the subscript S refers to the stick model and the subscript G refers to the GFEM, $\delta = 1 \times 10^{-10}$ is a safety parameter to avoid singularities.

A flowchart of the objective function can be seen in Figure 2.8.

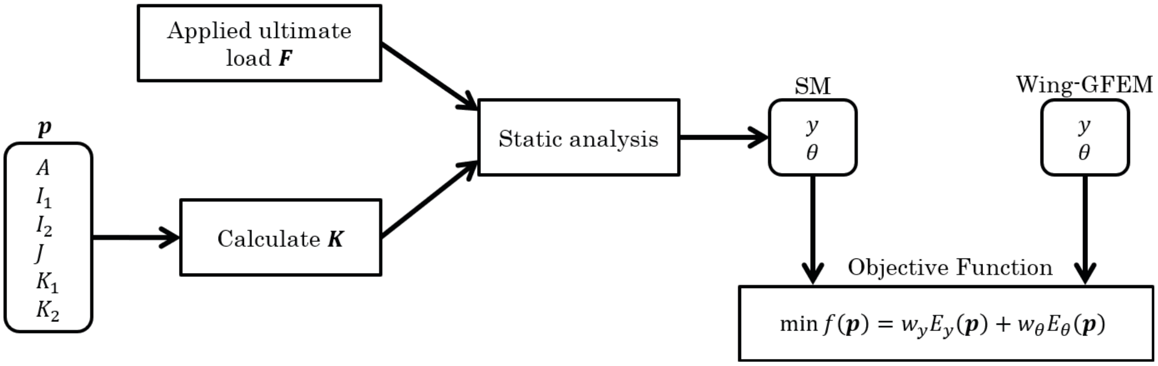

**Figure 2.8:** Objective function flowchart for Case Study A.

### 2.2.4 Case Study B: Modal Optimization Methodology

A stick model is developed to represent a complex GFEM of a wing. The stiffness properties of the stick model, namely cross-sectional areas, area moments of inertia, torsional inertia, and shear factors, are optimized to reproduce the modal response of the wing GFEM. The objectives of the optimization are to minimize the error in natural frequencies, maximize the compatibility of equivalent mode shapes, and minimize discrepancies in the relative coupling between vibration modes observed in the reduced order and full models.

Both the wing GFEM and the initial stick model are cantilevered at the wing root to eliminate rigid body modes. During the optimization, the eigenvalue problem is solved for each model. The resulting natural frequencies, crossMACX matrices and autoMACX matrices are then compared to assess the accuracy of the stick model.

The modal analysis framework described in Section 2.1.2 is first applied to the wing GFEM to establish the reference natural frequencies and mode shapes. These results are presented in Section 3.1. The same framework is then applied to the stick model within the optimization loop, with the objective of reproducing the elastic modal response of the wing GFEM.

Natural frequencies and mode shapes of equivalent modes are compared. The

Modal Assurance Criterion (MAC) is used to compare the eigenmodes of the stick model and wing GFEM. According to this criterion, identical mode shapes yield MAC values close to 1, whereas dissimilar modes approach zero. For consistency, the eigenvectors of the wing GFEM are reduced to the same set of structural nodes used in the stick model, and the same number of eigenmodes is retained in both models.

To prevent mode swapping, a mode tracking algorithm was developed using the MAC criterion [141, 142]. A crossMAC matrix is assembled to compare the eigenvectors of the stick model and the wing GFEM. The largest crossMAC values are identified and the most compatible modes across models are paired, within the tracking routine.

Natural frequencies identify the excitation frequencies at which vibration amplitudes are amplified - resonance phenomena. Differences between the reduced order and full models are penalized with an error during optimization.

Ideally, the crossMAC matrix after tracking is diagonal. However, if the mode shapes of corresponding modes are not perfectly equivalent, the associated diagonal terms of the crossMAC matrix deviate from unity. The trace of the crossMAC matrix is maximized toward the number of modes evaluated and any deviation from this ideal value (total number of modes) is treated as an error. Meanwhile, off-diagonal terms may be non-zero because modes are not purely associated with a single deformation mechanism, which is characteristic of complex structural systems.

Additionally, autoMAC matrices are assembled for both models. The autoMAC matrix is constructed by correlating each mode shape of a model with all other modes of the same model. The autoMAC of the GFEM serves as a reference description of how vibration modes couple with each other, while the SM seeks to reproduce these inter-modal relationships. Any discrepancies between the two autoMAC matrices are treated as errors.

The objectives of Modal Optimization are to minimize the Natural Frequency RMS Error ($E_f$), minimize the CrossMAC Trace Error ($E_c$) and minimize the AutoMAC RMS Error ($E_a$). All error functions are normalized, but can be weighted differently in the objective function. The objective function is therefore formulated as:

$$
\begin{aligned}
\min \mathrm{f}(\boldsymbol{p}) &= w_f E_f(\boldsymbol{p}) + w_c E_c(\boldsymbol{p}) + w_a E_a(\boldsymbol{p}),\\
E_f &= \sqrt{\frac{1}{m}\sum_{j=1}^{m}\left(\frac{f_{\mathrm{S}}(\boldsymbol{p})_{,j} - f_{\mathrm{G},j}}{f_{\mathrm{G},j} + \delta}\right)^2},\\
E_c &= 1 - \frac{\mathrm{trace}(\mathrm{crossMAC}(\boldsymbol{p}))}{m},\\
E_a &= \sqrt{\frac{1}{m}\frac{1}{m}\sum_{i=1}^{m}\sum_{j=1}^{m}\left(\mathrm{autoMAC}_{\mathrm{S}}(\boldsymbol{p})_{,ij} - \mathrm{autoMAC}_{\mathrm{G},ij}\right)^2},
\end{aligned}
\tag{2.9}
$$

where f is the objective function, $\boldsymbol{p}$ is the vector of design variables, $w_f$, $w_c$ and $w_a$ are the weight coefficients, $i$ and $j$ refer to the mode being evaluated, while $m$ is the total number of modes being evaluated, $f$ is the natural frequency, the subscript S refers to the stick model and the subscript G refers to the GFEM, $\delta = 1 \times 10^{-10}$ is a safety parameter to avoid singularities.

A flowchart of the objective function can be seen in Figure 2.9.

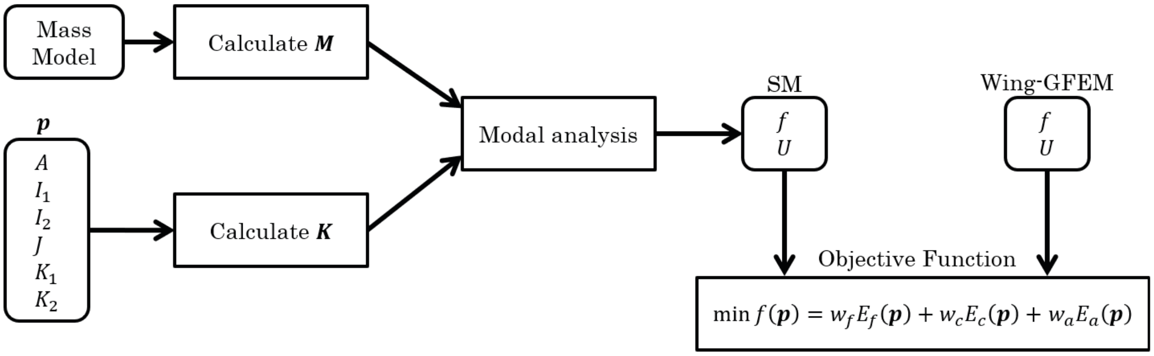

**Figure 2.9:** Objective function flowchart for Case Study B.

### 2.2.5 Case Study C: Aeroelastic Optimization Methodology

A hybrid structural model is developed to represent a complex GFEM of an aircraft. The stiffness properties of the stick model, namely cross-sectional areas, area moments of inertia, torsional inertia, and shear factors, are optimized to replicate the aeroelastic behaviour of the baseline GFEM. The objectives of the optimization are to minimize the error in aeroelastic frequencies and damping across the flight envelope, and to minimize discrepancies in the relative coupling between aeroelastic modes at flutter point observed in the reduced order and full models.

Both the baseline GFEM and the initial hybrid model are in free flight condition to include rigid body modes. During the optimization, the complex eigenvalue problem is solved for each model. The resulting complex eigenvalues, crossMACX matrices and autoMACX matrices are then compared to assess the accuracy of the stick model.

The aeroelastic analysis framework described in Section 2.1.2 is first applied to the GFEM to establish the reference complex eigenvalues and mode shapes. These results are presented in Section 3.1. The same framework is then applied to the hybrid model within the optimization loop, with the objective of replicating the aeroelastic behaviour of the GFEM.

Eigenvalues and mode shapes of equivalent aeroelastic modes are compared between the hybrid model and the baseline GFEM. To account for the complex nature of the aeroelastic eigenvectors, the Modal Assurance Criterion applied to complex vectors (MACX) [142] is employed as a phase-invariant measure of modal similarity. In this formulation, MACX values close to 1 indicate strongly correlated complex modes, whereas values approaching zero correspond to weakly related or orthogonal modes. For consistency, the eigenvectors of the GFEM are reduced to the same set of structural nodes used in the stick model, including selected fuselage nodes, and the same number of eigenmodes is retained in both models.

To prevent mode swapping, a mode tracking algorithm was developed using the MACX criterion [142]. A crossMACX matrix is assembled to compare the complex eigenvectors of the stick model and the wing GFEM. The largest crossMACX values are identified and the most compatible modes across models are paired, within the tracking routine.

Aeroelastic frequencies and damping characterize the oscillatory behaviour and stability of the coupled fluid-structure system and are captured by the complex eigenvalues of the aeroelastic modes. In radio-frequency engineering, Error Vector Magnitude (EVM) has been established as an effective metric to compare complex-valued signals [143, 144]. By analogy, the EVM concept is used here to quantify differences between the aeroelastic eigenvalues of the hybrid model with those of the baseline GFEM.

The autoMACX matrix correlates each mode shape of a model with all other modes of the same model. Ideally, the autoMACX matrix is diagonal. However, if a mode is not monophase, the diagonal term of the autoMACX matrix may deviate from 1. Meanwhile, off-diagonal terms may be non-zero because modes are not purely associated with a single deformation mechanism.

In contrast with Case Study B, the diagonal values of the crossMACX matrix of aeroelastic systems are not expected to be 1, due to the complex nature of the eigenmodes. Consequently, the CrossMAC Trace Error ($E_C$) is not applicable in this context. Instead, the diagonal terms of the autoMACX matrix of the baseline GFEM are used as the reference. In the same manner, the off-diagonal terms of the crossMACX matrix are evaluated relative to the off-diagonal terms of the autoMACX matrix of the baseline GFEM. Accordingly, a single error metric is introduced to compare the mode shapes of the two models at flutter point, which quantifies discrepancies between the crossMACX matrix of the two models with the autoMACX matrix of the baseline GFEM.

The objectives of Aeroelastic Optimization are to minimize the Complex Eigenvalue EVM Error ($E_e$) and minimize the Complex Eigenvector Error ($E_x$). All error functions are normalized, but can be weighted differently in the objective function. The objective function is therefore formulated as:

$$
\begin{aligned}
\min \mathrm{f}(\boldsymbol{p}) &= w_e E_e(\boldsymbol{p}) + w_x E_x(\boldsymbol{p}), \\
E_e &= \frac{\sqrt{\frac{1}{m}\frac{1}{n}\sum_{k=1}^{n}\sum_{i=1}^{m}\left|\lambda_H(\boldsymbol{p})_{,ik} - \lambda_{\mathrm{G},ik}\right|^2}}{\sqrt{\frac{1}{m}\frac{1}{n}\sum_{k=1}^{n}\sum_{i=1}^{m}\left|\lambda_{\mathrm{G},ik}\right|^2} + \delta}, \\
E_x &= \sqrt{\frac{1}{m}\frac{1}{m}\sum_{i=1}^{m}\sum_{j=1}^{m}\left(\mathrm{autoMACX}_{\mathrm{G},ij} - \mathrm{crossMACX}_S(\boldsymbol{p})_{,ij}\right)^2},
\end{aligned}
\tag{2.10}
$$

where f is the objective function, $\boldsymbol{p}$ is the vector of design variables, $w_e$ and $w_x$ are the weight coefficients, $i$ and $j$ refer to the mode being evaluated, while $m$ is the total number of aeroelastic modes, $k$ refers to the flight point being evaluated, while $n$ is the total number of flight conditions, $\lambda$ is the complex eigenvalue, the subscript H refers to the hybrid model and the subscript G refers to the baseline GFEM, $\delta = 1 \times 10^{-10}$ is a safety parameter to avoid singularities.

A flowchart of the objective function can be seen in Figure 2.10.

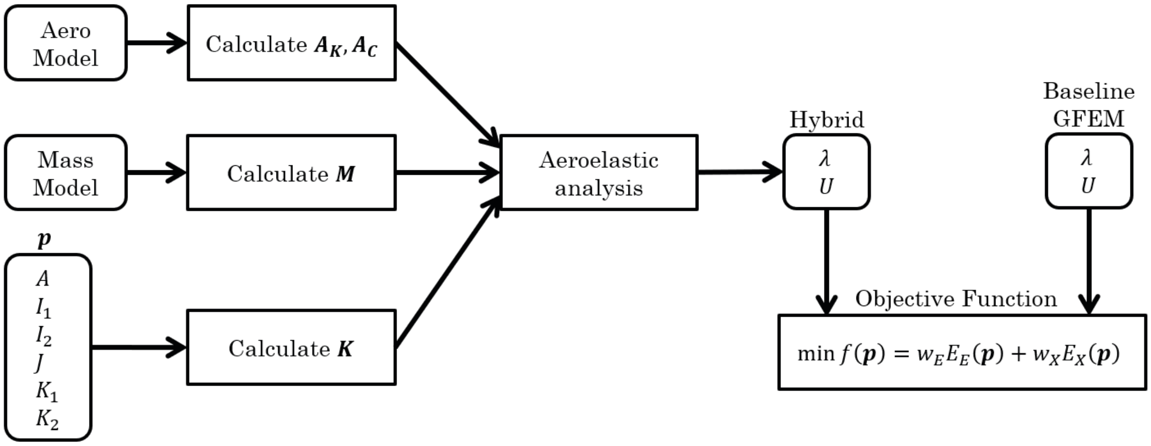

**Figure 2.10:** Objective function flowchart for Case Study C.

## 2.3 Aeroelastic Tailoring of the Very Flexible BWB Aircraft to Study Flutter Mechanisms

In the present work, aeroelastic tailoring is adopted within a parameterization framework to investigate flutter mechanisms in a very flexible blended-wing-body (BWB) aircraft. During the early stages of conceptual aircraft design, the configuration undergoes multiple modifications within a highly iterative process, in which key parameters of aerodynamic shape and structural properties are systematically varied. The present parameterization framework is used to explore the design space of the BWB configuration and to investigate the influence of selected parameters on the governing flutter mechanisms, as well as on the resulting flutter onset speed.

The structural parameterization is applied to the simplified stick model. As discussed previously in Section 2.2, SM are particularly well suited for iterative schemes, such as the present parameterization study, because of their low computational cost and simplified physical representation.

A set of parameters that affect aerodynamic shape and structural properties is selected to define the design space. Table 2.4 lists the fixed parameters used in the analysis, along with the nominal values of the design variables of the baseline BWB configuration. Table 2.5 summarizes the selected design variables and their respective ranges around the baseline configuration used in the Design of Experiments (DOE). To ensure the best coverage of the design space, the tested values are evenly spaced within their predefined range and only one design variable is varied at a time. A total of 600 configurations are evaluated by varying each of the six design variables independently over hundred discrete design points; the remaining parameters are held fixed at their nominal values.

**Table 2.4:** Nominal values for relevant parameters of the wing stick model.

| Type | Parameter | Description | Value |
|---|---|---|---|
| Stick geometry | $N_{ws}$ | No. of wing stations | 16 |
| | $x_{\text{EA}}$* | Elastic axis | 40–45%c |
| Material properties | E* | Young's modulus | 70 GPa |
| | G* | Shear modulus | 26 GPa |
| Mass properties | $m$ | Mass | 169.57 kg |
| | $x_{\text{CG}}$ | CG from nose | 1.84 m |
| Aerodynamic shape | $\Lambda_{c/4}$* | Sweptback angle | 32.84° |
| | $\phi$* | Dihedral angle | 3.36° |
| | AR* | Aspect ratio | 8.55 |
| | $\lambda$ | Taper ratio | 0.21 |
| | S | Reference area | $3.60\,\text{m}^2$ |
| | $b$ | Wing span | 5.55 m |
| | $\bar{c}$ | Mean chord | 0.65 m |
| Flight condition | $\rho$ | Air density | $1.167\,\text{kg/m}^3$ |
| | $h$ | Altitude | 500 m |

Parameters marked with * denote design variables.

**Table 2.5:** Wing design variables

| Variable | Description | Lower bound | Upper bound | Design points | Card | Modified coordinate |
|---|---|---|---|---|---|---|
| $\Lambda_{c/4}$ 🟦 | Sweptback angle | 21° | 45° | 100 | CAERO1 | $x_4$ |
| $\phi$ 🟧 | Dihedral angle | 0.35° | 6.35° | 100 | CAERO1 | $y_4$ |
| AR 🟩 | Aspect ratio | 6.55 | 10.55 | 100 | CAERO1 | $z_4$ |
| EI 🟥 | Bending stiffness | 10% | 190% | 100 | MAT1 | $E$ |
| GJ 🟪 | Torsional stiffness | 40% | 160% | 100 | MAT1 | $G$ |
| $x_{\text{EA}}$ 🟫 | Elastic axis | $-0.4c_{\text{tip}}$ | $0.6c_{\text{tip}}$ | 100 | GRID | $x$ |

### 2.3.1 Aerodynamic Shape Parameterization Framework

A nondimensional parameter $k$ is introduced to control the geometric variation of the wing. The baseline configuration corresponds to $k = 1$, while $k = 0$ defines the lower bound of each parameter, typically representing a limiting or degenerate case (for example, zero sweep or a flat wing).

Parameter $k$ is calculated globally for each targeted wing geometry and applied locally to every CAERO panel, from root to tip. Depending on the parameter under evaluation, a vertex coordinate at the tip $(x, y, z)$ is modified according to

$$x_{\text{new}} = x_{\text{lb}} + (x_{\text{ub}} - x_{\text{lb}})\,k, \tag{2.11}$$

where $x_{\text{new}}$ is the coordinate of the parameterized geometry, $x_{\text{ub}}$ is the coordinate in the baseline configuration (upper bound), and $x_{\text{lb}}$ is the coordinate in the limiting configuration (lower bound).

To ensure continuity across the aerodynamic surface, after each local modification, the adjacent panel is repositioned based on the updated leading-edge coordinates and the chord value of the preceding panel.

#### Parameter $\Lambda_{c/4}$: Sweptback Angle

The nominal sweptback angle is the mean quarter-chord sweep of the baseline wing. In the parameterization process, target values for the sweep are specified as $\Lambda_{c/4} \in [21^\circ, 45^\circ], \quad \Delta\Lambda_{c/4} = 0.24^\circ$. For each target, $k$ is computed relative to the nominal geometry, and the longitudinal coordinate of the tip vertex ($x_4$) of each panel is adjusted proportionally to $k$. This process increases or decreases the local sweep. Continuity is ensured by repositioning subsequent panels based on the updated leading-edge geometry. Figure 2.11 shows the parameterized aero-structural model.

#### Parameter $\phi$: Dihedral Angle

The nominal dihedral angle is defined at the quarter-chord line of the baseline wing. In the parameterization process, target values for the dihedral are specified as $\phi \in [0.35^\circ, 6.35^\circ], \quad \Delta\phi = 0.06^\circ$. For each target, $k$ is computed relative to the nominal geometry, and the vertical coordinate of the tip vertex ($y_4$) of each panel is modified according to $k$. This process increases or decreases the inclination of each panel to achieve the desired dihedral. Continuity is ensured by repositioning subsequent panels based on the updated leading-edge geometry.

### Parameter AR: Aspect Ratio

The nominal aspect ratio is the ratio of wing span to mean aerodynamic chord of the baseline configuration. In the parameterization process, target values for aspect ratio are specified as $\mathrm{AR} \in [6.55, 10.55], \quad \Delta\mathrm{AR} = 0.04$. For each target, $k$ is computed relative to the nominal geometry, and the transverse coordinate of the tip vertex ($z_4$) of each panel is modified according to $k$. This process scales the total span while preserving the mean aerodynamic chord. Local sweep and dihedral angles are adjusted automatically to preserve geometric consistency. Continuity is ensured by repositioning subsequent panels based on the updated leading-edge geometry. Figure 2.12 shows the parameterized aero-structural model.

### Structural Mapping to the Parameterized Aerodynamic Shape

These parameterizations directly affect the aerodynamic shape. To maintain aero-structural consistency, the structural and mass models are mapped onto the updated aerodynamic geometry. Each GRID point of the stick model and each CONM2 element of the lumped-mass model is first located in the baseline aerodynamic model, using normalized spanwise, chordwise and thicknesswise coordinates. These coordinates are then used to relocate the corresponding points in the parameterized geometry, ensuring that the structural stiffness and mass distributions follow the modified aerodynamic shape without altering their relative positioning.

## 2.3.2 Structural Properties Parameterization Framework

### Parameter EI: Bending Stiffness

Bending stiffness quantifies the resistance of a structure to bending deformation under applied loads and is defined as the product of the material Young's modulus (E) and the area moment of inertia ($I_x$) of the cross section about the bending axis. In the parameterization process, target values for the relative variation of the bending stiffness are specified as $\mathrm{EI} \in [10\%, 190\%]\mathrm{EI}_{\mathrm{baseline}}, \quad \Delta\mathrm{EI} = 1.8\%\mathrm{EI}_{\mathrm{baseline}}$. Values below 100% correspond to a reduction in bending stiffness relative to the baseline configuration, while values above 100% represent an increase. In practice, these variations are implemented by modifying the Young's modulus of the materials, while the area moment of inertia is kept constant. A particular characteristic of the stick model is that all beam elements share the same material properties, which are defined through MAT1 cards. This approach allows bending stiffness to be varied without altering the geometry of the models cross-sections.

### Parameter GJ: Torsional Stiffness

Torsional stiffness quantifies the resistance of a structure to twisting about the elastic axis under applied loads and is defined as the product of the material shear modulus (G) and the torsional constant (J) of the cross section. In the parameterization process, target values for the relative variation of the torsional stiffness are specified as $\mathrm{GJ} \in [40\%, 160\%]\mathrm{GJ}_{\mathrm{baseline}}, \quad \Delta\mathrm{GJ} = 1.2\%\mathrm{GJ}_{\mathrm{baseline}}$. Values below 100% correspond to a reduction in torsional stiffness relative to the baseline configuration, while values above 100% represent an increase. In practice, these variations are implemented by modifying the shear modulus of the materials, while the torsional constant is held fixed. A particular characteristic of the stick model is that all beam elements share the same material properties, which are defined through MAT1 cards. This approach allows torsional stiffness to be varied without altering the geometry of the models cross-sections.

### Parameter EA: Elastic Axis Position

The elastic axis is a reference line along which bending deformation occurs without inducing torsion [29]. It is a structural property determined by the stiffness distribution of the cross-section and is independent of aerodynamic loading. In the parameterization process, target values for the relative position of the elastic axis are specified as $x_{\mathrm{EA}} \in [-0.4, 0.6]c_{\mathrm{tip}}, \quad \Delta x_{\mathrm{EA}} = 0.01c_{\mathrm{tip}}$. Positive values correspond to an aft movement of the elastic axis towards the trailing edge, while negative values represent a forward shift towards the leading edge. The elastic axis displacement is normalized by the chord length at the wing tip. In practice, these variations are implemented by modifying the $x$-coordinate of the structural GRID points of the model, while ensuring that all nodes remain within the aerodynamic planform to preserve the physical feasibility of the resulting configuration. Figure 2.13 shows the parameterized aero-structural model.

(a) $\Lambda_{c/4} = 21°$. (b) $\Lambda_{c/4} = 32.84°$. (c) $\Lambda_{c/4} = 45°$.

**Figure 2.11:** Variation of sweptback angle on the aero-structural model.

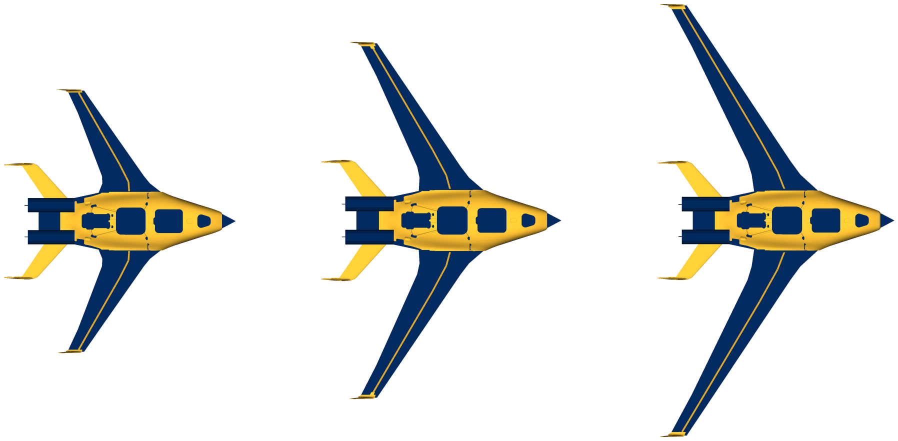

(a) $\mathrm{AR} = 6.55$. (b) $\mathrm{AR} = 8.55$. (c) $\mathrm{AR} = 10.55$.

**Figure 2.12:** Variation of aspect ratio on the aero-structural model.

(a) $x_{\mathrm{EA}} = -0.4c_{\mathrm{tip}}$. (b) $x_{\mathrm{EA}} = 0$. (c) $x_{\mathrm{EA}} = 0.6c_{\mathrm{tip}}$.

**Figure 2.13:** Variation of position of elastic axis on the aero-structural model.

# Chapter 3

# Results and Discussion

## 3.1 Reference Results of the Very Flexible Blended-Wing-Body Aircraft

This section presents the structural response of the reference wing GFEM and the full model, which serves as the benchmark for validating the simplified stick model. The results include static deflection, modal characteristics, and aeroelastic behaviour of the baseline model.

### 3.1.1 Wing GFEM

#### Static Analysis

The wing GFEM is cantilevered at the wing root and subjected to the ultimate load, which corresponds to the maximum aerodynamic load expected during service multiplied by a safety factor of 1.5 (CS/CFR 25.301, CS/CFR 25.303[33, 34]). The discretized load distribution was shown in Figure 2.5. Figure 3.1 illustrates the static deformation under this condition.

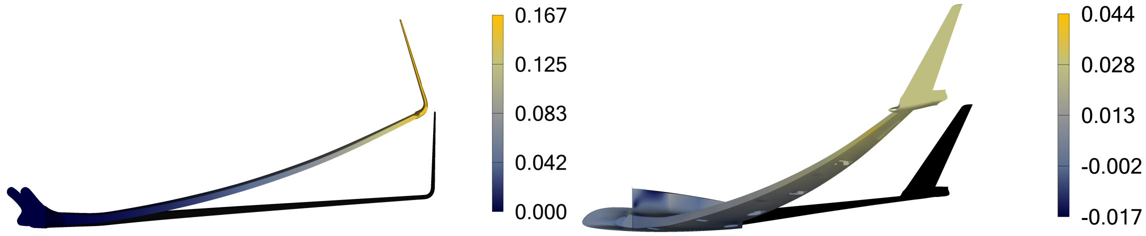

**(a)** Vertical displacement ($\Delta y$) in meters.

**(b)** Twist ($\Delta\theta$) in radians.

**Figure 3.1:** Static deformation of the wing GFEM in comparison with the undeformed configuration (shaded). For reference, the wing semi-span length is 2.31 m.

### Modal Analysis

A modal analysis is then performed to determine the natural frequencies and corresponding mode shapes of the cantilevered wing. The first five elastic modes are extracted, and the eigenvectors are used to compute the autoMAC matrix. Table 3.1 summarizes the modal characteristics, while Figure 3.2 depicts the corresponding mode shapes in two views.

Each mode is examined through its animated deformation and correlated with others using the autoMAC matrix (Figure 3.3). The autoMAC helps confirm the modal purity, identify harmonics and potential coupling between modes.

**Table 3.1:** Modal behaviour of the reference cantilevered wing GFEM.

| Mode | Label | $f$ (Hz) | Description |
|---|---|---|---|
| 1 | OB1 | 5.45 | First out-of-plane bending |
| 2 | T1 | 13.93 | First torsion |
| 3 | OB2 | 16.44 | Second out-of-plane bending |
| 4 | IB-T | 26.88 | Coupled in-plane bending-torsion |
| 5 | T2 | 27.98 | Second torsion |

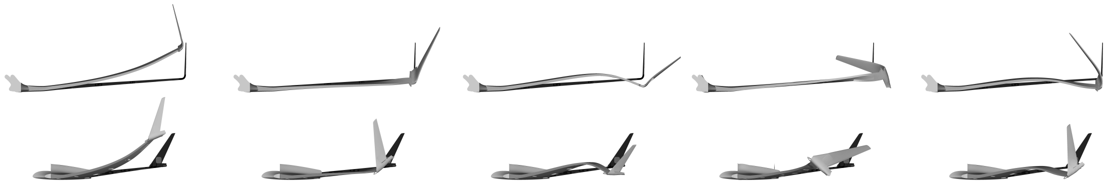

**(a)** Mode 1 **(b)** Mode 2 **(c)** Mode 3 **(d)** Mode 4 **(e)** Mode 5

**Figure 3.2:** Elastic mode shapes of the wing GFEM shown in different views.

Mode 1 corresponds to the first out-of-plane bending, dominated by vertical bending deformation. Mode 2 represents a pure torsional motion about the elastic axis. Mode 3 exhibits a second out-of-plane bending pattern with one node, which is confirmed by the partial correlation of entry (1,3) in the autoMAC matrix. Mode 4 presents a combination of in-plane bending and torsion, confirmed by the bright off-diagonal entry (2,4) and the visual coupling in the mode animation (longitudinal bending coupled with torsion). Finally, mode 5 is identified as the second torsional mode, featuring two nodal lines along the span. Entry (2,5) confirms the strong correlation with the first torsional mode.

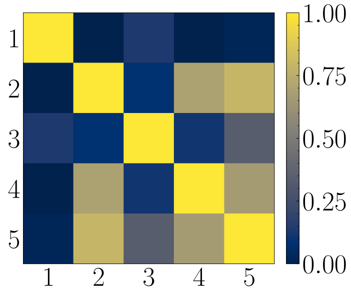

**Figure 3.3:** AutoMAC matrix of the wing GFEM.

### 3.1.2 Full GFEM of the BWB

#### Aeroelastic Analysis

The previous results on static deformation and modal response of the wing GFEM serve as the reference for static and modal optimization of the stick model. In the remainder of this section, the aeroelastic behaviour of the very flexible BWB is analysed. First, the modal characteristics of the full model in free-free condition are presented. Then, the evolution of damping and frequency with airspeed is examined with $V$–$g$ and $V$–$f$ plots, complemented by the root locus representation. Finally, the aeroelastic modes at flutter condition are identified. The complex eigenvalues and mode shapes at flutter are the reference results used for the aeroelastic optimization of the stick model.

Table 3.2 summarizes the modal characteristics, while Figure 3.4 depicts the corresponding mode shapes in two views. The modal identification of the full model is performed based on the visual mode shape animation and the autoMAC matrix (Figure 3.5).

**Table 3.2:** Modal behaviour of full GFEM in free-free condition.

| Mode | Label | $f$ (Hz) | Description |
|---|---|---|---|
| 7 | WB1 (S) | 5.01 | First wing bending (symmetric) |
| 8 | WB1 (A) | 7.03 | First wing bending (antisymmetric) |
| 9 | WT1 (S) | 7.49 | First wing torsion (symmetric) |
| 10 | WT1 (A) | 7.92 | First wing torsion (antisymmetric) |
| 11 | WB2 (S) | 11.22 | Second wing bending (symmetric) |
| 12 | WB2 (A) | 13.43 | Second wing bending (antisymmetric) |
| 13 | – | 13.70 | Higher order wing bending (symmetric) |
| 14 | – | 14.54 | Higher order wing bending (antisymmetric) |

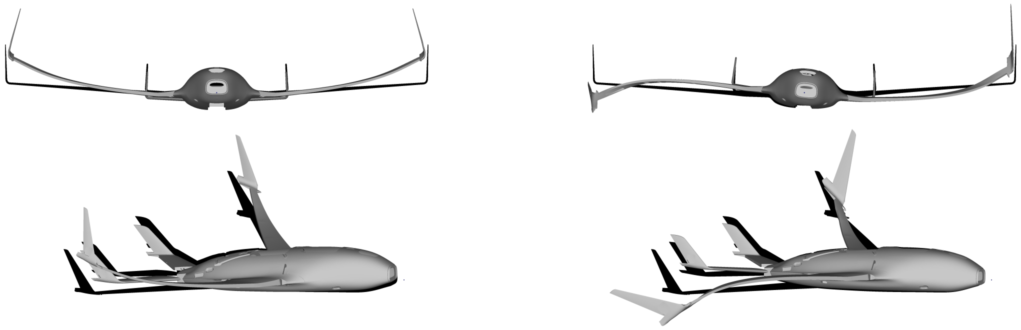

**(a)** Mode 7 **(b)** Mode 8

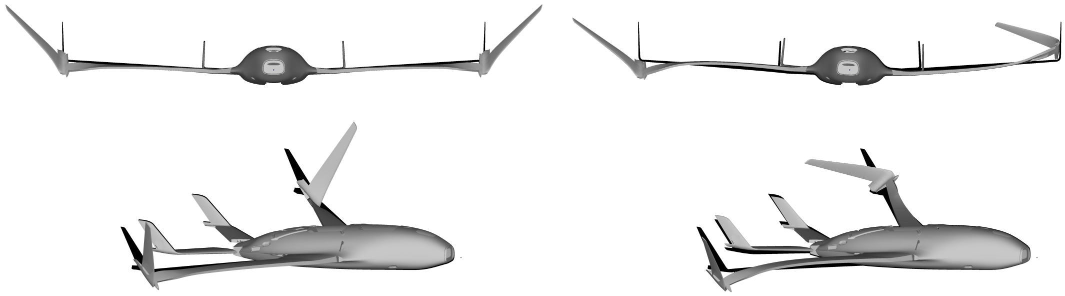

**(c)** Mode 9 **(d)** Mode 10

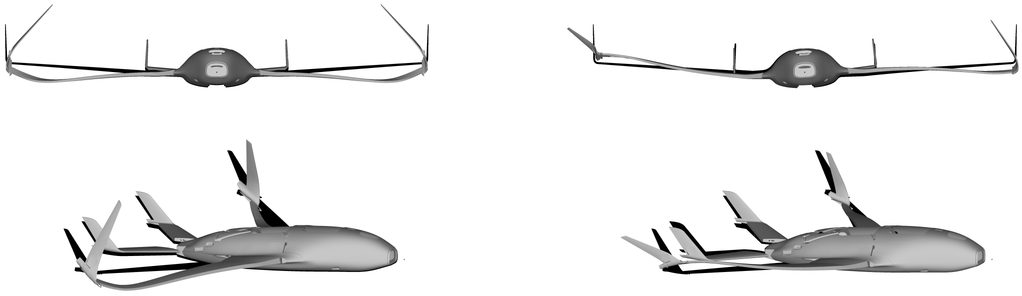

**(e)** Mode 11 **(f)** Mode 12

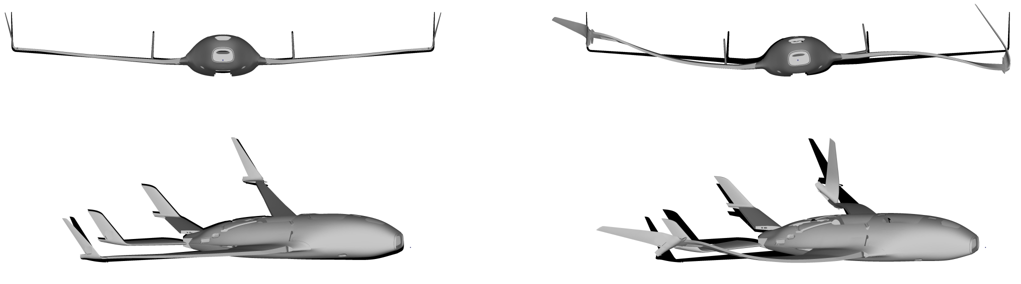

**(g)** Mode 13 **(h)** Mode 14

**Figure 3.4:** Elastic mode shapes of the very flexible BWB shown in different views.

Mode 7 corresponds to the symmetric first out-of-plane bending of the wing. Mode 8 is identified as an antisymmetric first out-of-plane bending of the wing coupled with some torsional component. Mode 9 and 10 are the first torsion of the wing in a symmetric and antisymmetric configuration, respectively. Mode 11 exhibits a second out-of-plane wing bending in a symmetric configuration. The bending component is evident from the visual animation, while some torsional contribution is confirmed by the bright entry (9, 11). Mode 12 shows an antisymmetric second out-of-plane bending of the wing coupled with some torsional component, as indicated by the partial correlation in entry (10, 12). Mode 13 and 14 appear to be higher-order wing bending in a symmetric and antisymmetric configuration, respectively. Mode 14 is coupled with modes 10 and 12 as suggested by the strong correlations observed in the autoMAC entries (10, 14) and (12, 14).

The upper-left quadrant of the autoMAC matrix, shown in Figure 3.5, represents the first 6 rigid body modes. The lower-right quadrant of the autoMAC matrix is used to identify coupling between elastic modes, whereas the upper-right quadrant (symmetric to the lower-left quadrant) is useful to assess whether elastic modes exhibit components of rigid-body motion.

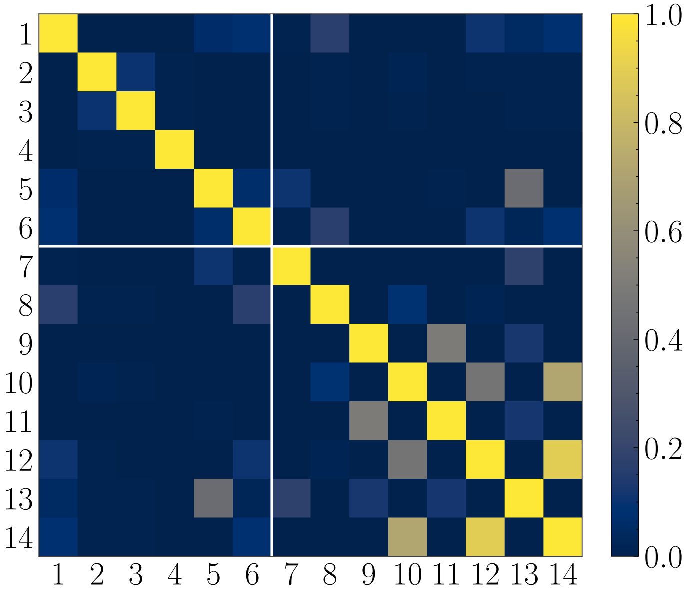

**Figure 3.5:** AutoMAC matrix of the full model.

These results serve as the modal basis for the subsequent aeroelastic analysis. The aeroelastic behaviour of the full GFEM is evaluated using the PKNL method, considering steady level flight at an altitude of 500 m. The resulting $V$–$g$ and $V$–$f$ diagrams, together with the root locus representation, are shown in Figure 3.8. The stability of the system is assessed from the evolution of modal damping and frequency with airspeed. Flutter is identified at the zero-crossing of the damping curves, which corresponds to the point at which the real part of the aeroelastic eigenvalue becomes positive. This condition is highlighted in the plots using a red star marker.

Two flutter points are detected in the $V$–$g$ plot, occurring at airspeeds of 64.26m/s and 73.80m/s. To properly identify the unstable aeroelastic modes and their underlying coupling mechanisms, visual mode shape animation and autoMACX matrices are examined. In contrast to the previously presented autoMAC matrices, the diagonal entries are not necessarily equal to 1 in the aeroelastic case. This is because the complex aeroelastic eigenvectors are generally not monophase. Nevertheless, higher autoMACX values (brighter entries) still indicate stronger modal compatibility.

**Table 3.3:** Aeroelastic instabilities within the flight envelope.

| **M** | **Label** | ***f* (Hz)** | ***V* (m/s)** | **Description** | **Flutter mechanism** |
|---|---|---|---|---|---|
| 9 | WBT$^*$(S) | 6.77 | 64.26 | Wing bending-torsion (symmetric) | BTF (S) |
| 8 | WBT$^*$(A) | 6.87 | 73.80 | Wing bending-torsion (antisymmetric) | BTF (A) |

In this aeroelastic analysis, the rigid body modes are retained; however, the plunge mode is found to be consistently unstable. Although this mode exhibits positive real part across all investigated flight points, it remains at near-zero frequency and does not couple with the aeroelastic modes of interest.

The first flutter point, at 64.26 m/s, occurs when the aeroelastic mode 9 becomes unstable and is labeled WBT$^*$ (S). The symmetric aeroelastic mode shape, illustrated in Figure 3.6, exhibits a coupled deformation involving wing torsion, consistent with the modal shape of mode 9, together with wing out-of-plane bending, which is characteristic of mode 7 identified in the modal analysis. The autoMACX matrix evaluated at this flutter speed, shown in Figure 3.9(a), reveals a strong modal correlation between modes 9 and 7, a coupling that was not present in the autoMAC matrix (Figure 3.5). The $V$–$f$ plot shows coalescence of the aeroelastic modes 7 and 9 once flight speed reaches 50 m/s. This behaviour indicates that the instability arises from aeroelastic coupling between bending and torsion modes, and is therefore classified as a classical bending-torsion flutter (BTF).

The second flutter point, occurring at 73.80 m/s, is associated with the instability of aeroelastic mode 8, labeled WBT$^*$ (A). The antisymmetric aeroelastic mode shape, illustrated in Figure 3.7, reveals a coupled deformation involving wing bending, consistent with the modal shape of mode 8, and wing torsion, which is characteristic of mode 10 identified in the modal analysis. The autoMACX matrix evaluated at this flutter speed, shown in Figure 3.9(b), exhibits a strong modal correlation between modes 8 and 10, a coupling that was significantly weaker in the autoMAC matrix (Figure 3.5). This behaviour indicates that the instability arises from aeroelastic coupling between bending and torsion modes, and is therefore classified as a antisymmetric bending-torsion flutter (BTF).

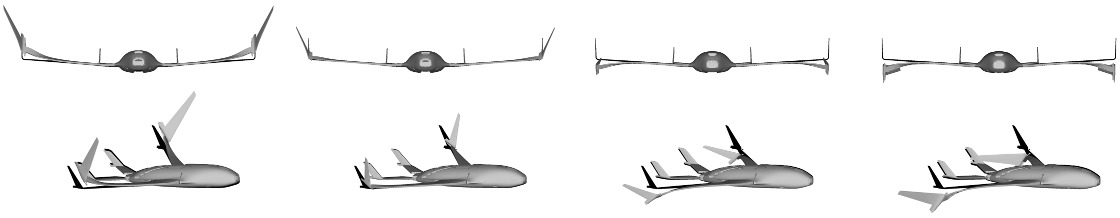

**(a)** $\phi = 0°$ **(b)** $\phi = 60°$ **(c)** $\phi = 120°$ **(d)** $\phi = 180°$

**Figure 3.6:** Mode shape of symmetric BTF at $V = 64.26$ m/s and flight altitude $h = 500$m, for different phase angles $\phi$.

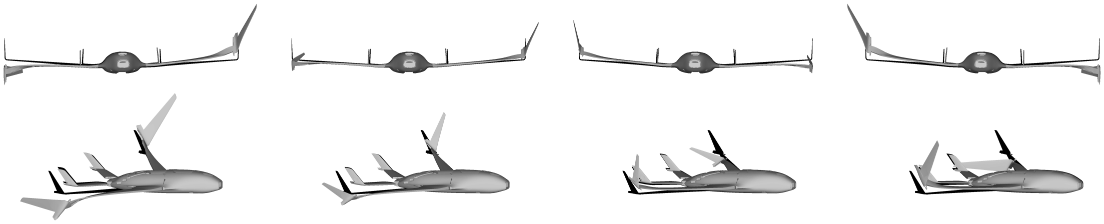

**(a)** $\phi = 0°$ **(b)** $\phi = 60°$ **(c)** $\phi = 120°$ **(d)** $\phi = 180°$

**Figure 3.7:** Mode shape of antisymmetric BTF at $V = 73.80$ m/s and flight altitude $h = 500\,$m, for different phase angles $\phi$.

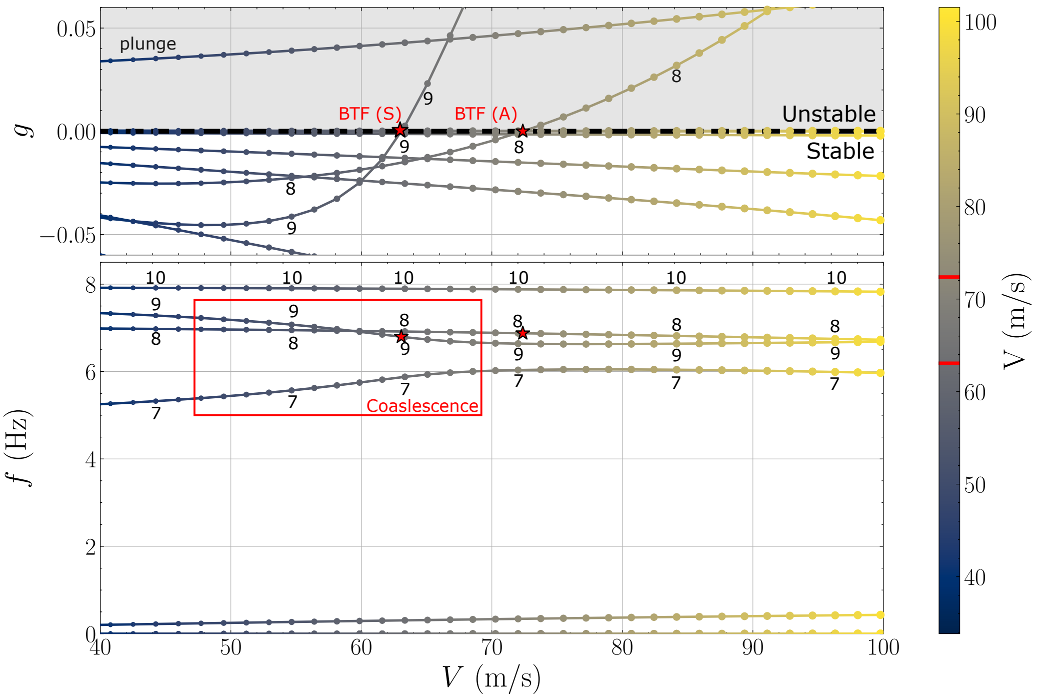

**(a)** $V$–$g$ (upper) and $V$–$f$ (lower) plots.

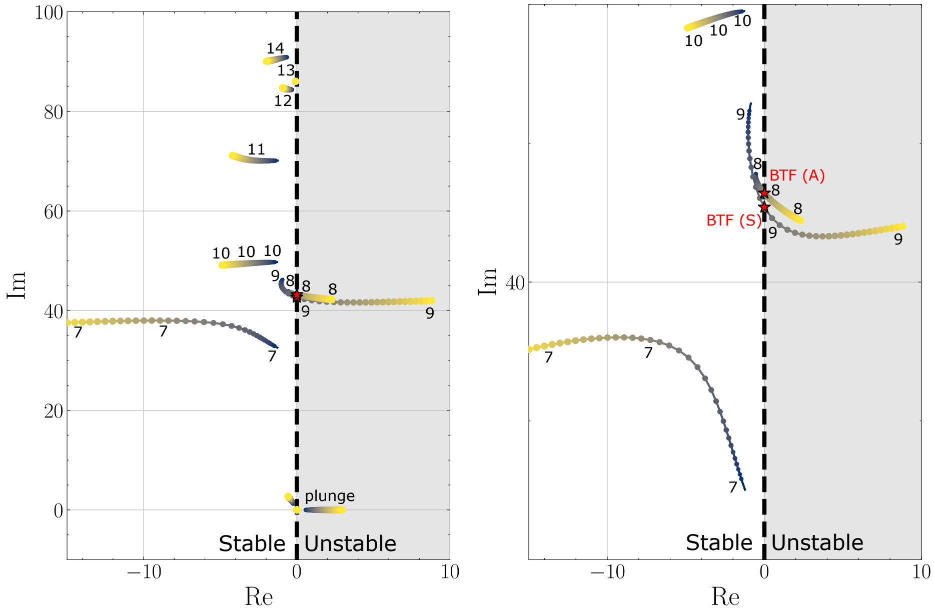

**(b)** Root locus of the open loop aeroelastic system.

**(c)** Close-up on the aeroelastic modes involved in the flutter mechanisms.

**Figure 3.8:** Stability plots of the full model at $h = 500\,\text{m}$, with increasing speed.

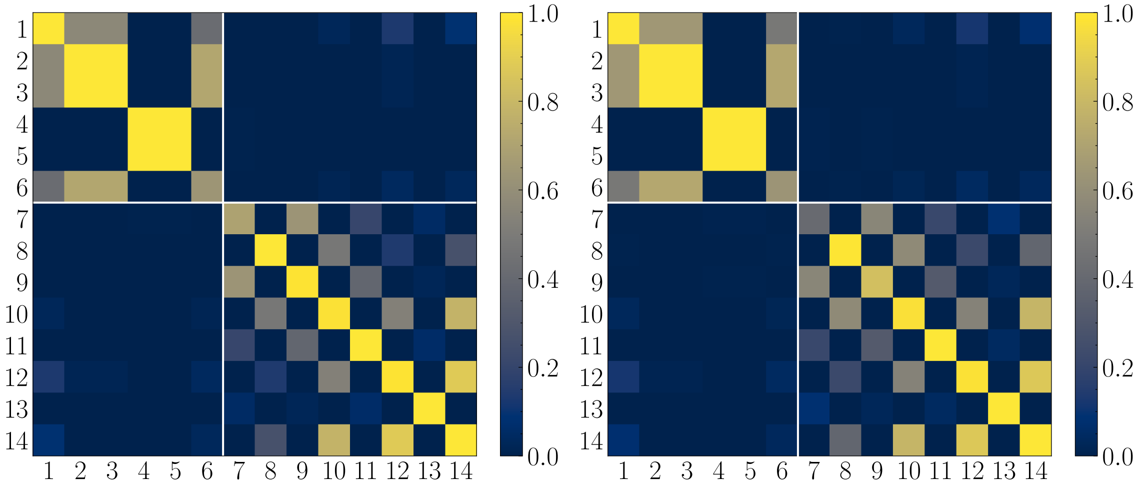

**(a)** $V = 64.26$ m/s **(b)** $V = 73.80$ m/s

**Figure 3.9:** AutoMACX matrices of the full aeroelastic model at both flutter points, at a flight altitude of $h = 500\,\mathrm{m}$.

## 3.2 Optimized Stick Model Results

This section presents the results obtained from the proposed methodology for optimizing the SM. Three strategies are investigated. First, the SM is optimized to match the static deformation of the wing. Second, the optimization reproduces the elastic modal response of the wing. Finally, the SM is optimized to replicate the aeroelastic behaviour of the full GFEM. The results are compared against the solutions in Section 3.1 to assess the accuracy and robustness of the proposed approach.

### 3.2.1 Case Study A: Static Optimization Results

This section presents the results of static optimization of the stick model, focusing on the simultaneous minimization of the vertical displacement error ($E_y$) and the twist error ($E_\theta$) with respect to the reference wing GFEM solution.

To investigate the trade-off between these two objectives, a Pareto front analysis is implemented. The objective function is presented in Equation 2.8 and the weight coefficients satisfy

$$w_y + w_\theta = 1, \tag{3.1}$$

where $w_y$ and $w_\theta$ are the weight coefficients for the vertical displacement error and the twist error, respectively. A systematic sweep of the weight space is done using increments of 0.05, resulting in 21 distinct optimization subcases.

In the context of multi-objective optimization, a Pareto front represents the set of non-dominated solutions, for which no objective can be improved without degrading the other. Conversely, solutions that are inferior in both objectives to at least one other design are classified as dominated and are therefore discarded. The Pareto front provides a physically meaningful representation of the best trade-offs between competing error metrics.

Out of the 21 weight combinations considered, 7 designs are identified as non-dominated and thus form the Pareto front, while the remaining subcases correspond to dominated solutions. The resulting Pareto front is presented in Figure 3.10

Although 7 configurations lie on the Pareto front, only a representative subset of five Pareto design points is presented in Table 3.4. These configurations are selected to illustrate the range of trade-offs captured by the Pareto front and include: (1) the design achieving the minimum vertical displacement error, (2-4) three balanced configurations exhibiting simultaneously low errors in both objectives, and (5) the design achieving the minimum twist error. To identify a suitable SM for subsequent analyses, an additional filtering criterion was defined: candidate designs are required to exhibit errors below 15% in vertical displacement and below 15% in twist. Among the Pareto candidate design points, three configurations satisfy both criteria, but only one is selected as the optimal design for static optimization. This configuration is highlighted in bold in Table 3.4.

A comparison between the static deformation of the optimal SM and the reference wing GFEM is presented in Figure 3.11 using different colormaps, while the undeformed configuration is shown in black. The optimized SM showed a strong agreement in both vertical displacement ($E_y = 6.93\%$) and twist ($E_\theta = 3.01\%$) along the span with the GFEM counterpart. Overall, the close correspondence in both bending and torsional responses indicates that the optimized stick model provides an accurate reduced-order representation of the wing static behaviour under the considered loading condition.

**Table 3.4:** Summary of the static optimization for different weights. Optimal point is highlighted in bold and baseline results are shown for reference.

| **Parameter** | | **Optimized stick** | | | | | **Baseline** |
|---|---|---|---|---|---|---|---|
| **Weight coefficients** | $w_y$ | 0.90 | 0.55 | **0.40** | 0.35 | 0.05 | - |
| | $w_\theta$ | 0.10 | 0.45 | **0.60** | 0.65 | 0.95 | - |
| **Station 1** (GRID 106) | $\Delta y$ | -1.41% | -12.01% | **-14.04%** | -10.95% | 26.67% | 0.018 m |
| | $\Delta\theta$ | -49.51% | -29.88% | **-0.56%** | -31.05% | -5.42% | −0.012 rad |
| **Station 2** (GRID 113) | $\Delta y$ | 1.71% | 2.62% | **5.39%** | 1.56% | -18.67% | 0.062 m |
| | $\Delta\theta$ | -60.88% | -3.45% | **0.72%** | 2.42% | 0.68% | −0.021 rad |
| **Station 3** (GRID 119) | $\Delta y$ | 0.17% | 3.92% | **-5.53%** | 0.78% | -42.21% | 0.151 m |
| | $\Delta\theta$ | 8.46% | -0.48% | **-1.09%** | -1.02% | 0.12% | −0.030 rad |
| **Error metrics** | $E_y$ | 1.18% | 6.01% | **6.92%** | 6.12% | 34.35% | - |
| | $E_\theta$ | 74.78% | 9.50% | **3.01%** | 8.79% | 2.78% | - |

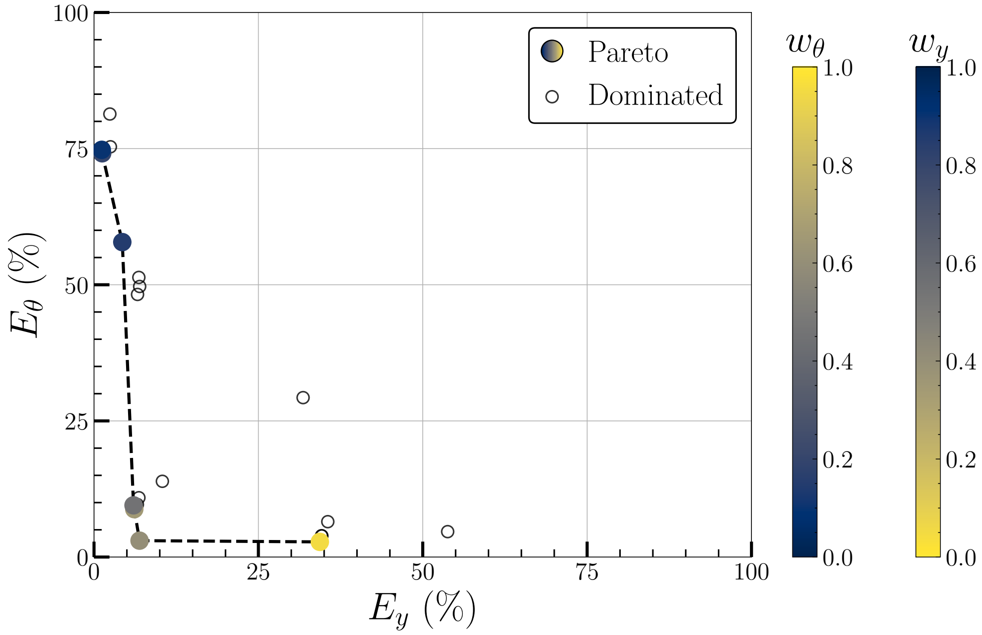

**Figure 3.10:** Pareto front for static optimization, considering 21 design points.

### 3.2.2 Case Study B: Modal Optimization

This section presents the results of the modal optimization of the stick model, focusing on the simultaneous minimization of three modal error metrics with respect to the reference wing GFEM: the natural frequency error ($E_f$), crossMAC trace error ($E_c$) and the autoMAC error ($E_a$).

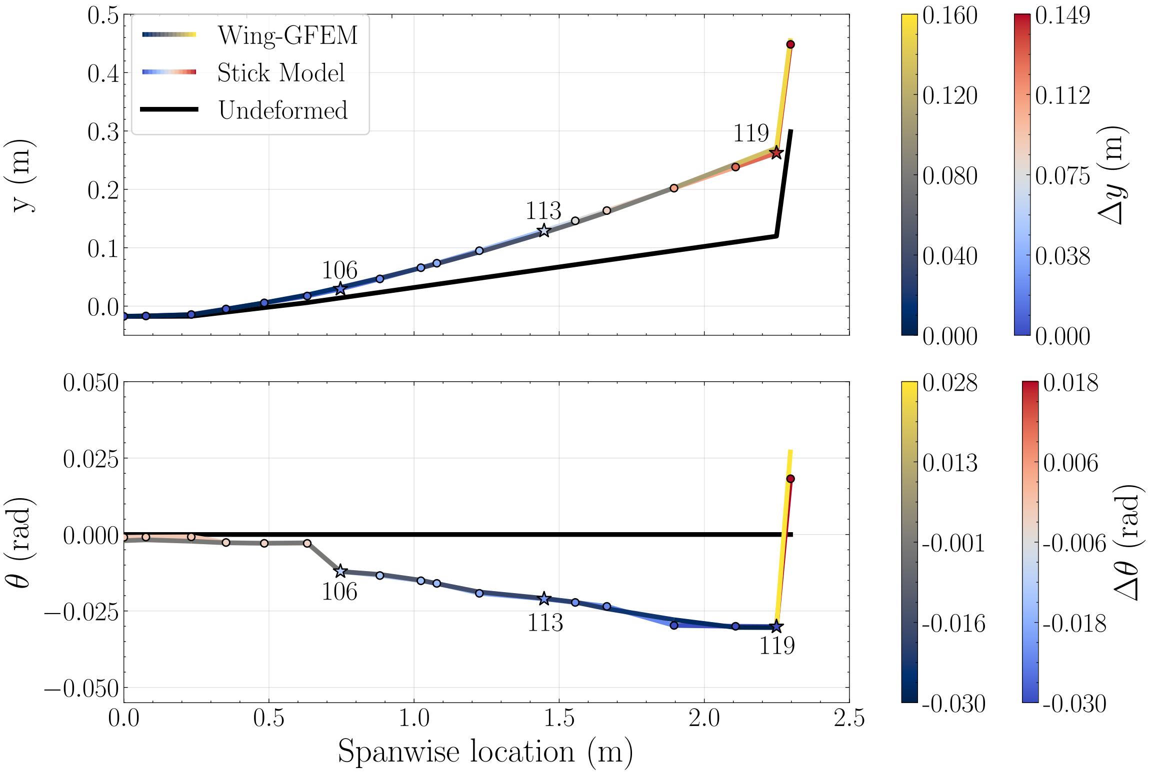

**Figure 3.11:** Comparison of vertical displacement and twist between the reference wing GFEM and the stick model. The SM is discretized in beam elements and the dots represent the GRID points.

To investigate the trade-off between these three objectives, a Pareto front analysis is implemented. The objective function is presented in Equation 2.9 and the weight coefficients satisfy

$$w_f + w_c + w_a = 1, \tag{3.2}$$

where $w_f$, $w_c$ and $w_a$ are the weight coefficients for the natural frequency error, crossMAC trace error and the autoMAC error, respectively. A systematic sweep of the weight space is done using increments of 0.05, resulting in 231 distinct optimization subcases.

In this case, three objectives are considered simultaneously, and the resulting Pareto front forms a two-dimensional surface in a three-dimensional objective space. Each optimized configuration corresponds to a point in the space $(E_f, E_c, E_a)$, and the collection of non-dominated points approximates the Pareto surface. The Pareto front provides a physically meaningful representation of the best achievable trade-offs between competing modal error metrics.

Out of the 231 weight combinations considered, 27 designs are identified as non-dominated and thus form the Pareto front, while the remaining subcases correspond to dominated solutions. The resulting Pareto surface is presented in Figure 3.12.

Although 27 configurations lie on the Pareto front, only a representative subset of five Pareto design points is presented in Table 3.4. These configurations are selected to illustrate the range of trade-offs captured by the Pareto front and include: (1) the design achieving the minimum natural frequency error, (2) the design achieving the minimum crossMAC trace error, (3) the design achieving the minimum autoMAC error, (4-5) two balanced configurations exhibiting simultaneously low errors across all three objectives.

To identify a suitable SM for subsequent analyses, an additional filtering criterion was defined: candidate designs are required to exhibit error below 15% in natural frequency, error below 25% in crossMAC trace, and error below 25% in autoMAC. Among the Pareto candidate design points, two configurations satisfy all criteria; however, only one is selected as the optimal design for modal optimization. This configuration is highlighted in bold in Table 3.5.

The comparison between the reference wing GFEM and the optimized stick model shows a good agreement in both natural frequencies and mode shapes. The optimized SM accurately captures the first five resonance modes with a frequency error of 5.41%, a crossMAC trace error of 16.9% and autoMAC error of 20.19%.

The error metric $E_x$ introduced in Section 2.2.5 is applied to assess the quality of modal optimization in reproducing the reference mode shapes. This metric is defined by comparing the autoMAC matrix of the wing GFEM and the crossMAC matrix obtained after mode tracking of the SM. While the autoMAC matrix characterizes the modal compatibility of the reference model, the crossMAC quantifies the correlation between the eigenvectors, or mode shapes, of the SM and those of the wing GFEM. Close agreement between the two matrices indicates a high degree of modal similarity across models. Figure 3.13 provides a visual representation of $E_x$, expressed as a percentage error between the wing GFEM autoMAC matrix and the crossMAC matrix after mode tracking. A vast area of low error (dark blue) is observed, indicating that the majority of the SM mode shapes closely match those of the reference model, with errors below 10%. In particular, mode 1 (OB1) and mode 2 (T1) are very accurately captured. Mode 3 (OB2), mode 4 (IB-T) and mode 5 (T2) exhibit slightly larger discrepancies, although the associated error remains below 25%, indicating a satisfactory representation of higher-order and coupled modes.

Overall, this level of agreement in both natural frequency and mode shapes indicates that the optimized stick model provides a reliable reduced-order representation of the cantilevered wing's modal behaviour.

**Table 3.5:** Summary of the modal optimization for different weights. Optimal point is highlighted in bold and baseline results are shown for reference.

| **Parameter** | | **Optimized stick** | | | | | **Baseline** |
|---|---|---|---|---|---|---|---|
| **Weight coefficients** | $w_f$ | 0.85 | 0.05 | 0.00 | 0.45 | **0.55** | - |
| | $w_c$ | 0.10 | 0.70 | 0.10 | 0.20 | **0.40** | - |
| | $w_a$ | 0.05 | 0.25 | 0.90 | 0.35 | **0.05** | - |
| **Natural frequency** | 1 | -0.12% | -15.41% | 23.28% | -0.79% | **-3.88%** | 5.45 Hz |
| | 2 | -3.11% | 23.42% | 62.65% | -5.88% | **-2.21%** | 13.93 Hz |
| | 3 | 4.24% | 188% | 374% | 3.44% | **0.22%** | 16.44 Hz |
| | 4 | -4.25% | 28.55% | 23.91% | 6.73% | **9.02%** | 26.88 Hz |
| | 5 | 5.52% | -23.63% | 32.67% | -4.29% | **-6.71%** | 27.98 Hz |
| **Error metrics** | $E_f$ | 3.90% | 86.63% | 171% | 4.68% | **5.41%** | - |
| | $E_c$ | 33.15% | 14.18% | 26.89% | 22.36% | **16.90%** | - |
| | $E_a$ | 31.85% | 7.56% | 6.19% | 23.30% | **20.19%** | - |

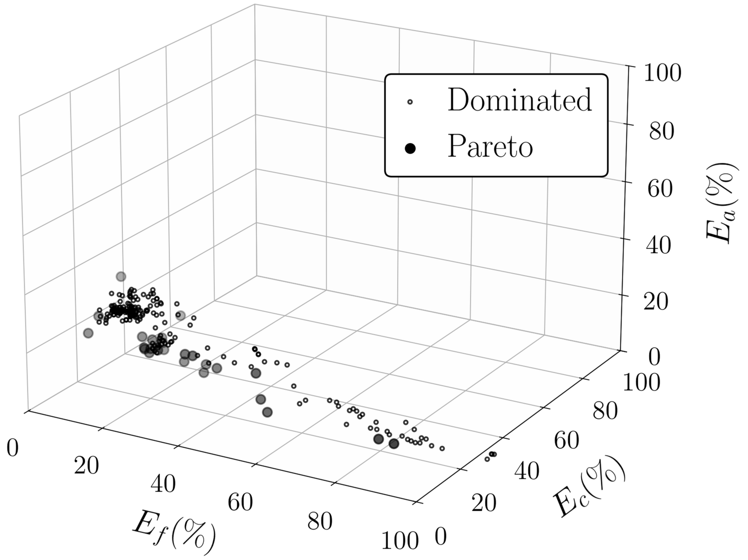

**Figure 3.12:** Pareto front for modal optimization, considering 231 design points.

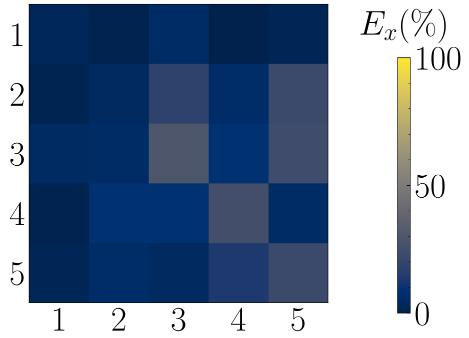

**Figure 3.13:** Comparison of the mode shapes of the wing GFEM and SM, showing an RMS error of $E_x = 12.78\%$.

### 3.2.3 Case Study C: Aeroelastic Optimization

This section presents the results of aeroelastic optimization of the stick model. A hybrid representation is adopted, as described in Section 2.2.1, to replicate the aeroelastic behaviour of the full GFEM, focusing on the simultaneous minimization of the complex eigenvalue error ($E_e$) and the complex eigenvector error ($E_x$) with respect to the reference GFEM solution.

To investigate the trade-off between these two objectives, a Pareto front analysis is implemented. The objective function is presented in Equation 2.10 and the weight coefficients satisfy

$$w_e + w_x = 1, \tag{3.3}$$

where $w_e$ and $w_x$ are the weight coefficients for the complex eigenvalue error and the complex eigenvector error, respectively. A systematic sweep of the weight space is done using increments of 0.05, resulting in 21 distinct optimization subcases.

Out of the 21 weight combinations considered, 6 designs are identified as non-dominated and thus form the Pareto front, while the remaining subcases correspond to dominated solutions. The resulting Pareto front is presented in Figure 3.14.

Although 6 configurations lie on the Pareto front, only a representative subset of five Pareto design points is presented in Table 3.6. These configurations are selected to illustrate the range of trade-offs captured by the Pareto front and include: (1) the design achieving the minimum complex eigenvalue error, (2-4) three balanced configurations exhibiting simultaneously low errors in both objectives, and (5) the design achieving the minimum complex eigenvector error. To identify a suitable SM for subsequent analyses, an additional filtering criterion was defined: candidate designs are required to exhibit errors below 5% in complex eigenvalues and below 25% in complex eigenvectors. Among the Pareto candidate design points, 4 configurations satisfy both criteria, but only one is selected as the optimal design for aeroelastic optimization. This configuration is highlighted in bold in Table 3.6.

The comparison between the reference GFEM and the optimized stick model shows a good agreement in both complex eigenvalues across the flight envelope and aeroelastic mode shape at the speed of the first flutter point, with errors of 3.70% and 21.71%, respectively.

Figure 3.16 compares the aeroelastic behaviour of the full GFEM and hybrid model, at an altitude of 500 m, through the use of $V$–$g$, $V$–$f$ diagrams and the root locus representation. Each model uses a different colormap. Overall, the hybrid model reproduces the key aeroelastic trends observed in the reference GFEM, including the evolution of modal damping and frequency with airspeed and the identification of the critical flutter mechanisms.

The SM predicts both symmetric and antisymmetric bending-torsion flutter mechanism with errors below 3% in speed and below 8% in frequency. The SM closely follows baseline GFEM trends, particularly in capturing the coalescence of aeroelastic modes in the $V$–$f$ plot. The first flutter point (BTF (S)) is characterized by a coupled deformation involving wing out-of-plane bending and torsion, arising from the interaction between aeroelastic modes 9 and 7. The second flutter point (BTF (A)) corresponds to an antisymetric coupling between wing bending and torsion, driven by the interaction between aeroelastic modes 8 and 10. In both cases, the hybrid model successfully reproduces the physical nature of the flutter mechanisms identified in the reference solution.

Figure 3.15 further compares the aeroelastic mode shapes of the SM and the GFEM at the first flutter point using the eigenvector error metric ($E_x$). A vast area of low error is observed for the aeroelastic modes 7-10, which are directly involved in the flutter mechanisms, with relative errors below 12%. Higher-order aeroelastic modes (modes 11-13) are reproduced with lower fidelity, exhibiting relative errors above 25%; however, these modes remain dynamically uncoupled from the critical flutter modes and therefore have a limited influence on flutter prediction.

Overall, the results demonstrate that the optimized stick model retains sufficient fidelity in both eigenvalue evolution and mode shape representation to accurately predict the flutter mechanisms of the full GFEM. Table 3.7 summarizes the computational cost of the stick model, GFEM model and optimization framework.

**Table 3.6:** Summary of the aeroelastic optimization of the hybrid model for different weights. Optimal point is highlighted in bold and baseline results are shown for reference.

| **Parameter** | | **Optimized stick** | | | | | **Baseline** |
|---|---|---|---|---|---|---|---|
| **Weight coefficients** | $w_e$ | 0.70 | 0.75 | **0.80** | 0.95 | 1.00 | - |
| | $w_x$ | 0.30 | 0.25 | **0.20** | 0.05 | 0.00 | - |
| **BTF (S)**$_{h\,=\,500\,\mathrm{m}}$ | $V$ | -5.29% | -2.07% | **-2.81%** | -3.43% | -1.98% | 64.26 m/s |
| | $f$ | 0.59% | -4.07% | **-3.03%** | -2.82% | -3.94% | 6.77 Hz |
| **BTF (A)**$_{h\,=\,500\,\mathrm{m}}$ | $V$ | -6.98% | -0.86% | **-2.59%** | -2.79% | 1.56% | 73.80 m/s |
| | $f$ | -2.08% | -7.88% | **-7.95%** | -6.85% | -7.06% | 6.87 Hz |
| **Error metrics** | $E_e$ | 4.91% | 3.76% | **3.27%** | 2.94% | 2.69% | - |
| | $E_x$ | 18.15% | 21.10% | **21.71%** | 22.03% | 22.77% | - |

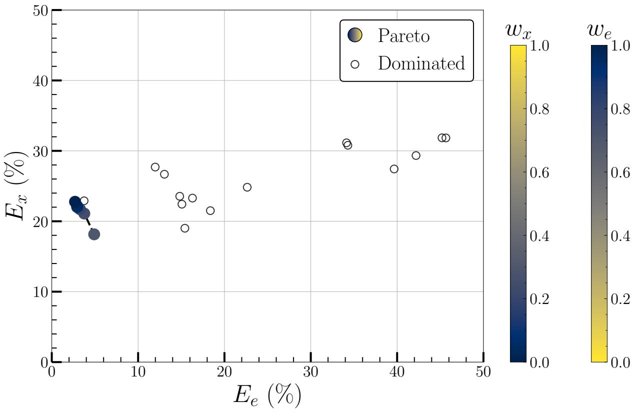

**Figure 3.14:** Pareto front for aeroelastic optimization, considering 21 design points.

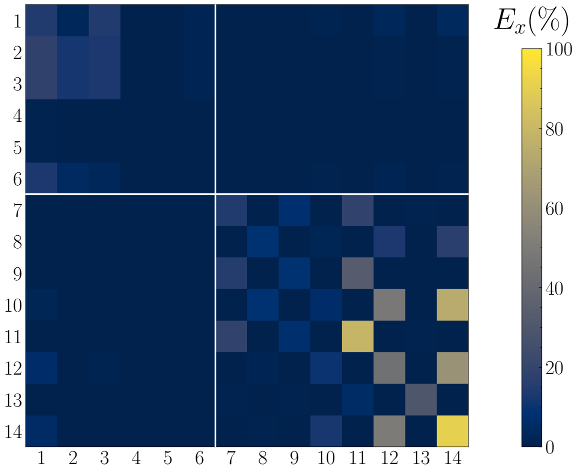

**Figure 3.15:** Comparison of the aeroelastic mode shapes of the reference GFEM and hybrid model at the first flutter point ($V$ = 64.26 m/s) at a flight altitude $h = 500\,\mathrm{m}$, showing an RMS error of $E_x = 21.71\%$.

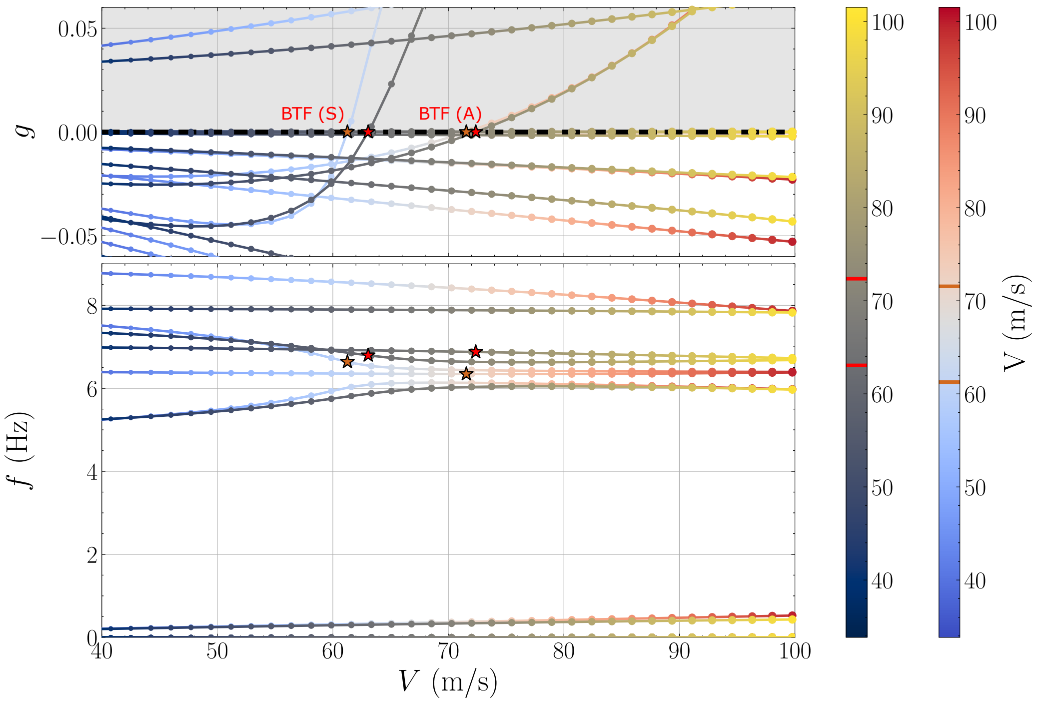

**(a)** $V$–$g$ (upper) and $V$–$f$ (lower) plots.

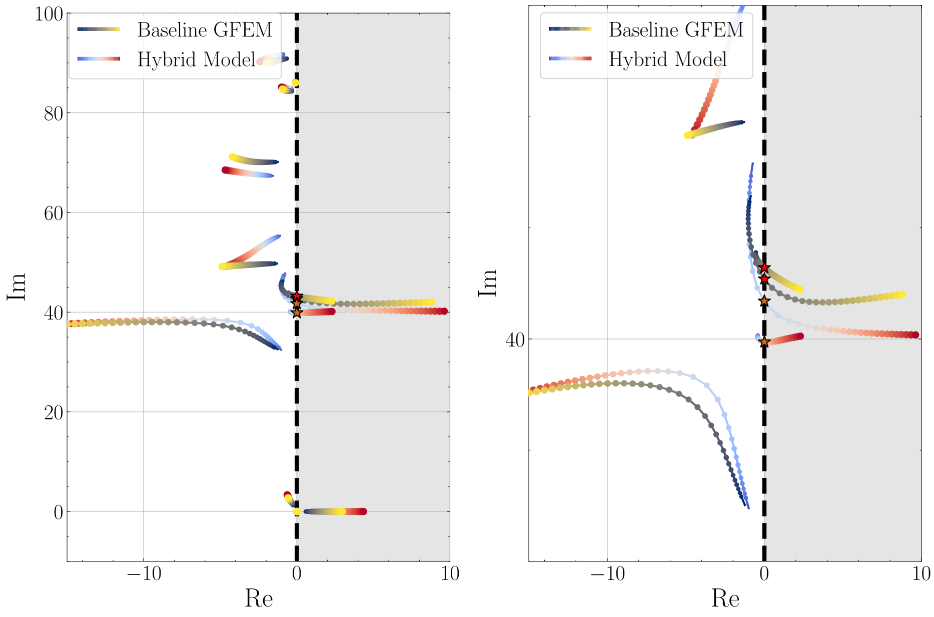

**(b)** Root locus of the open loop aeroelastic system.

**(c)** Close-up on the aeroelastic modes involved in the flutter mechanisms.

**Figure 3.16:** Stability plots of the full model and hybrid model at $h = 500\,\mathrm{m}$, with increasing speed.

**Table 3.7:** Summary of the computational cost of the stick model, GFEM model and optimization framework.

| | | Computational cost | | |
|---|---|---|---|---|
| | | **Static** | **Modal** | **Aeroelastic** |
| **Model runtime** | **Wing GFEM** | 3.51s | 2.87s | – |
| | **Wing SM** | 0.93s | 0.77s | – |
| | **Full GFEM** | 28.26s | 17.15s | 71.71s |
| | **Hybrid Model** | 22.26s | 12.06s | 37.59s |
| **Optimization** | **Subcases** | 21 | 231 | 21 |
| | **CPUs used** | 24 | 24 | 16 |
| | **Runtime/CPU** | 17h 55m 19s | 12d 20h 51m 40s | 15d 17h 9m 8s |
| | **Design points evaluated** | $1.67 \times 10^6$ | $34.66 \times 10^6$ | $0.58 \times 10^6$ |

### 3.2.4 Validation: Hybrid Model

The stick model is optimized to replace the very flexible wings of the full GFEM in a hybrid representation, as described in Section 2.2.1. In this configuration, the SM is coupled with the remaining airframe components, such as rigid winglet and fuselage, which are retained in their GFEM form. For Case Study A and Case Study B, the static and modal responses of the SM are compared with the results of Section 3.1.1, providing an initial assessment of the accuracy of the reduced-order model.

Rather than re-optimizing the hybrid configuration, a representative set of candidate stick models is assembled from the Pareto front solutions obtained in the static and modal optimizations. These candidates are subsequently applied to the hybrid model, evaluated based on their aeroelastic performance and compared with the candidates obtained from the aeroelastic optimization.

To assess the accuracy and robustness of the hybrid representation, the model is tested at different analysis conditions. Static validation is performed under the negative ultimate load, modal characteristics are compared with those of the full GFEM, and the aeroelastic response is assessed at a different flight altitude ($h = 1000\,\mathrm{m}$) to evaluate the sensitivity of the optimized SM to operating conditions. Each candidate design is evaluated using the error metrics introduced in Sections 2.2.3-2.2.5. A summary of these results is provided in Table 3.8. As expected, the SM from static optimization outperforms the others in the static deformation error metrics, while the SM from modal optimization is the best in the modal error metrics. When evaluating the aeroelastic response of the stick models, the SM from modal optimization can predict the flutter points, speed, frequency and mode shape, with better accuracy than the SM from aeroelastic optimization. Therefore, the SM from modal optimization is selected as the optimal configuration and is highlighted in bold.

A comparison between the static deformation of the optimal hybrid model and the reference GFEM is presented in Figure 3.17 using different colormaps, while the undeformed configuration is shown in black. The optimized SM showed a good agreement in vertical displacement ($E_y = 12.25\%$) along the span with the GFEM counterpart. On the other hand, the SM under performs in twist, with an error of $E_y = 53.96\%$. But the twist values are small ($\Delta\theta < 1.5^\circ$), and therefore can be neglected. Overall, the optimized stick model provides an accurate reduced-order representation of the wing static behaviour under positive and negative ultimate loading conditions.

The comparison between the reference GFEM and the optimized hybrid model shows a good agreement in both natural frequencies and mode shapes. The optimized SM accurately captures the first eight resonance modes with a frequency error of 5.53%, a crossMAC trace error of 19.22% and autoMAC error of 14.27%.

The error metric $E_x$ introduced in Section 2.2.5 is applied to assess the quality of modal optimization in reproducing the reference mode shapes. Figure 3.18 provides a visual representation of $E_x$, expressed as a percentage error between the wing GFEM autoMAC matrix and the crossMAC matrix after mode tracking. Close agreement between the two matrices indicates a high degree of modal similarity across models. A vast area of low error (dark blue) is observed, indicating that the majority of the SM mode shapes closely match those of the reference model, with errors below 10%. In particular, mode 7-10 and 13 are very accurately captured. Mode 11, 12 and 14 exhibit larger discrepancies, with errors above 25%.

Figure 3.19 compares the aeroelastic behaviour of the full GFEM and hybrid model, at an altitude of $h = 1000\,\mathrm{m}$, through the use of $V$–$g$, $V$–$f$ diagrams. Each model uses a different colormap. Overall, the hybrid model reproduces the key aeroelastic trends observed in the reference GFEM, including the evolution of modal damping and frequency with increasing airspeed and the identification of the critical flutter mechanisms.

The SM predicts both symmetric and antisymmetric bending-torsion flutter mechanism with errors below 2% in speed and below 6% in frequency. The SM closely follows baseline GFEM trends, particularly in capturing the coalescence of aeroelastic

**Table 3.8:** Error metrics of the candidate stick models evaluated in the hybrid configuration under static, modal, and aeroelastic analyses. Optimal point is highlighted in bold and baseline results are shown for reference.

| **Model** | | **Optimized stick** | | | **Baseline** |
|---|---|---|---|---|---|
| **Weight coefficients** | $w_y$ | 0.40 | **0.00** | 0.00 | - |
| | $w_\theta$ | 0.60 | **0.00** | 0.00 | - |
| | $w_f$ | 0.00 | **0.55** | 0.00 | - |
| | $w_c$ | 0.00 | **0.40** | 0.00 | - |
| | $w_a$ | 0.00 | **0.05** | 0.00 | - |
| | $w_e$ | 0.00 | **0.00** | 0.80 | - |
| | $w_x$ | 0.00 | **0.00** | 0.20 | - |
| **Station 1** | $\Delta y$ | 11.60% | **-3.96%** | 13.16% | $-0.009\,\mathrm{m}$ |
| (GRID 106) | $\Delta\theta$ | -4.15% | **43.47%** | 62.67% | $0.006\,\mathrm{rad}$ |
| **Station 2** | $\Delta y$ | -5.8% | **-11.49%** | 1.86% | $-0.031\,\mathrm{m}$ |
| (GRID 113) | $\Delta\theta$ | -3.44% | **38.08%** | 71.88% | $0.010\,\mathrm{rad}$ |
| **Station 3** | $\Delta y$ | 4.84% | **-7.48%** | 6.87% | $-0.074\,\mathrm{m}$ |
| (GRID 119) | $\Delta\theta$ | -0.85% | **36.38%** | 54.83% | $0.015\,\mathrm{rad}$ |
| **Natural frequency** | 7 | 5.32% | **-4.18%** | -1.17% | 5.01 Hz |
| | 8 | 5.71% | **-5.32%** | -8.75% | 7.03 Hz |
| | 9 | 8.38% | **5.09%** | 4.39% | 7.49 Hz |
| | 10 | 74.19% | **8.69%** | 11.07% | 7.92 Hz |
| | 11 | 38.17% | **-7.40%** | -6.07% | 11.22 Hz |
| | 12 | 24.31% | **-5.31%** | 8.31% | 13.43 Hz |
| | 13 | -0.47% | **-0.07%** | 0.08% | 13.70 Hz |
| | 14 | -32.19% | **-4.06%** | -7.50% | 14.54 Hz |
| **BTF (S)**$_{h\,=\,1000\,\mathrm{m}}$ | $V$ | -24.33% | **-1.80%** | -2.76% | 64.55 m/s |
| | $f$ | 1.53% | **0.90%** | -3.05% | 6.79 Hz |
| **BTF (A)**$_{h\,=\,1000\,\mathrm{m}}$ | $V$ | -19.41% | **-0.03%** | -2.59% | 74.08 m/s |
| | $f$ | -2.95% | **-5.27%** | -7.95% | 6.87 Hz |
| **Error metrics** | $E_y$ | 6.12% | **12.25%** | 11.37% | - |
| | $E_\theta$ | 18.09% | **53.96%** | 73.45% | - |
| | $E_f$ | 33.01% | **5.53%** | 6.91% | - |
| | $E_c$ | 38.26% | **19.22%** | 33.05% | - |
| | $E_a$ | 21.00% | **14.27%** | 16.28% | - |
| | $E_e$ | 16.65% | **4.29%** | 3.31% | - |
| | $E_x$ | 23.13% | **15.67%** | 21.74% | - |

modes in the $V$–$f$ plot. The first flutter point (BTF (S)) is characterized by a coupled deformation involving wing out-of-plane bending and torsion, arising from the interaction between aeroelastic modes 9 and 7. The second flutter point (BTF (A)) corresponds to an antisymetric coupling between wing bending and torsion, driven by the interaction between aeroelastic modes 8 and 10. In both cases, the hybrid model successfully reproduces the physical nature of the flutter mechanisms identified in the reference solution.

Figure 3.22 further compares the aeroelastic mode shapes of the SM and the GFEM at the flutter points using the eigenvector error metric ($E_x$). A vast area of low error is observed for the aeroelastic modes 7-10, which are directly involved in the flutter mechanisms, with relative errors below 7%. Higher-order aeroelastic modes (modes 11-13) are reproduced with lower fidelity, exhibiting relative errors above 25%; however, these modes remain dynamically uncoupled from the critical flutter modes and therefore have a limited influence on flutter prediction.

Overall, the results demonstrate that the optimized stick model retains sufficient fidelity in static deformation, modal response and aeroelastic behaviour to accurately predict the flutter mechanisms of the full GFEM.

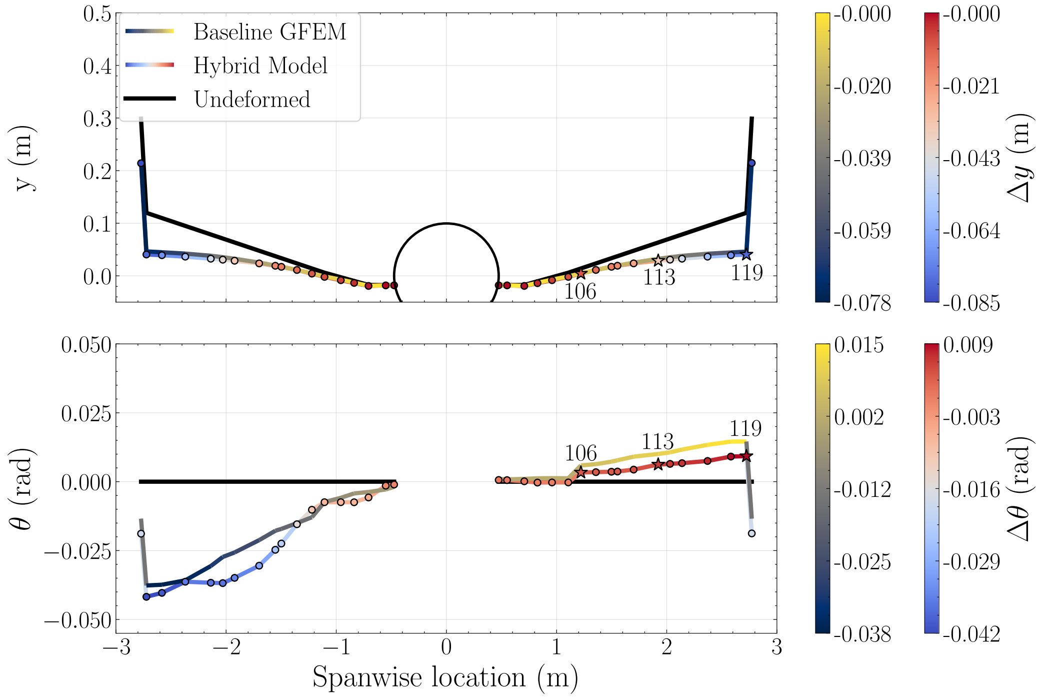

**Figure 3.17:** Comparison of vertical displacement and twist between the reference GFEM and the hybrid model. The SM is discretized and the dots represent the GRID.

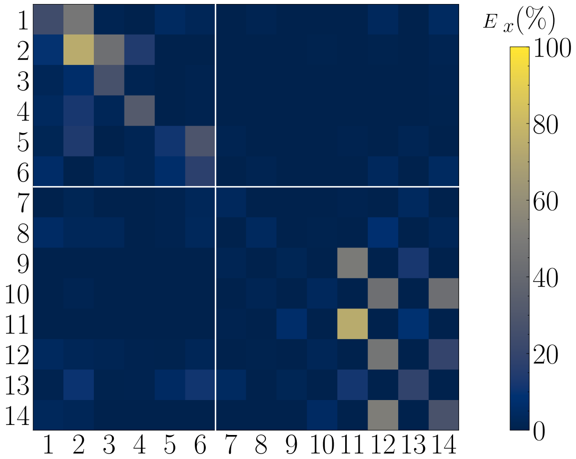

**Figure 3.18:** Comparison of the mode shapes of the reference GFEM and hybrid model, from modal analysis, showing an RMS error of $E_x = 13.00\%$.

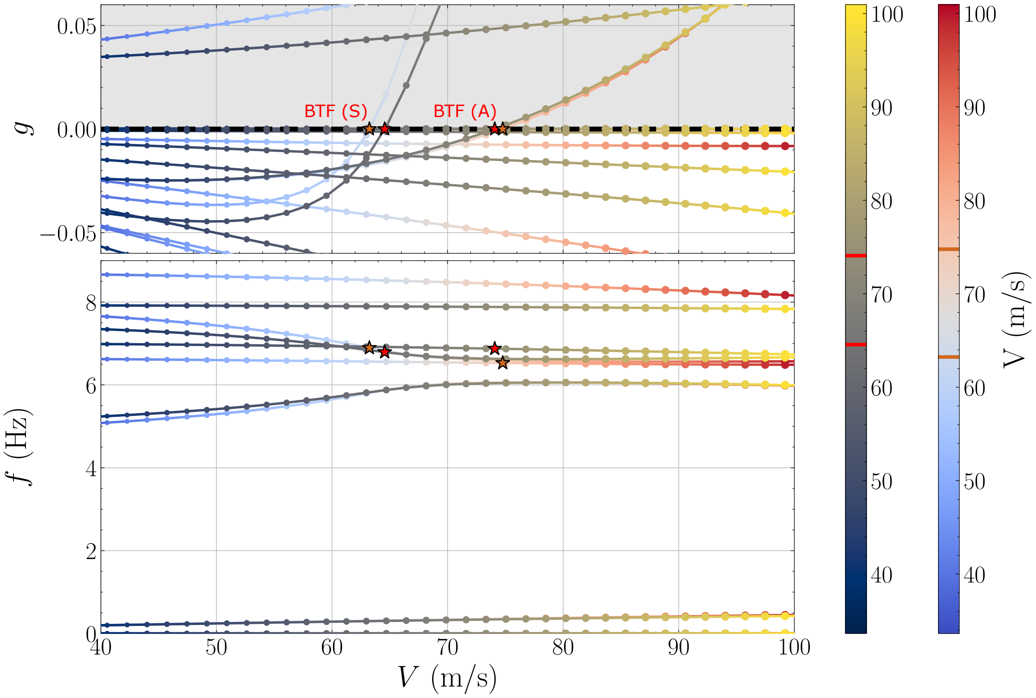

**Figure 3.19:** $V$–$g$ (upper) and $V$–$f$ (lower) plots of the full model and hybrid model at $h = 1000\,\text{m}$, with increasing speed.

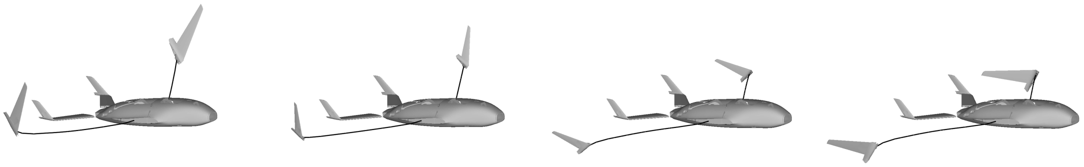

**(a)** $\phi = 0°$ **(b)** $\phi = 60°$ **(c)** $\phi = 120°$ **(d)** $\phi = 180°$

**Figure 3.20:** Mode shape of symmetric BTF at $V =$ 64.55 m/s and flight altitude $h = 1000\,\text{m}$, for different phase angles $\phi$.

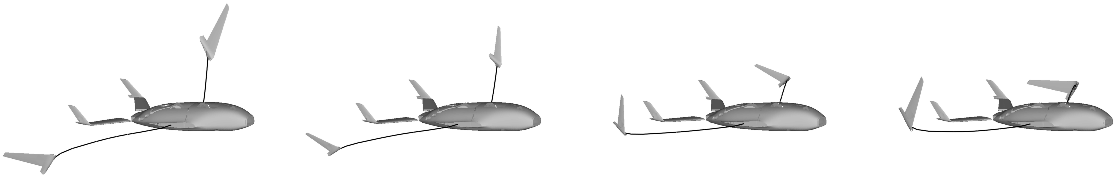

**(a)** $\phi = 0°$ **(b)** $\phi = 60°$ **(c)** $\phi = 120°$ **(d)** $\phi = 180°$

**Figure 3.21:** Mode shape of antisymmetric BTF at $V =$ 74.08 m/s and flight altitude $h = 1000\,\text{m}$, for different phase angles $\phi$.

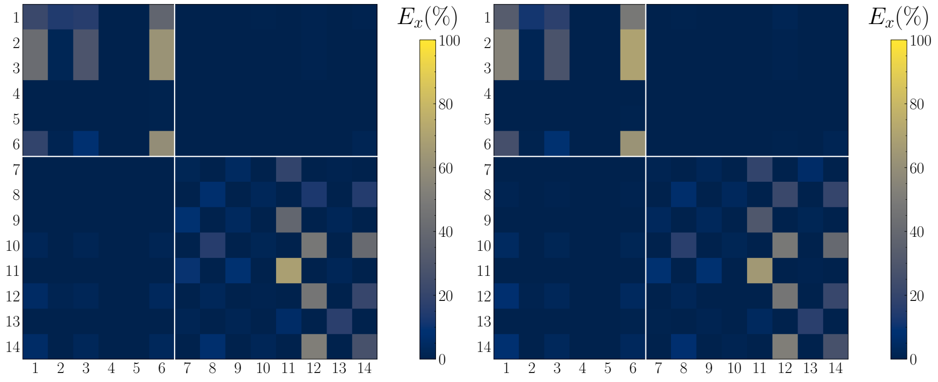

**(a)** $V = 64.55\text{m/s}$ **(b)** $V = 74.08\text{m/s}$

**Figure 3.22:** Comparison of the aeroelastic mode shapes of the reference GFEM and hybrid model at both flutter points at a flight altitude $h = 1000\,\text{m}$, showing an RMS error of $E_x = 15.67\%$ and $E_x = 16.45\%$, respectively.

## 3.3 Flutter Mechanism Investigation through Parametric Studies

This section presents the results of the parametric study based on the parameterization strategy introduced in Section 2.3. Key aerodynamic shape and structural parameters are systematically varied to explore the design space of the very flexible BWB configuration. Only one parameter is varied at a time.

The sensitivity of natural frequency and onset flutter speed to each parameter is quantified, with particular emphasis on identifying those that most effectively raise the flutter boundary. Furthermore, transitions between flutter mechanisms are identified, including shifts from classical bending-torsion flutter to body-freedom flutter.

**Table 3.9:** Design points considered in the parametric sweep. Configuration 50 of the parameter sweep corresponds to the baseline model.

| **Parameter** | | **Parameter sweep** | | | | | **Step** |
|---|---|---|---|---|---|---|---|
| | | 0 | 25 | 50 | 75 | 100 | |
| $\Lambda_{c/4}$ | 🟦 | 21° | 27° | 32.84° | 39° | 45° | 0.24° |
| $\phi$ | 🟧 | 0.35° | 1.85° | 3.36° | 4.85° | 6.35° | 0.06° |
| AR | 🟩 | 6.55 | 7.55 | 8.55 | 9.55 | 10.55 | 0.04 |
| EI | 🟥 | 10.0% | 55.0% | 100.0% | 145.0% | 190.0% | 1.8% |
| GJ | 🟪 | 40.0% | 70.0% | 100.0% | 130.0% | 160.0% | 1.2% |
| $x_{\text{EA}}$ | 🟫 | $-0.40c_{\text{tip}}$ | $-0.15c_{\text{tip}}$ | $0.10c_{\text{tip}}$ | $+0.35c_{\text{tip}}$ | $+0.60c_{\text{tip}}$ | $+0.01c_{\text{tip}}$ |

### 3.3.1 Effect on the Natural Frequency of Elastic Modes

Table 3.9 summarizes the design variables and the values considered in the Design of Experiments (DOE). Figure 3.23 illustrates the sensitivity of elastic modes 7–10 to variations in structural parameters. From simple beam theory, the curves behave such as

$$f_{\text{bending}} \propto \frac{C}{L^2}\sqrt{\frac{\text{EI}}{\rho A}}, \quad f_{\text{torsion}} \propto \frac{C}{L}\sqrt{\frac{\text{GJ}}{\rho I_p}}, \tag{3.4}$$

where $f$ is natural frequency, $C$ is a constant, $L$ is the beam length, EI and GJ are bending stiffness and torsional stiffness, respectively, $\rho$ is the material density, $A$ is the cross sectional area and $I_p$ is the polar moment of inertia. These relationships provide a useful physical interpretation of the trends observed in the numerical results.

Among all parameters, aspect ratio (proportional to span length $L$), bending stiffness (EI), and torsional stiffness (GJ) dominate the modal response. These parameters exhibit the steepest slopes, but the curves gradually flatten at higher values. The saturation observed indicates that beyond a certain threshold, further increases produce only marginal gains in natural frequency. The monotonic behaviour observed across most parameters makes the modal response predictable.

Increasing aspect ratio up to 10.55 reduces the natural frequencies by approximately $-15\%$ to $-25\%$. Conversely, reducing the aspect ratio increases all elastic modes frequencies by $+25\%$ to $+45\%$. Increasing the sweep angle, which is proportional to span length $L$, consistently reduces the natural frequency of elastic modes 7–10, although its influence is moderate ( approximately $-10\%$ to $-15\%$).

Increasing bending stiffness up to 1.9 times the baseline value raises the natural frequencies by as much as $+30\%$, particularly for modes 7 and 10. Increasing torsional stiffness primarily affects modes 9 and 10 ($+20\%$). In contrast, reducing either stiffness parameter results in substantial frequency reductions (up to $-66\%$).

Shifting the elastic axis aft increases the natural frequencies of modes 7 and 8 by approximately $+10\%$ to $+15\%$, while having limited influence on higher-order modes. Similarly, variations in dihedral angle have minor impact on the overall modal response.

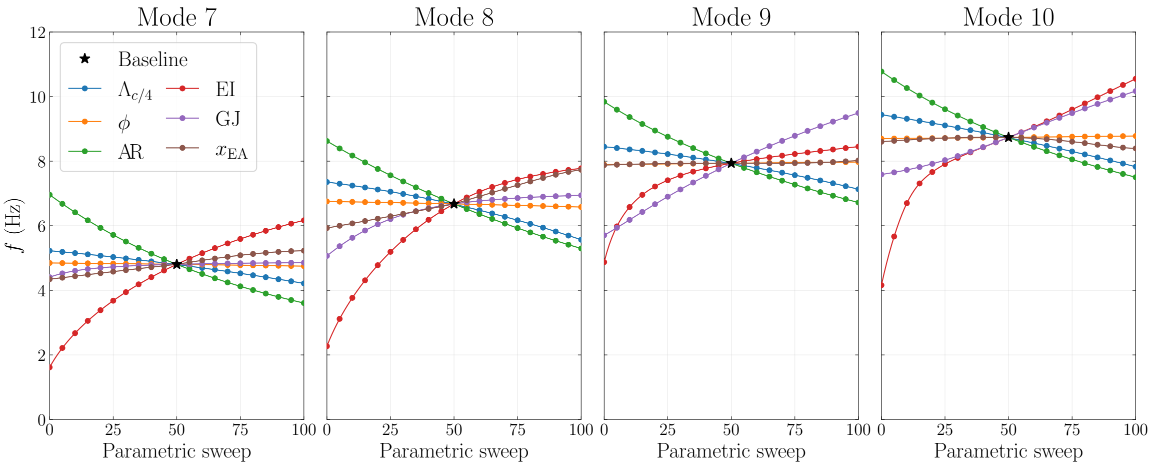

**Figure 3.23:** Effect of structural parameters on natural frequency of elastic modes 7–10. Modes 7 and 8 have a bending nature, whereas modes 9 and 10 are related to torsion deformation.

## 3.3.2 Raising the Flutter Boundary

Figure 3.24 presents the sensitivity of the two flutter points to variations in structural parameters and aerodynamic shape.

In the baseline configuration, both symmetric and antisymmetric bending-torsion flutter (BTF) modes were identified. Across the parameter sweep, the same underlying mechanisms persist. The first flutter point occurs when aeroelastic mode 9 becomes unstable. The flutter frequency plot in Figure 3.24 follows the aeroelastic mode 9 at the onset of instability and the trend closely follows the behaviour of elastic mode 9 in Figure 3.23.

The flutter speed evolution plot of Figure 3.24 reveals which parameters most effectively raise the flutter boundary. Reducing aspect ratio (+33.0% $V_{\text{BTF (S)}}$), moving the elastic axis forward (+9.1% $V_{\text{BTF (S)}}$), increasing sweep angle (+11.3% $V_{\text{BTF (S)}}$) or increasing torsional stiffness (+30.8% $V_{\text{BTF (S)}}$) can safely raise the onset flutter speed. In contrast, the bending stiffness curve shows a non-monotonic behaviour. Only within a limited interval (28% to 100% of the baseline EI), the parameter has a positive effect on the flutter speed (+4.6% $V_{\text{BTF (S)}}$). Outside this range, the benefit diminishes or reverses. Dihedral angle has negligible influence, altering flutter speed by less than 1%. Similar trends are observed for the second flutter point. An aeroelastic mode-tracking algorithm was implemented to ensure consistent identification of the governing instability mechanism across configurations.

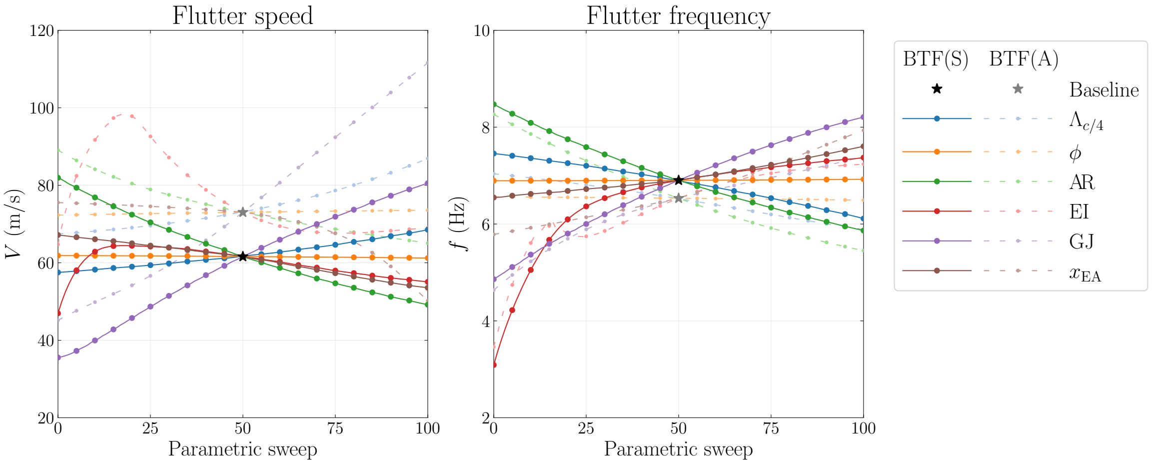

**Figure 3.24:** Effect of structural parameters on flutter speed and frequency for the first and second flutter modes.

# Chapter 4

# Concluding Remarks

This chapter concludes this thesis by revisiting its major developments and drawing conclusions and remarks from the findings of the work. Finally, an outlook on future research directions is given.

## 4.1 Conclusions

Novel aircraft configurations are being proposed to meet the demanding environmental goals of the future of aviation. The proposed configurations range from wings with an increased aspect ratio to completely novel designs, such as the blended-wing-body (BWB) configuration. These configurations show increased aerodynamic efficiency, resulting in a reduction in fuel consumption. At the same time, the tendency to lightweight composite flexible structures increases the susceptibility to coupled aeroelastic instabilities whose mechanisms may differ from classical bending-torsion flutter.

Within this context, this thesis pursued two objectives: (1) develop a model order reduction methodology that preserves the physical significance of the wing geometry while reproducing static, modal, and coupled aeroelastic response with high accuracy at reduced computational cost; and (2) build a parameterization framework that systematically explores the design space of the BWB configuration, quantifies the influence of each parameter on flutter onset, and characterizes the flutter mechanisms.

A high-fidelity baseline aeroelastic model of the BWB configuration was first developed to serve as a reference for subsequent reduction and parametric analyses. The structural model was assessed under a positive ultimate load case in accordance with CS/CFR 25.301 and CS/CFR 25.303[33, 34] requirements, ensuring that the structural response was representative of certification-level loading conditions.

The modal characterization of the full GFEM revealed the dominant bending and torsional modes governing the dynamic behaviour of the wing. The Modal Assurance Criterion (autoMAC) was systematically used to identify modal purity, harmonics, and coupling signatures between modes. Later, this criteria was used in a mode tracking algorithm within the optimization framework.

The aeroelastic analysis of the baseline configuration identified two distinct flutter phenomena within the flight envelope: a symmetric and an antisymmetric bending-torsion flutter. The identification and characterization of these two flutter modes provide a comprehensive understanding of the dynamic stability of the BWB and establish a reliable reference for the reduced-order model to reproduce the underlying physics of the flutter mechanisms.

An optimization framework was developed to calibrate a wing stick model (SM) to replace the flexible wings within a hybrid configuration, capable of reproducing the static deformation, modal characteristics, and coupled aeroelastic behavior of the baseline model. Dedicated error metrics were introduced to quantify the accuracy of the reduced-order model. For Case Study A, the vertical displacement and twist errors ($E_y$, $E_\theta$) were defined under positive ultimate loading. For Case Study B, frequency and mode shape discrepancies were quantified using $E_f, E_c, E_a$ error metrics for the first five elastic modes. The optimized stick models achieved strong agreement with the GFEM counterpart, with errors below 7% in vertical displacement, 3% in twist, 6% in natural frequencies, and approximately 20% in mode shapes. These results demonstrate that beam-like representations can capture deflection and resonance frequencies by properly tuning its stiffness properties.

There is limited evidence in the open literature that stick models reliably capture coupled aeroelastic behavior for complex configurations. Therefore, this thesis introduced two dedicated aeroelastic validation metrics: an eigenvalue error ($E_e$) based on the Error Vector Magnitude (EVM) concept for complex-valued signals, and a complex-eigenvector correlation error ($E_x$) designed to compare aeroelastic mode shapes in a robust and unified manner, overcoming the limitations of $E_c$ and $E_a$.

For Case Study C, the hybrid configuration predicted both symmetric and antisymmetric bending-torsion flutter mechanisms with errors below 3% in flutter speed and 8% in flutter frequency, while achieving an eigenvalue prediction error of 3% across the flight envelope. Although mode shape errors at flutter reached approximately 22%, the reduced model accurately captured the dominant instability mechanisms and their onset conditions.

Once the optimization was concluded, the stick models were validated to assess their applicability at a different loading condition (negative ultimate loading) and the aeroelastic response was determined at a different flight altitude. Results show that no single optimization strategy excelled in all metrics simultaneously. The stick model obtained from modal optimization emerged as the best overall configuration, performing consistently well across static, modal, and aeroelastic metrics and predicting accurately both flutter mechanisms with errors below 2% in flutter speed and below 6% in flutter frequency. The larger relative errors observed in twist were negligible in practice because the absolute values were small ($\Delta\theta < 1.5°$).

A limitation of the proposed optimization framework is that each case study targeted specific objectives separately. A unified multi-objective optimization including all seven error metrics could potentially yield a more globally optimal stick model. However, constructing and exploring a seven-dimensional Pareto front would require substantial computational resources and was beyond the scope of this work. Nevertheless, the present methodology establishes a systematic and transferable framework for stick model calibration and validation in coupled aeroelastic applications.

With the optimized hybrid model established, a parameterization framework was developed to explore the BWB design space efficiently. Six key parameters were identified and varied systematically: sweep angle, dihedral angle, aspect ratio, bending stiffness, torsional stiffness, and elastic axis position.

A first objective of the parametric study was to assess how the computational experiment relates to the fundamental physical trends. Particularly, the square-root dependence of natural frequencies on bending and torsional stiffness was clearly reproduced, as expected from beam theory. Conversely, increases in aspect ratio and sweep angle, which effectively increase structural length, led to reductions in modal frequencies.

The influence of each parameter on the flutter boundary was subsequently quantified. The study demonstrated that structural and geometric modifications can significantly alter the onset of bending-torsion flutter. But across the parametric sweep, the baseline symmetric and antisymmetric bending-torsion flutter mechanisms persisted as the governing instabilities. For instance, reducing the aspect ratio to 6.55 or increasing torsional stiffness to approximately 190% of the baseline value can increase the flutter speed by roughly 30%. These findings provide clear design guidelines for improving aeroelastic stability in BWB configurations.

However, these improvements must be interpreted with caution. Modifications that enhance flutter speed may adversely affect aerodynamic efficiency, structural weight, flight performance, or static stability. Moreover, the computational experiment evaluated approximately 600 configurations, a scale that is impractical for experimental validation through ground vibration tests or wind tunnel campaigns due to time and cost constraints. Therefore, experimental validation would require a carefully selected subset of representative configurations.

Despite these limitations, the parametric study successfully characterizes the evolution of flutter mechanisms across the design space and demonstrates the suitability of the hybrid reduced-order framework for large-scale exploratory studies.

## 4.2 Future Work

Several research directions naturally emerge from this work. First, additional dynamic analyses beyond classical flutter should be considered. Forced-response analyses, tuned discrete gust (TDG) simulations, and power spectral density (PSD) assessments would provide a more comprehensive characterization of the aeroelastic performance of the BWB configuration under realistic operational excitations.

Second, the model order reduction framework could be extended to a fully multi-objective optimization strategy, simultaneously minimizing static, modal, and aeroelastic error metrics. Advanced sampling or surrogate-based optimization techniques could mitigate the computational burden associated with high-dimensional Pareto front exploration.

Third, experimental validation represents a crucial next step. Ground vibration tests and wind tunnel campaigns on selected configurations would provide valuable data for further tuning and validating both the high-fidelity and reduced-order models. Such validation is essential to strengthen confidence in predictive aeroelastic simulations for unconventional aircraft.

Finally, the parameterization framework could be integrated into a multidisciplinary design optimization (MDO) environment, coupling aeroelastic stability with aerodynamic efficiency, structural weight, and flight performance constraints. This would enable a more holistic assessment of BWB configurations and support their maturation toward practical implementation.

In conclusion, this thesis contributes a systematic methodology for reduced-order aeroelastic modelling and parametric exploration of a BWB configuration. It demonstrates that physically meaningful stick models, when properly optimized and validated, can accurately reproduce complex coupled aeroelastic phenomena while significantly reducing computational cost, thereby enabling efficient exploration of unconventional aircraft design spaces.

# Bibliography

[1] European Commission. *2030 climate targets*. Accessed 05-28-2025. 2023.

[2] Government of Canada. *Canada's 2030 Emissions Reduction Plan*. Accessed 05-28-2025. 2022.

[3] Bashir Parveez et al. "Scientific Advancements in Composite Materials for Aircraft Applications: A Review". en. In: *Polymers* 14.22 (2022), p. 5007. DOI: `10.3390/polym14225007`.

[4] Yiyuan Ma and Ali Elham. "Designing high aspect ratio wings: A review of concepts and approaches". In: *Progress in Aerospace Sciences* 145 (2024), p. 100983. DOI: `https://doi.org/10.1016/j.paerosci.2024.100983`.

[5] H. Z. Hassan and N. M. Saeed. "Advancements and Applications of Lightweight Structures: A Comprehensive Review". en. In: *Discover Civil Engineering* 1 (2024). DOI: `10.1007/s44290-024-00049-z`.

[6] Mark A. Potsdam, Mark A. Page, and Robert H. Liebeck. "Blended Wing Body Analysis and Design". In: *15th Applied Aerodynamics Conference*. Atlanta, Georgia, USA: American Institute of Aeronautics and Astronautics, 1997. DOI: `10.2514/6.1997-2317`.

[7] R. H. Liebeck. "Blended Wing Body Design Challenges". en. In: *AIAA International Air and Space Symposium and Exposition: The Next 100 Years*. Dayton, Ohio, USA: American Institute of Aeronautics and Astronautics, 2003, pp. 1–12. DOI: `10.2514/6.2003-2659`.

[8] R. H. Liebeck. "Design of the Blended Wing Body Subsonic Transport". en. In: *Journal of Aircraft* 41.1 (2004), pp. 10–25. DOI: `10.2514/1.9084`.

[9] A. R. Collar. "The Expanding Domain of Aeroelasticity". en. In: *The Journal of the Royal Aeronautical Society* 50.428 (1946), pp. 613–636. DOI: `10.1017/S0368393100120358`.

[10] Raymond L. Bisplinghoff, Holt Ashley, and Robert L. Halfman. *Aeroelasticity*. en. Reading, Massachusetts: Addison-Wesley Publishing Company, 1955.

[11] G. J. Hancock, J. R. Wright, and A. Simpson. "On the Teaching of the Principles of Wing Flexure–Torsion Flutter". en. In: *The Aeronautical Journal* 89.888 (1985), pp. 285–305. DOI: `10.1017/S0001924000015050`.

[12] J. R. Banerjee. "Flutter characteristics of high aspect ratio tailless aircraft". en. In: *Journal of Aircraft* 21.9 (1984), pp. 733–736. DOI: `10.2514/3.45022`.

[13] J. R. Banerjee. "Flutter modes of high aspect ratio tailless aircraft". en. In: *Journal of Aircraft* 25.5 (1988), pp. 473–476. DOI: `10.2514/3.45607`.

[14] Federal Aviation Administration. *Part 23 - Airworthiness Standards: Normal Category Airplane*. Accessed 05-28-2025. 2023.

[15] European Union Aviation Safety Agency. *Easy Access Rules for Large Aeroplanes (CS-25)*. Accessed 05-28-2025. 2023.

[16] Canadian Aviation Regulations. *Part V — Airworthiness*. Accessed 05-28-2025. 2021.

[17] Dale Pitt, Brian Hayes, and Charles Goodman. "F/A-18E/F Aeroservoelastic Design, Analysis, and Test". en. In: *44th AIAA/ASME/ASCE/AHS/ASC Structures, Structural Dynamics, and Materials Conference*. Norfolk, Virginia: American Institute of Aeronautics and Astronautics, Apr. 2003. DOI: `10.2514/6.2003-1880`.

[18] Gaëtan Kerschen et al. "Past, present and future of nonlinear system identification in structural dynamics". en. In: *Mechanical Systems and Signal Processing* 20.3 (Apr. 2006), pp. 505–592. DOI: `10.1016/j.ymssp.2005.04.008`.

[19] S.A. Fazelzadeh, A. Mazidi, and H. Kalantari. "Bending-torsional flutter of wings with an attached mass subjected to a follower force". en. In: *Journal of Sound and Vibration* 323.1-2 (June 2009), pp. 148–162. DOI: `10.1016/j.jsv.2009.01.002`.

[20] P.K. Datta and S. Biswas. "Aeroelastic Behaviour of Aerospace Structural Elements with Follower Force: A Review". en. In: *International Journal of Aeronautical and Space Sciences* 12.2 (June 2011), pp. 134–148. DOI: `10.5139/IJASS.2011.12.2.134`.

[21] Arnaldo Delli Carri et al. “Extending modal testing technology for model validation of engineering structures with sparse nonlinearities: A first case study”. en. In: *Mechanical Systems and Signal Processing* 84 (Feb. 2017), pp. 97–115. DOI: `10.1016/j.ymssp.2016.04.012`.

[22] Paul Vazhayil Thomas, Mostafa S. A. ElSayed, and Denis Walch. “Review of Model Order Reduction Methods and Their Applications in Aeroelasticity Loads Analysis for Design Optimization of Complex Airframes”. en. In: *Aerospace* 9.2 (2022), p. 65. DOI: `10.3390/aerospace9020065`.

[23] Leonard Bairstow and Arthur Fage. *Oscillations of the Tailplane and Body of an Aircraft in Flight.* en. Tech. rep. Aeronautical Research Committee (ARC), 1916.

[24] R. A. Frazer and W. J. Duncan. *The Flutter of Aeroplane Wings.* en. London: H. M. Stationery Office, 1929.

[25] R. A. Frazer and W. J. Duncan. *The flutter of monoplanes, biplanes and tail units.* en. Tech. rep. 1255. Aeronautical Research Committee, Aeronautical Research Council (ARC), 1931.

[26] Alfred Cox H. Roxbee Pugsley. *Theory of loss of lateral control due to wing twisting.* London: HMSO, 1933.

[27] J. Hanson. “Critical Speeds of Monoplanes”. In: *The Journal of the Royal Aeronautical Society* 41.320 (1937), pp. 703–726. DOI: `10.1017/S0368393100108168`.

[28] Eli Livne. “The Future of Airplane Aeroelasticity”. en. In: *Journal of Aircraft* 40.6 (2003), pp. 1066–1092. DOI: `10.2514/2.7218`.

[29] Y. C. Fung. *An Introduction to the Theory of Aeroelasticity.* en. Mineola, New York: Courier Dover Publications, 2008.

[30] Terrence A. Weisshaar. “Static and Dynamic Aeroelasticity”. en. In: *Encyclopedia of Aerospace Engineering.* John Wiley & Sons, Ltd., 2010. DOI: `10.1002/9780470686652.eae149`.

[31] W.P. Rodden. *Theoretical and Computational Aeroelasticity.* Crest Pub., 2011.

[32] Jan R. Wright and Jonathan E. Cooper. *Introduction to Aircraft Aeroelasticity and Loads.* en. 2nd ed. Chichester: Wiley, 2015.

[33] European Aviation Safety Agency. *Certification Specifications for Large Aeroplanes (CS-25).* 2023.

[34] Federal Aviation Administration. *14 CFR Part 25 - Airworthiness Standards: Transport Category Airplanes.* 2024.

[35] Eirikur Jonsson et al. “Flutter and post-flutter constraints in aircraft design optimization”. en. In: *Progress in Aerospace Sciences* 109 (2019), p. 100537. DOI: `10.1016/j.paerosci.2019.04.001`.

[36] R. Kassner and H. Fingado. “The Two-Dimensional Problem of Wing Vibration”. In: *The Journal of the Royal Aeronautical Society* 41.322 (1937), pp. 921–944. DOI: `10.1017/S0368393100103499`.

[37] Theodore Theodorsen. *General Theory of Aerodynamic Instability and the Mechanism of Flutter.* Technical Report NACA TR 496. National Advisory Committee for Aeronautics (NACA), 1949.

[38] William Bollay and Charles D. Brown. “Some Experimental Results on Wing Flutter”. In: *Journal of the Aeronautical Sciences* 8.8 (1941), pp. 313–318. DOI: `10.2514/8.10724`.

[39] G. Schweiger and G. Sensburger. *Aeroelastic Problems and Structural Design of a Tailless CFC-Sailplane.* Tech. rep. Munich and Braunschweig, Germany: Messerschmitt-Bölkow-Blohm GmbH and Technische Universität Braunschweig, 1983.

[40] LL. T Niblett. “The fundamentals of body-freedom flutter”. In: *The Aeronautical Journal* 90.899 (1986), pp. 373–377. DOI: `10.1017/S0001924000015979`.

[41] D. R. Gaukroger. *Wind-Tunnel Tests on the Symmetric and Antisymmetric Flutter of Swept-Back Wings.* en. Tech. rep. London: Aeronautical Research Council, 1955.

[42] E. Livne and Terrence A. Weisshaar. “Aeroelasticity of Nonconventional Airplane Configurations — Past and Future”. en. In: *AIAA Journal* (2012). DOI: `10.2514/2.7217`.

[43] E. Livne, T. Lee, and T. Wang. “Aeroelasticity of Joined-Wing Airplane Configurations: Past Work and Future Challenges - A Survey”. en. In: *AIAA/ ASME/ ASC Structures, Structural Dynamics and Materials Conference.* 2001-1370. 2001. DOI: `10.2514/6.2001-1370`.

[44] M. C. van Schoor and A. H. von Flotow. “Aeroelastic Characteristics of a Highly Flexible Aircraft”. en. In: *Journal of Aircraft* 27.10 (1990), pp. 901–908. DOI: `10.2514/3.45955`.

[45] Mayuresh J. Patil, Dewey H. Hodges, and Carlos E. S. Cesnik. “Characterizing the Effects of Geometrical Nonlinearities on Aeroelastic Behaviour of High-Aspect-Ratio Wings”. en. In: *AIAA Journal* 38.12 (2000), pp. 2240–2250. DOI: `10.2514/2.901`.

[46] Mayuresh J. Patil, Dewey H. Hodges, and Carlos E. S. Cesnik. “Nonlinear Aeroelasticity and Flight Dynamics of High-Altitude Long-Endurance Aircraft”. en. In: *AIAA Journal* 39.8 (2001), pp. 1510–1518. DOI: `10.2514/2.1485`.

[47] M. J. Patil and D. H. Hodges. “On the Importance of Aerodynamic and Structural Geometrical Nonlinearities in Aeroelastic Behaviour of High-Aspect-Ratio Wings”. en. In: *Journal of Fluids and Structures* 22.4 (2006), pp. 617–628. DOI: `10.1016/j.jfluidstructs.2005.12.002`.

[48] Rafael Palacios, Carlos E. S. Cesnik, and Eric Reichenbach. “A Re-Examination of the Structural Design Procedures for Very Flexible Aircraft”. en. In: *46th AIAA/ ASME/ ASCE/ AHS/ ASC Structures, Structural Dynamics and Materials Conference.* AIAA 2005-1945. 2005. DOI: `10.2514/6.2005-1945`.

[49] Mark Drela. *Method for Simultaneous Wing Aerodynamic and Structural Load Prediction.* Tech. rep. MIT Aeronautics and Astronautics Technical Report. Massachusetts Institute of Technology, 1990. DOI: `10.2514/3.25342`.

[50] Mark Drela. *ASWING: Integrated Simulation Model for Preliminary Aerodynamic, Structural, and Control-Law Design of Aircraft.* Tech. rep. ASWING Technical Documentation. Massachusetts Institute of Technology, 1998. DOI: `10.2514/6.1999-1394`.

[51] Weihua Su and Carlos E. S. Cesnik. “Dynamic Response of Highly Flexible Flying Wings”. en. In: *47th AIAA/ASME/ASCE/AHS/ASC Structures, Structural Dynamics and Materials Conference.* AIAA 2006-1636. 2006. DOI: `10.2514/6.2006-1636`.

[52] Weihua Su and Carlos E. S. Cesnik. “Nonlinear Aeroelasticity of a Very Flexible Blended-Wing-Body Aircraft”. en. In: *AIAA Journal* (2012). DOI: `10.2514/1.47317`.

[53] Frederico Afonso et al. “A review on non-linear aeroelasticity of high aspect-ratio wings”. en. In: *Progress in Aerospace Sciences* 89 (2017), pp. 40–57. DOI: `10.1016/j.paerosci.2016.12.004`.

[54] Frederico Afonso et al. "Strategies towards a more sustainable aviation: A systematic review". en. In: *Progress in Aerospace Sciences* (2022), p. 100878. DOI: `10.1016/j.paerosci.2022.100878`.

[55] Junaid Najmi et al. "Aeroelastic tailoring for aerospace applications". en. In: *Heliyon* (2024). DOI: `10.1016/j.heliyon.2024.e24151`.

[56] Eli Livne. "Aircraft Active Flutter Suppression: State of the Art and Technology Maturation Needs". en. In: *AIAA Journal* (2017). DOI: `10.2514/1.C034442`.

[57] David Lucia. "The SensorCraft Configurations: A Non-Linear AeroServoElastic Challenge for Aviation". en. In: *46th AIAA/ASME/ASCE/AHS/ASC Structures, Structural Dynamics and Materials Conference*. Austin, Texas: American Institute of Aeronautics and Astronautics, Apr. 2005. DOI: `10.2514/6.2005-1943`.

[58] JetZero. *The Future Takes Shape*. en. `https://www.jetzero.aero`. Accessed 09-25-2025. 2025.

[59] Airbus. *Imagine travelling in this blended wing body aircraft: The Airbus MAVERIC demonstrator is pushing innovative aircraft design to the limit*. en. `https://www.airbus.com/en/newsroom/stories/2020-11-imagine-travelling-in-this-blended-wing-body-aircraft`. Online; accessed 05-September-2025. 2020.

[60] Bombardier. *EcoJet Research Project*. en. `https://bombardier.com/en/ecojets`. Accessed 09-25-2025. 2025.

[61] S. Jacobson et al. "Residual pitch oscillation (RPO) flight test and analysis on the B-2 bomber". en. In: *39th AIAA/ASME/ASCE/AHS/ASC Structures, Structural Dynamics, and Materials Conference and Exhibit*. 1998-1805. 1998. DOI: `10.2514/6.1998-1805`.

[62] R. T. Britt et al. *Aeroservoelastic Characteristics of the B-2 Bomber and Implications for Future Large Aircraft*. en. Tech. rep. Northrop Grumman / U.S. Air Force / RTO AVT Specialists' Meeting, 2000.

[63] C. Gelzer. *X-48B Blended Wing Body*. en. `https://www.nasa.gov/aeronautics/x-48b/`. Accessed 07-25-2025. 2010.

[64] Jihai Liu et al. "Flutter Modeling, Analysis and Test for Blended-Wing-Body Flying Wing". en. In: *Proceedings of the 2018 Asia-Pacific International Symposium on Aerospace Technology (APISAT 2018)*. Ed. by Sung Chul Kim et al. Singapore: Springer, 2019, pp. 1017–1028. DOI: `10.1007/978-981-13-3305-7_78`.

[65] Pengtao Shi et al. "Full-Span Flying Wing Wind Tunnel Test: A Body Freedom Flutter Study". en. In: *Fluids* 5.1 (2020), p. 34. DOI: `10.3390/fluids5010034`.

[66] Pengtao Shi et al. "The Development of a Flight Test Platform to Study the Body Freedom Flutter of BWB Flying Wings". en. In: *Aerospace* 8.12 (2021), p. 390. DOI: `10.3390/aerospace8120390`.

[67] Yingsong Gu and Pengtao Shi. "Body Freedom Flutter of Scaled Vehicles: From Blended Wing Body to Conventional Configuration". en. In: *Proceedings of the International Forum on Aeroelasticity and Structural Dynamics (IFASD 2024)*. The Hague, The Netherlands, June 2024.

[68] Yingsong Gu. "Body Freedom Flutter of a Blended Wing Body Model Coupled with Flight Control System". en. In: *Procedia Engineering* 99 (2015), pp. 850–858. DOI: `10.1016/j.proeng.2014.12.506`.

[69] Pengxuan Lei et al. "Verification of a Body Freedom Flutter Numerical Simulation Method Based on Main Influence Parameters". en. In: *Machines* 9.10 (2021), p. 243. DOI: `10.3390/machines9100243`.

[70] Daniel Strong et al. "Flutter Analysis of Wing Configurations Using Pre-Stressed Frequencies and Mode Shapes". en. In: *46th AIAA/ ASME/ ASCE/ AHS/ ASC Structures, Structural Dynamics and Materials Conference*. AIAA 2005-2173. 2005. DOI: `10.2514/6.2005-2173`.

[71] Philip Beran et al. "Static Nonlinear Aeroelastic Analysis of a Blended Wing Body". en. In: *46th AIAA/ ASME/ ASCE/ AHS/ ASC Structures, Structural Dynamics and Materials Conference*. Austin, Texas: American Institute of Aeronautics and Astronautics, Apr. 2005. DOI: `10.2514/6.2005-1944`.

[72] Daniel Paulus et al. "The Integration of an Efficient High Lift System in the Design Process of a Blended Wing Body Aircraft". en. In: *12th AIAA Aviation Technology, Integration, and Operations (ATIO) Conference and 14th AIAA/ISSMO Multidisciplinary Analysis and Optimization Conference*. AIAA 2012-5650. 2012. DOI: `10.2514/6.2012-5650`.

[73] Charles Harvard Gibbs-Smith. *Aviation: An Historical Survey from Its Origins to the End of World War II.* en. London: H. M. Stationery Office, 1970.

[74] Terrance A. Weisshaar and Holt Ashley. “Static Aeroelasticity and the Flying Wing”. en. In: *Journal of Aircraft* 10.10 (1973), pp. 586–594. DOI: `10.2514/3.60265`.

[75] Terrence A. Weisshaar and Holt Ashley. “Static Aeroelasticity and the Flying Wing, Revisited”. en. In: *Journal of Aircraft* 23.4 (1986), pp. 293–300. DOI: `10.2514/3.44409`.

[76] Edward Burnett et al. “NDOF Simulation Model for Flight Control Development with Flight Test Correlation”. en. In: *50th AIAA Structures, Structural Dynamics, and Materials Conference.* AIAA 2010-7780. 2010. DOI: `10.2514/6.2010-7780`.

[77] Jessica R. Jones and Carlos E. S. Cesnik. “Nonlinear Aeroelastic Analysis of the X-56A Multi-Utility Aeroelastic Demonstrator”. en. In: *57th AIAA/ ASCE/ AHS/ ASC Structures, Structural Dynamics, and Materials Conference.* AIAA 2016-1799. 2016. DOI: `10.2514/6.2016-1799`.

[78] Jacob Schaefer et al. *Flying Beyond Flutter with the X-56A Aircraft.* en. Tech. rep. NASA/TM-20220012337. Edwards, California: NASA Armstrong Flight Research Center, 2023.

[79] Norman H. Zimmerman and Jason T. Weissenburger. “Prediction of Flutter Onset Speed Based on Flight Testing at Subcritical Speeds”. en. In: *AIAA Journal* 16.7 (1978), pp. 705–712. DOI: `10.2514/3.43581`.

[80] Karl Nickel and Michael Wohlfahrt. *Tailless Aircraft in Theory and Practice.* en. Washington, D.C.: American Institute of Aeronautics and Astronautics, 1994.

[81] Michael Love et al. “Body Freedom Flutter of High Aspect Ratio Flying Wings”. en. In: *46th AIAA/ASME/ASCE/AHS/ASC Structures, Structural Dynamics and Materials Conference.* AIAA 2005-1947. 2005. DOI: `10.2514/6.2005-1947`.

[82] Eric Vartio et al. “Structural Modal Control and Gust Load Alleviation for a SensorCraft Concept”. en. In: *46th AIAA/ASME/ASCE/AHS/ASC Structures, Structural Dynamics and Materials Conference.* AIAA 2005-1946. 2005. DOI: `10.2514/6.2005-1946`.

[83] Jeff Beranek et al. “Conceptual Design of a Multi-Utility Aeroelastic Demonstrator”. en. In: *13th AIAA/ISSMO Multidisciplinary Analysis and Optimization Conference*. 2010. DOI: `10.2514/6.2010-9350`.

[84] Thomas E. Noll and et al. *Investigation of the Helios Prototype Aircraft Mishap*. en. Tech. rep. NASA/TM-2004-212280. Hampton, Virginia: NASA Langley Research Center, 2004.

[85] Julian Theis, Harald Pfifer, and Peter Seiler. “Robust Modal Damping Control for Active Flutter Suppression”. en. In: *AIAA Journal* (2020). DOI: `10.2514/1.G004846`.

[86] Qitong Zou and Rui Huang. “Body-Freedom Flutter Analysis and Flight Test for a Flying-Wing Aircraft Testbed”. en. In: *Mechanical Systems and Signal Processing* 210 (2024), p. 111717. DOI: `10.1016/j.ymssp.2024.111717`.

[87] Elijah Hao Wei Ang and Daryl Jieli Leo. “Wind tunnel experiments of bending-torsion and body-freedom flutter on flying wing unmanned aerial vehicles”. en. In: *Aerospace Science and Technology* 140 (2023), p. 108798. DOI: `10.1016/j.ast.2023.108798`.

[88] Elijah Hao Wei Ang. “Wind Tunnel Experiment for Body Freedom Flutter of Flying Wing Unmanned Aerial Vehicle”. en. In: *Proceedings of the International Forum on Aeroelasticity and Structural Dynamics (IFASD 2024)*. The Hague, The Netherlands, June 2024.

[89] Markus Ritter et al. “Collaborative Pazy Wing Analyses for the Third Aeroelastic Prediction Workshop”. en. In: *AIAA Scitech 2024 Forum*. AIAA 2024-0419. 2024. DOI: `10.2514/6.2024-0419`.

[90] Markus Ritter et al. “Experimental Aeroelastic Benchmark of a Very Flexible Wing”. en. In: *AIAA Journal* 60.3 (2022), pp. 1–24. DOI: `10.2514/1.J060621`.

[91] C. P. Tilmann et al. “High Altitude Long Endurance Technologies for Sensor-Craft”. en. In: *RTO AVT-099 Symposium on Novel and Emerging Vehicle and Vehicle Technology Concepts*. MP-104-P26. Brussels, Belgium, 2003.

[92] Benjamin P. Hallissy and Carlos E. S. Cesnik. “High-Fidelity Aeroelastic Analysis of Very Flexible Aircraft”. en. In: *51st AIAA/ASME/ASCE/AHS/ASC Structures, Structural Dynamics, and Materials Conference*. AIAA 2010-2963. Orlando, Florida, 2010. DOI: `10.2514/6.2010-2963`.

[93] Rafael Palacios and Carlos E. S. Cesnik. “Static Nonlinear Aeroelasticity of Flexible Slender Wings in Compressible Flow”. en. In: *43rd AIAA/ ASME/ ASCE/ AHS/ ASC Structures, Structural Dynamics and Materials Conference.* AIAA 2002-1936. 2002. DOI: `10.2514/6.2002-1936`.

[94] Carlos E. S. Cesnik et al. “X-HALE: A Very Flexible Unmanned Aerial Vehicle for Nonlinear Aeroelastic Tests”. en. In: *AIAA Journal* 50.12 (2012), pp. 2820–2832. DOI: `10.2514/1.J051392`.

[95] Julian Wolkovitch. “The Joined Wing — An Overview”. en. In: *Journal of Aircraft* 24.2 (1987), pp. 151–158. DOI: `10.2514/3.45285`.

[96] S. Smith, S. Cliff, and I. Kroo. “The Design of a Joined Wing Flight Demonstrator Aircraft”. en. In: *28th AIAA/ASME/ASCE/AHS/ASC Structures, Structural Dynamics and Materials Conference.* AIAA 1987-2930. 1987. DOI: `10.2514/6.1987-2930`.

[97] Mary Fairchild Samuels. “Structural Weight Comparison of a Joined Wing and a Conventional Wing”. en. In: *Journal of Aircraft* 23.2 (1986), pp. 162–168. DOI: `10.2514/3.57418`.

[98] E. V. Laitone. “Prandtl’s Biplane Theory Applied to Canard and Tandem Aircraft”. en. In: *Journal of Aircraft* 14.3 (1977), pp. 305–310. DOI: `10.2514/3.44653`.

[99] Terrence A. Weisshaar and D. H. Lee. “Aeroelastic Tailoring of Joined-Wing Configurations”. en. In: *43rd AIAA/ASME/ASCE/AHS/ASC Structures, Structural Dynamics, and Materials Conference.* AIAA 2002-1207. 2002. DOI: `10.2514/6.2002-1207`.

[100] M. Goland. “The Flutter of a Uniform Cantilever Wing”. en. In: *Journal of Applied Mechanics* 12.4 (1945), A197–A208.

[101] Norizham Abdul Razak, Thomas Andrianne, and Grigorios Dimitriadis. “Flutter and Stall Flutter of a Rectangular Wing in a Wind Tunnel”. en. In: *AIAA Journal* 50.10 (2012), pp. 2156–2167. DOI: `10.2514/1.J051041`.

[102] Casey Fagley. “Aero-Servo-Elastic Control of a Cyber-Physical Flexible Wing”. en. In: *54th AIAA Aerospace Sciences Meeting.* AIAA 2016-0320. 2016. DOI: `10.2514/6.2016-0320`.

[103] A. Suleman et al. “Non-linear Aeroelastic Analysis in the Time Domain of High-Aspect-Ratio Wings: Effect of Chord and Taper-Ratio Variation”. en. In: *The Aeronautical Journal* 121.1235 (2017), pp. 21–53. DOI: `10.1017/aer.2016.94`.

[104] F. Afonso et al. “Non-linear Aeroelastic Response of High Aspect-Ratio Wings in the Frequency Domain”. en. In: *The Aeronautical Journal* 121.1240 (2017), pp. 858–876. DOI: `10.1017/aer.2017.29`.

[105] Andrea Iannelli, Andrés Marcos, and Mark Lowenberg. “Study of Flexible Aircraft Body Freedom Flutter with Robustness Tools”. en. In: *Journal of Guidance, Control, and Dynamics* 41.5 (2018), pp. 1083–1094. DOI: `10.2514/1.G003165`.

[106] Kemin Zhou, John C. Doyle, and Keith Glover. *Robust and Optimal Control*. en. Upper Saddle River, New Jersey: Prentice Hall, 1996.

[107] John C. Doyle. “Analysis of Feedback Systems with Structured Uncertainties”. en. In: *IEE Proceedings D: Control Theory and Applications* 129.6 (1982), pp. 242–250. DOI: `10.1049/ip-d.1982.0053`.

[108] M. Bras, S. Warwick, and A. Suleman. “Aeroelastic Evaluation of a Flexible High Aspect Ratio Wing UAV: Numerical Simulation and Experimental Flight Validation”. en. In: *Aerospace Science and Technology* 128 (2022), p. 107400. DOI: `10.1016/j.ast.2022.107400`.

[109] M. J. Patil and D. H. Hodges. “Limit-Cycle Oscillations in High-Aspect-Ratio Wings”. en. In: *AIAA Journal* 40.10 (2002), pp. 1992–2001. DOI: `10.2514/2.1888`.

[110] Carlos E. S. Cesnik and Weihua Su. “Nonlinear Aeroelastic Modeling and Analysis of Fully Flexible Aircraft”. en. In: *46th AIAA/ASME/ASCE/AHS/ASC Structures, Structural Dynamics, and Materials Conference*. AIAA 2005-2169. Austin, Texas, 2005. DOI: `10.2514/6.2005-2169`.

[111] R. Cavallaro et al. “PrandtlPlane Joined Wing: Body freedom flutter, limit cycle oscillation and freeplay studies”. en. In: *Journal of Fluids and Structures* 61 (2016), pp. 212–230. DOI: `10.1016/j.jfluidstructs.2015.08.016`.

[112] Michael H. Shirk, Terrence J. Hertz, and Terrence A. Weisshaar. “Aeroelastic Tailoring—Theory, Practice, and Promise”. en. In: *Journal of Aircraft* 23.1 (1986), pp. 6–18. DOI: `10.2514/3.45260`.

[113] R. J. Guyan. “Reduction of Stiffness and Mass Matrices”. en. In: *AIAA Journal* 3.2 (1965), p. 380. DOI: `10.2514/3.2874`.

[114] J. C. O’Callahan. “A Procedure for an Improved Reduced System (IRS) Model”. en. In: *Proceedings of the 7th International Modal Analysis Conference (IMAC)*. Union College. Schenectady, New York, 1989, pp. 17–21.

[115] M. C. Bampton and R. R. Jr. Craig. “Coupling of Substructures for Dynamic Analyses”. en. In: *AIAA Journal* 6.7 (1968), pp. 1313–1319. DOI: `10.2514/3.4741`.

[116] Mostafa S. A. El Sayed et al. “Monitor Points Method for Loads Recovery in Static/Dynamic Aeroelasticity Analysis with Hybrid Airframe Representation”. en. In: *SAE 2013 AeroTech Congress & Exhibition*. 2013-01-2142. Montreal, Canada: SAE International, 2013. DOI: `10.4271/2013-01-2142`.

[117] Paul V. Thomas, Mostafa S. A. Elsayed, and Denis Walch. “Model Order Reduction of Complex Airframes Using Component Mode Synthesis for Dynamic Aeroelasticity Load Analysis”. en. In: *Journal of Mechanics Engineering and Automation* 8.2018 (2018), pp. 145–155. DOI: `10.17265/2159-5275/2018.04.001`.

[118] P. V. Thomas, M. S. A. Elsayed, and D. Walch. “Development of High-Fidelity Reduced Order Hybrid Stick Model Representation for Aeroelastic Analysis”. en. In: *Thin-Walled Structures* 139 (2019), p. 107409. DOI: `10.1016/j.tws.2019.107409`.

[119] M. Abdo et al. “Transonic Aerodynamics of Flexible Wings”. en. In: *Proceedings of the 48th Annual General Meeting and Conference of the Canadian Aeronautics and Space Institute (CASI)*. Toronto, Canada, 2001.

[120] M. S. A. Elsayed, R. Sedaghati, and M. Abdo. “Accurate Stick Model Development for Static Analysis of Complex Aircraft Wing-Box Structures”. en. In: *AIAA Journal* 47.9 (2009), pp. 2063–2075. DOI: `10.2514/1.38447`.

[121] M. Abdo et al. “Equivalent Finite Element Wing Structural Models Used for Aerodynamics–Structures Interaction”. en. In: *Proceedings of the 50th Annual General Meeting and Conference of the Canadian Aeronautics and Space Institute (CASI) and 16th Aerospace Structures and Materials Symposium*. Montréal, Canada, Apr. 2003.

[122] G. Bindolino et al. “Multilevel Structural Optimization for Preliminary Wing-Box Weight Estimation”. en. In: *Journal of Aircraft* 46.2 (2009), pp. 475–489. DOI: `10.2514/1.41552`.

[123] Guillaume Corriveau and Franck Dervault. “Impact of Wing Box Geometrical Parameters on Stick Model Prediction Accuracy”. en. In: *54th AIAA/ ASME/ ASCE/ AHS/ ASC Structures, Structural Dynamics, and Materials Conference*. AIAA 2013-1810. Advanced Structures, Bombardier Aerospace. Boston, Massachusetts, Apr. 2013. DOI: `10.2514/6.2013-1810`.

[124] M. Hashemi-Kia and M. Toossi. *Development and Application of a Technique for Reducing Airframe Finite Element Models for Dynamic Analysis*. en. Tech. rep. NASA-CR-187448. NASA, 1990.

[125] Ugur Hayirli. “Stick Model Development of Aircraft Structures for Dynamic Analysis”. en. In: *58th AIAA/ASCE/AHS/ASC Structures, Structural Dynamics, and Materials Conference*. AIAA 2017-0407. Grapevine, Texas, Jan. 2017. DOI: `10.2514/6.2017-0407`.

[126] P. Piperni, M. Abdo, and F. Kafyeke. “The Application of Multi-Disciplinary Optimization Technologies to the Design of a Business Jet”. en. In: *10th AIAA/ ISSMO Multidisciplinary Analysis and Optimization Conference*. AIAA 2004-4530. Albany, New York, Aug. 2004. DOI: `10.2514/6.2004-4370`.

[127] S. Corn, J. Piranda, and N. Bouhaddi. “Simplification of Finite Element Models for Structures Having a Beam-Like Behaviour”. en. In: *Mechanical Systems and Signal Processing* 13.4 (1999), pp. 605–625. DOI: `10.1006/jsvi.1999.2746`.

[128] S. P. Timoshenko. *Strength of Materials, Part I: Elementary Theory and Problems*. en. D. Van Nostrand Company, 1955.

[129] Leonhard Euler. “Elastic Curves”. en. In: *Isis* 20.1 (1933). English translation of Euler’s 1744 work, pp. 1–25.

[130] Alex Kratochvil. “A New Approach of Creating a Finite Element Stick Model for Flutter Analysis”. en. In: *MATEC Web of Conferences*. Vol. 304. 2019, p. 01015. DOI: `10.1051/matecconf/201930401015`.

[131] Rafael Palacios et al. “Condensation of Large Finite-Element Models for Wing Load Analysis with Geometrically-Nonlinear Effects”. en. In: *AIAA SciTech Forum*. AIAA 2014-0778. 2014. DOI: `10.2514/6.2014-0778`.

[132] D. C. Kammer. “Test-Analysis-Model Development Using an Exact Modal Reduction”. en. In: *International Journal of Analytical and Experimental Modal Analysis* 2.4 (1987), pp. 174–179.

[133] Riccardo Cirillo. “Detailed and Condensed Finite Element Models for Dynamic Analysis of a Business Jet Aircraft”. en. MA thesis. Politecnico di Milano, 2011.

[134] Darshan Sarojini. “An Efficient Method to Dimensionally Reduce Aperiodic Inhomogeneous 3-D Structures to 1-D Beam-Like Structures”. en. In: *AIAA SciTech 2020 Forum*. AIAA 2020-0272. Orlando, Florida, Jan. 2020. DOI: `10.2514/6.2020-0272`.

[135] Ferdinando Auricchio, Marco Alfano, and Gianni Artioli. “Efficient Nonlinear Reduced Order Model Updating for Aeroelastic Analysis of Aircraft Structures”. en. In: *AIAA Journal* 59.8 (2021), pp. 2947–2961. DOI: `10.2514/1.J057563`.

[136] S. A. Dunn. “Optimisation of the Structural Dynamic Finite Element Model for a Complete Aircraft”. en. PhD thesis. University of Bristol, 1998.

[137] P. M. Trivailo et al. “Inverse Problem of Aircraft Structural Parameter Identification: Application of Genetic Algorithms Compared with Artificial Neural Networks”. en. In: *Inverse Problems in Science and Engineering* 15.6 (2007), pp. 643–663. DOI: `10.1080/17415970600573338`.

[138] Paul Vazhayil Thomas. “Development and Design Optimization of High-Fidelity Reduced Order Models for Dynamic Aeroelasticity Loads Analyses of Complex Airframes”. en. MA thesis. University of Michigan, 2018.

[139] Oğuzhan Köse. “Development of Reduced Order Model for Dynamic Analysis of Aircraft via Global Optimization”. en. MA thesis. Middle East Technical University, 2023.

[140] Florian Gerber. *optimparallel: A Parallel Version of `scipy.optimize.minimize (method='L-BFGS-B')`*. en. 2020. DOI: `10.5281/zenodo.3888570`.

[141] Randall J. Allemang. “The Modal Assurance Criterion: Twenty Years of Use and Abuse”. en. In: *Sound and Vibration* 37.8 (2003), pp. 14–23.

[142] P. Vacher, B. Jacquier, and A. Bucharles. “Extensions of the MAC Criterion to Complex Modes”. en. In: *Proceedings of ISMA2010*. ONERA. Toulouse, France, 2010.

[143] Rishad Ahmed Shafik. “On the Extended Relationships Among EVM, BER and SNR as Performance Metrics”. en. In: *Proceedings of the 4th International Conference on Electrical and Computer Engineering (ICECE 2006)*. Dhaka, Bangladesh, Dec. 2006, pp. 497–500. DOI: `10.1109/ICECE.2006.355657`.

[144] Rene Schmogrow, Bernd Nebendahl, et al. “Error Vector Magnitude as a Performance Measure for Advanced Modulation Formats”. en. In: *IEEE Photonics Technology Letters* 24.1 (2012), pp. 61–63. DOI: `10.1109/LPT.2011.2179554`.